

Impact of Majorana fermions on the Kondo state in the carbon nanotube quantum dot

D. Krychowski¹

¹*Institute of Molecular Physics, Polish Academy of Sciences
M. Smoluchowskiego 17, 60-179 Poznań, Poland*

(Dated: August 13, 2024)

We have studied the quantum conductance of the Kondo state in the carbon nanotube quantum dot (CNTQD) with side-attached multi-Majorana fermion states in topological superconductors (TSCs). The zero-energy Majorana fermions interfere with the fourfold degenerate states of the CNTQD in the spin-orbital Kondo regime. Using the extended Kotliar-Ruckenstein slave-boson mean-field approach, we have analyzed the symmetry reduction of the SU(4) Kondo effect to the SU*(3) Kondo state with a fractional charge in the system by increasing the tunneling strength to a single Majorana fermion (TSC). We observed the fractional quantum conductance, the residual impurity entropy, the enhancement of the thermoelectric power with two compensation points, the fractional linear and nonlinear Fano factor (F_K) and the spin polarization of the conductance. Two Majoranas (2TSC) in conjunction with the CNTQD have reduced the spin-orbital Kondo effect to the SU*(2) Kondo state with $2e$ in the system. F_K contains information about the effective charge and the interaction between the quasiparticles, two- and three-body correlators and identifies the broken symmetry of the Kondo state. We discussed the local quadratic Casimir operator separately for the states associated with the Kondo effect and the Majorana fermion state to show the difference between the fluctuations of the pseudospin in both quantum channels. We have shown that the device coupled with three Majorana fermions (3TSC) achieves a quantized conductance $5/2(e^2/h)$, conserves the U*(1) charge symmetry at the electron-hole symmetry point and manifests the increase in nonlinear current and shot noise due to the entanglement in octuplets with opposite charge-leaking states. Furthermore, we have investigated the influence of the spin-orbit interaction in the CNTQD-TSC device on the quantum transport properties.

PACS numbers: 72.10.Fk, 73.63.Kv, 71.27.+a, 85.35.Kt, 74.45.+c, 05.30.Pr

I. INTRODUCTION

The quantum dot can be realized in the carbon nanotubes due to the quantization effect of the confinement potential [1, 2]. One of the interesting features in the low-dimensional systems is the Kondo effect [3–8], where the localized pseudospin or spin states on the quantum dot are screened by the conduction electrons in the leads. The system is in the new ground state, called the Kondo singlet, which opens the transport window in the Coulomb blockade region [4].

The screening effect plays one of the most important roles in the formation of the Kondo singlet [9]. One of the popular methods to solve the Kondo cloud problem is the numerical renormalization group (NRG) method [10], where the screening strongly depends on the number of sites in the Wilson chain and is based on deleting the states in the growing Hilbert space. In another method, the poor man’s scaling method, we solve the Kondo Hamiltonian (the effective Hamiltonian of the Anderson model reduced by the Schrieffer-Wolff canonical transformation using the projection operator technique). In the solution we observe an asymptotic strengthening of the Kondo exchange coupling, logarithmically proportional to the Kondo temperature. Other methods, which include the problem of spin-orbital fluctuations, the finite Coulomb interaction, the Fermi liquid behavior [11] and the scaling problem [12], are the symmetrized finite-U NCA (non-crossing approximation) [13], the equation of motion (EOM) method [14, 15], or

the extended Kotliar-Ruckenstein slave-boson mean-field approach (KR-sbMFA)[16] based on path integral methods [17]. On the other hand, the Bethe ansatz approach (BAA) is reserved to the strong coupling limit (infinite-U) and is also limited to the number of states in the chain [18], which is a mapping between a set of quantum numbers and a set of momenta. This map is nonlinear and fully coupled. In this paper [19, 20], the authors showed that the single impurity Anderson model is completely integrable with finite U using the Bethe ansatz approach and solved the transcendental equations with the energies lying not far from the Fermi level. Formally, for non-trivial values of the interaction, Bethe’s equations form a transcendental system of equations that can’t be solved in closed form. However, as is often the case in statistical mechanics, it is hoped that moving to a thermodynamically large system will simplify matters somewhat. In any case, all these methods have some limitations, but in most general aspects they describe the N-orbital Anderson model with modifications.

The Kondo singlet has been realized in the heterostructure [7, 21] and molecular devices [22–25], but was first discovered in the dilute alloys [9]. In contrast to heterostructure quantum dots [4, 6, 7], the intra- and inter-Coulomb interactions in carbon nanotube quantum dots (CNTQD) are comparable, which is an essential condition for the formation of the SU(4) Kondo effect [2, 5, 26–28]. In CNTQD, the Kondo temperature [3, 5, 26, 27] is three orders of magnitude higher than the millikelvin temperatures observed in GaAs quantum dots [4, 6]. These

two aspects are the features that determine the experimental attractiveness of CNTQDs in the strongly correlated electron regime [12, 17, 29]. The Seebeck coefficient for the Kondo-correlated single quantum dot transistor is suppressed at the electron hole symmetry point and changes sign beyond this point [30, 31]. This is a result of the linear response theory [32] and is a consequence of Fermi liquid (FL) behavior. For temperatures below the Kondo temperature T_K only the linear coefficient contributes to the Seebeck effect and the thermoelectric power (TEP) is proportional to the ratio of the derivative of the quasiparticle densities to itself (the Mott's formula) [33]. The Seebeck effect has also been observed in the Coulomb blockade regime [34]. The authors observed the large enhancement of the thermoelectric power (TEP) in a double quantum dot system due to interference and Coulomb correlation effect.

The model of CNTQD is described by the linear approach of graphene bands [8, 35]. The quantum numbers that characterize the carbon quantum dots are the spin, isospin (valley) and pseudospin (lattice) numbers. The source of the energy gap in semiconducting CNTQDs is the chirality of the nanotube (the gap is proportional to one over the diameter of the nanotube) and the perturbation effects (the perturbation gap is smaller than the geometry gap and proportional to one over the square of the diameter of the nanotube) [2, 8]. Despite the fact that the spin-orbit interaction (SOI) is negligible in graphene, the SOI has been uncovered in the semiconducting CNTQD [2, 5, 36]. In flat graphene, the symmetry forbids direct hopping between orbitals with opposite parity under the inversion. In a nanotube, the symmetry is broken by the curvature, and the SOI arises from the direct hybridization between the non-orthogonal orbitals on the A and the B sites in graphene [2, 37–39]. The spin-orbit coupling breaks the fourfold degeneracy in the shell of the CNTQD and leads to the ground state with two Kramers doublets [8] (opposite pairs in the spin and isospin sectors). Increasing the SOI changes the symmetry of the Kondo effect from SU(4) to SU(2) [35, 40–43]. The SOI in CNTQD has two contributions: Zeeman (diagonal part in the A(B) lattice basis) and orbital (off-diagonal part). The value and sign of these interactions determine the ground state in the energy spectrum of holes and electrons on the multishell quantum dot. In general, the SOI is of the order of tens of meV [2, 44], but for the ultraclean semiconducting CNTQD the coupling is comparable to the Coulomb interaction. Special attention has been paid to the problem of the square dependence in the magnetic field of the CNTQD states [44] as a consequence of the narrow band gap in semiconducting CNTQD, which contributed to the spinful SU(3) Kondo state [45]. The observation of the SU(3) Kondo effect can be identified by localizing the quantum conductance to the characteristic value $(9/4)(e^2/h)$ [46].

One of the most important differences between SU(2) and SU(4) Kondo states in CNTQD, besides the conductance measurements, is the nonlinear shot noise detec-

tion using the lock-in technique [28, 47–50]. The electronic transport is described by the free non-interacting quasiparticles around the equilibrium state (low bias). In the non-equilibrium regime, two-particle scattering processes dominate due to the residual interaction. Using the Fermi liquid theory [11, 51–57], the authors showed that the interaction parameter [58], called the Wilson ratio, takes the quantized values $W = 2$ for SU(2) and $W = 4/3$ for SU(4) Kondo states and changes the corresponding effective charges e^* [59]. For single Kondo QDs, the experimental measurements showed the three-body correlation function in the nonlinear conductance at finite magnetic field, validating the recent Fermi liquid theory in the nonequilibrium Kondo regime [60].

Majorana fermions are their own antiparticles originally proposed by Ettore Majorana [61]. They are called real fermion quasiparticles because of the real nature of the creation and annihilation operators [62]. These quasiparticles exhibit non-Abelian braiding properties [62–64] and the Majorana fermion states are associated with zero energy modes that occur in the Bogoliubov-de Gennes description of a paired condensate with non-Abelian exchange statistics [65]. The search for Majorana quasiparticle bound states in condensed matter systems is motivated in part by their potential use as topological qubits and possible applications in quantum computation. The Majorana qubits are predicted for quantum states in the fault-tolerant non-Abelian quantum processors [63, 66–68]. A pair of Majorana fermions can be combined into a complex Dirac fermionic state. The Majorana fermion in this composite complex fermion is half of a normal fermion, and is obtained as a superposition of two Majorana fermions. Each of the Majorana fermions is basically split into a real and an imaginary part of a fermion. The Majorana fermions exist at the edges of proximitized quantum wire by p-wave superconductor [69]. The states are spatially separated and protected from most types of decoherence. However, in [70] as a result, the authors showed that the Majorana qubit coherence and the fermion parity conservation cannot be immune to local perturbations during the braiding operations.

The statistical thermodynamic calculation based on the NRG method showed that the entropy of the quantum dot coupled to a single Majorana fermion leads to $S_{tot}/k_B = \ln[2]/2$ and corresponds to the NFL behavior, confirming the anyonic non-Abelian nature of the hybrid device [71]. The author presented the contribution of the impurity to the electron entropy as a function of the temperature for different values of the ratio of the Majorana tunneling rate.

Rasetti and Castagnoli argued that anyons could be used to perform quantum computations [72]. The idea of statistical mechanics in anyons was originated with Arovas et al. [73] and had previously been studied by Frank Wilczek [74]. The author mentioned that the interchange of two particles orbiting around the magnetic flux manifests itself as an arbitrary phase between bosons and fermions, and called the exotic state anyons. Other

authors showed that the excitation spectrum of a half-quantum vortex in a p-wave superconductor contains a zero-energy Majorana fermion with non-Abelian statistics [75–77]. Haldane proposed that the reduction of the apparent Hilbert space dimension by non-orthogonality of states describes localized topological defects at different points in space is also seen in the fractional quantum Hall effect (FQHE), and seems to be the fundamental feature of the fractional statistics [78]. In [76] the authors suggest, that p-wave superfluids, and the Moore-Read state are predicted to support the simplest non-Abelian anyons - the Ising anyons. Their behavior can be understood in terms of Majorana fermion modes at the vortex cores, and it is argued that in 1d, non-Abelian and in particular $SU(2)$ level- k statistics manifest themselves in fractional statistics. For $k = 2$, the authors have observed for the Ising anyons that the state counting of the internal Hilbert space associated with the non-Abelian statistics is equivalent to that of the Majorana fermion states coupled to the spinons [76].

The simplest model of the Majorana fermion is predicted by the Kitaev toy model which assumes the spinless topological superconductor (TSC) [69]. In real TSC, we should consider the polarization of the Majorana fermions in the Rashba and Dresselhaus 1d wire. The authors [79] introduced the Majorana pseudospin and showed that the local Majorana polarization is correlated with the transverse spin polarization. Other authors [80, 81] studied the selective equal spin Andreev reflections (SESARs) spectroscopy to detect the polarized Majorana quasiparticles appearing at the edges of the proximitized Rashba chain. In this paper the authors show under which conditions a pseudo-spin degree of freedom can be attributed to Majorana bound states (MBS). MBS correspond to class D and are related to the Z -topological invariant. Class DIII with mirror symmetry supports multiple MBS and is described by the Z_2 -invariant with an additional time-reversal symmetry [82].

Discussions remain divided regarding over the preparation and actual implementation of Majorana fermions in low-dimensional systems [83–85]. Regardless of the scientific dispute, the $SU(2)$ Kondo effect in quantum dots can be used as a very precise detector of topologically protected Majorana states [86, 87]. There are currently several candidates for host boundary Majorana quasiparticles: vortices in two-dimensional (2d) $p_x + ip_y$ spinless superconductors [88], Moore-Reed type states in FQHE [89, 90], the surface of a 3d topological insulator in proximity to an s-wave superconductor [91], 2d semiconductors with strong spin-orbit coupling coupled to an s-wave superconductor with broken time-reversal symmetry (using a local ferromagnet [92, 93] or an external magnetic field [94]), domain walls in 1d p-wave topological superconductors [95], and helical Majorana modes appearing at the two ends of a 1d wire [96, 97]. In particular, the authors of the references [98] demonstrated in InSb nanowires with strong Rashba-type spin-orbit coupling,

the artificial realization of a p-wave superconductor and the observation of a magnetic field-induced zero-bias conductance peak, as expected for a zero-energy Majorana fermion signature [99, 100]. In this setup, where the presence of a topological superconductor is controlled by the Zeeman gap, these systems require a delicate balance of the (spin-orbit coupling, magnetic field and chemical potential) to create the topological superconductor. The idea of 1d spinless p-wave superconductor based on the semiconducting nanowire, where spin-orbit coupling is used to shift the spin-up/down levels in the momentum space and Zeeman field, leading to spin splitting and spin texture at the Fermi level. A proximity induced SC gap within the spin-split levels would lead to an effective spinless p-wave SC [101].

Recently, a topological superconductor has been realized in 1d ferromagnetic atom chains [102], where the 1d system with a strong spin-orbit interaction is placed in proximity to a conventional s-type superconductor. Using high-resolution spectroscopic imaging techniques, the authors have demonstrated the spatially resolved signature of edge-bound Majorana fermions in Fe atom chains and the appearance of zero-energy states in the electronic density of states of the chains. Majorana fermion states are expected to be realized in class D topological superconductors (TSCs with broken time-reversal symmetry)[82]. However, Majorana zero modes can also appear in pairs in time-reversal invariant DIII class topological superconductors. These interesting types of Majorana fermions are called Majorana Kramers pairs [103, 104]. For example, chiral superconductors with $p_x + ip_y$ pairing state in 2d have a sharp topological distinction between the strong and weak pairing regime [87, 103, 104]. In the weak pairing regime, the gapless chiral Majorana states at the edge are topologically protected. In two dimensions, a time-reversal invariant topological defect of a Z_2 non-trivial superconductor carries a Kramers pairs of Majorana fermions [105].

One of the interesting papers focuses on the aspect of Majorana-Klein hybridization: in [106, 107] the authors demonstrate a topological Kondo effect that implements the $SO(M)$ Kondo problem for M Majorana lead couplings. These topological Kondo states give rise to robust non-Fermi liquid behavior, even for Fermi liquid leads, and to a quantum phase transition between the insulating and Kondo regimes when the leads form Luttinger liquids.

In another paper, the authors studied the interacting Majorana fermions [108]. This is quite a challenge. The simplest interactions between the Majorana degrees of freedom show an unusual non-local structure involving four distinct Majorana sites [109]. The authors [108] solved the Sachdev-Ye-Kitaev model and showed that correlated phases of matter with Majorana building blocks can lead to emergent spacetime supersymmetry (SUSY), topological order or Fibonacci topological phase, which are more exotic generalizations of Majorana fermions known as parafermions.

Returning to the issues discussed in this article, the previous theoretical work investigated the problem of the Majorana zero mode coupled to the spin Kondo state using NRG methods: in single [71, 110, 111] and double quantum dots [112, 113]. Several papers have discussed the thermoelectric effects of quantum dots coupled to side-attached TSCs in the Coulomb blockade regime [114–116] and in the T-shaped DQD system in the Kondo state side-attached to the Majorana fermion [117]. In these thermoelectric quantum devices, the thermopower changes sign and is fully spin polarized. Measurements of the Seebeck coefficient beyond the e-h symmetry point show strong enhancement and a violation of the Wiedeman-Franz law.

The Kondo cloud plays the role of an interference detector for Majorana fermions. In this article, we discuss the influence of weakly and strongly coupled multi-Majorana fermions on the spin-orbital SU(4) Kondo effect in the carbon nanotube quantum dot. We have coupled three TSC devices proximitized by AB superconducting pairing coat. SOI and SC leads to the Majoranization of the wire states of the zigzag CNT in the absence of a magnetic field. The Majorana states are indexed by the spin-orbital numbers and coupled to the fourfold degenerate states of the CNTQD. The Majorana-Kondo effect is observed for the strong coupling strength limit and manifests itself as the coexistence of the strongly correlated electrons and the topological Majorana states in the system. The spin-orbital type of the Majorana quasiparticles is chosen by the sign of the SOI. An alternative realization is proposed in the armchair CNT, where the electric field can induce the Majorana fermions [118].

The shot noise for the QD-TSC device in the weak coupling limit and for the SU(2) Kondo quantum dot is discussed in [119], where the the shot noise power for the linear voltage is quantized to $(1/2)(e^2/h)$. Alternatively results, using the Keldysh field integral description are presented in [120, 121], where the author suggests that in the Majorana state, for positive atomic level of the QD, we should observe two different fractional effective charges at low and high energies, $e^*/e=1/2$ and $e^*/e=3/2$, accessible at low and high bias voltages. In another paper [122] the authors analyzed the shot noise in a 1d Majorana chain fermion coupled to a normal metal, and found that the Fano factor is quantized to $F=2$ for the single Majorana bound state (MBS) and to non-integer F when both MBSs couple to the lead.

The paper is organized as follows. In Sec. II we discuss the Hamiltonian of the two-orbital Anderson model coupled with one, two and three topological superconducting wires (1TS, 2TS and 3TSC). In the subsections of Sec. III we demonstrate the detection of the symmetry reduction of the spin-orbital SU(4) Kondo effect to exotic SU*(3) and SU*(2) Kondo states in the quantum transport measurements (i.e. quantum conductance, thermoelectric power, linear and nonlinear shot noise). In the last part of the results we study the influence of the SOI

on the Majorana-Kondo states. Finally, we summarize the results in the conclusions.

II. MODEL OF A CNTQD COUPLED TO SIDE-ATTACHED TOPOLOGICAL SUPERCONDUCTORS

We address the calculation to the system with quantum dot tunneling coupled to multi-Majorana fermions (Fig. 1). We model the carbon nanotube quantum dot (CNTQD) by using the two-orbital Anderson Hamiltonian with side-attached topological superconductors (TSCs):

$$\begin{aligned} \mathcal{H} = & \sum_{ls} E_{ls} n_{ls} + \sum_l U n_{l\uparrow} n_{l\downarrow} + \sum_{ss'} U n_{+1s} n_{-1s'} + \\ & \sum_{k\alpha ls} E_{k\alpha ls} n_{k\alpha ls} + \sum_{k\alpha ls} t_0 (c_{k\alpha ls}^\dagger d_{ls} + h.c) + \\ & \sum_s i t_{+1s} \gamma_{+1s} (d_{+1s}^\dagger + d_{+1s}) + i t_{-1\uparrow} \gamma_{-1\uparrow} (d_{-1\uparrow}^\dagger + d_{-1\uparrow}), \end{aligned} \quad (1)$$

where the first term describes the energy of the spin-orbital quantum dot level ($E_{ls} = E_d(V_g) + ls\Delta/2$). Δ is the spin-orbit interaction (SOI) observed in the CNTQD [2, 8], which arises from the curvature of the carbon nanotube [39]. $s = \uparrow (\downarrow)$ and $l = \pm 1$ are the spin and orbital numbers. The second and third terms are the intra- and inter-Coulomb interactions in the system. The next two parts of the Hamiltonian (1) are related to the energy of the left and right electrodes $E_{k\alpha ls}$ ($\alpha = L, R$) and the tunneling strength between the CNTQD and the normal electrodes (t_0). The last two terms are the tunneling terms of the Majorana fermions γ_{ls} with the QD states. The tunneling strength is given by t_{ls} , and in the paper we considered three types of hybrid systems: CNTQD-TSC ($t_{+1\uparrow} = t$), CNTQD-2TSC ($t_{+1\uparrow} = t_{-1\uparrow} = t$) and CNTQD-3TSC device (where $t_{+1s} = t_{-1\uparrow} = t$). The Majorana fermions are indexed by their spin-orbital number. All energies are given in Γ units, where $\Gamma = \frac{\pi t_0^2}{2W}$ is the tunnel coupling. $1/2W$ is the flat density of states in the electrode, inversely proportional to the half bandwidth (W).

Using the extended slave-boson Kotliar-Ruckenstein mean-field approach [16, 40, 45], the Hamiltonian (1) can be written in the effective form:

$$\begin{aligned} \tilde{\mathcal{H}} = & \sum_{ls} \tilde{E}_{ls} n_{ls}^{(f)} + U \sum_{\nu} d_{\nu}^\dagger d_{\nu} + 3U \sum_{ls} t_{ls}^\dagger t_{ls} + \\ & 6U f^\dagger f + \lambda(\mathcal{I} - 1) - \lambda_{ls} \sum_{ls} Q_{ls} + \\ & \sum_{k\alpha ls} t_0 (c_{k\alpha ls}^\dagger z_{ls} f_{ls} + h.c) + i t_{-1\uparrow} \gamma_{-1\uparrow} (z_{-1\uparrow}^\dagger f_{-1\uparrow}^\dagger + h.c) \\ & \sum_s i t_{+1s} \gamma_{+1s} (z_{+1s}^\dagger f_{+1s}^\dagger + h.c) \end{aligned} \quad (2)$$

where $\tilde{E}_{ls} = E_{ls} + \lambda_{ls}$ is the renormalized energy level of the quasiparticle Kondo resonance. λ and λ_{ls} are

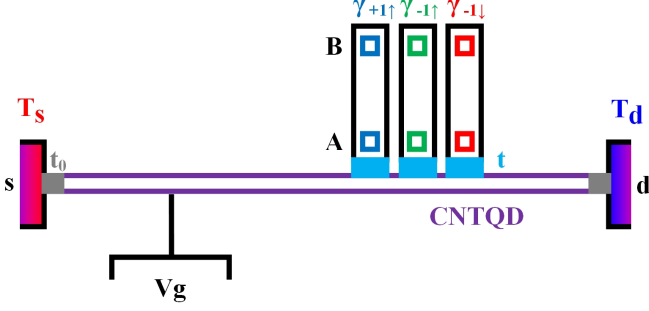


FIG. 1. (Color online) Carbon nanotube quantum dot (CNTQD) device tunnel-coupled through V to the normal leads and through t to the Majorana fermion quasiparticle states (γ_{ls}) in topological superconducting (TSC) wires. The back-gate V_g changes the number of the electrons on the CNTQD. $\delta T = T_s - T_d$ is the temperature gradient applied to the left and right electrodes $s(d)$ in the thermoelectric power measurements.

the Lagrange multipliers associated with the completeness relation ($\mathcal{I} = e^\dagger e + \sum_{ls} p_{ls}^\dagger p_{ls} + \sum_{\nu=20,02,s\bar{s}} d_\nu^\dagger d_\nu + \sum_{ls} \bar{t}_{ls}^\dagger \bar{t}_{ls} + f^\dagger f$) and charge conservation ($Q_{ls} = \tilde{z}_{ls}^\dagger \cdot \tilde{z}_{ls} = p_{ls}^\dagger p_{ls} + d_l^\dagger d_l + \sum_{s'} d_{ss'}^\dagger d_{ss'} + \bar{t}_{ls}^\dagger \bar{t}_{ls} + \sum_{s'} \bar{t}_{ls'}^\dagger \bar{t}_{ls'} + f^\dagger f$). The \cdot denotes the non-commutative multiplication in the charge operator. In the effective Hamiltonian, the quantum dot operators d_{ls} are replaced by the product of the bosonic operator z_{ls} and the pseudofermionic operator f_{ls} ($d_{ls} \equiv z_{ls} f_{ls}$). Thus, all physical states are obtained by creating electrons and auxiliary bosons on the vacuum state $|\text{vac}\rangle$. In this formalism, the empty and the fully occupied states are generated by the operators as follows: $|e\rangle = |00\rangle = e^\dagger |\text{vac}\rangle$ and $|f\rangle = |22\rangle = f^\dagger \prod_{ls} f_{ls}^\dagger |\text{vac}\rangle$. The single particle electron state is represented by $|p_{+s(-s)}\rangle = |s0(0s)\rangle = p_{ls}^\dagger f_{ls}^\dagger |\text{vac}\rangle$. The triple occupied states are given by $|\bar{t}_{\pm s}\rangle = |s2(2s)\rangle = \bar{t}_{\pm s}^\dagger f_{\pm s}^\dagger f_{\mp s}^\dagger f_{\mp s}^\dagger |\text{vac}\rangle$. The auxiliary canonical particles for the double occupied state are represented by six states: $|d_{20(02)}\rangle = |20(02)\rangle = d_{20(02)}^\dagger f_{\pm\uparrow}^\dagger f_{\pm\downarrow}^\dagger |\text{vac}\rangle$ and $|d_{ss(s\bar{s})}\rangle = |ss'\rangle = d_{ss(s\bar{s})}^\dagger f_{+s(+s)}^\dagger f_{-s(-\bar{s})}^\dagger |\text{vac}\rangle$.

The tunnel rates $\tilde{t}_{0ls} = t_0 z_{ls}$ and $\tilde{t}_{ls} = t_{ls} z_{ls}$ are renormalized by $z_{ls} = \tilde{z}_{ls} / \sqrt{\delta n_{ls}^2} = (e^\dagger p_{ls} + p_{l\bar{s}}^\dagger d_l + \sum_{l's'} p_{l's'}^\dagger d_{s's'} + \sum_l d_l^\dagger \bar{t}_{ls} + \sum_{l's'} d_{s's'}^\dagger \bar{t}_{l's'} + \bar{t}_{l\bar{s}}^\dagger f) / \sqrt{Q_{ls}(1-Q_{ls})}$. z_{ls} is the renormalization of the width of the Kondo resonance (compare with the amplitude of the quasiparticle wave function [17, 29]), and determines the Kondo temperature $T_K = \min\{T_{K,ls}\} = \sqrt{\tilde{E}_{ls}^2 + \tilde{\Gamma}_{ls}^2}$, where $\tilde{\Gamma}_{ls} = \Gamma |z_{ls}|^2$ is renormalized tunnel coupling. For the non-interacting system $U = 0$, $z_{ls}^2 \approx 1$ and we can say that the spin-orbital fluctuations are comparable to the tunneling processes involved in the in Kondo effect $\delta n_{ls} \approx \tilde{z}_{ls}^2$.

In the calculations, we consider three models: a quantum dot coupled to a single Majorana fermion

$\gamma_{+\uparrow}$ (CNTQD-TSC), with two Majorana fermions $\gamma_{\pm\uparrow}$ (CNTQD-2TSC), and with side-attached three Majoranas $\gamma_{\pm\uparrow}$ and $\gamma_{+\downarrow}$ (CNTQD-3TSC). In all systems we take the same value for the coupling strength t in the Hamiltonian (2). Using the saddle-point approximation, we solved the following self-consistent equations:

$$\begin{aligned} \frac{\partial \langle \tilde{\mathcal{H}} \rangle}{\partial b_n^\dagger} &= \frac{\partial \langle \tilde{\mathcal{H}} \rangle}{\partial b_n} = \Delta \tilde{\mathcal{H}}_n + \Delta \tilde{E}_n = 0 \\ \frac{\partial \langle \tilde{\mathcal{H}} \rangle}{\partial \lambda} &= \mathcal{I} - 1 = 0, \quad \frac{\partial \langle \tilde{\mathcal{H}} \rangle}{\partial \lambda_{ls}} = \langle f_{ls}^\dagger f_{ls} \rangle^< - Q_{ls} = 0 \end{aligned} \quad (3)$$

where b^\dagger is represented by auxiliary boson operators: $b_{n=1\dots 16}^\dagger = \{e^\dagger, p_{ls}^\dagger, d_\nu^\dagger, \bar{t}_{ls}^\dagger, f^\dagger\}$.

$$\begin{aligned} \Delta \tilde{\mathcal{H}}_n &= \sum_{k\alpha ls} t_0 \left(\frac{\partial z_{ls}}{\partial b_n^\dagger} \langle c_{k\alpha ls}^\dagger f_{ls} \rangle^< + c.c. \right) \\ &+ it_{-1\uparrow} \left(\frac{\partial z_{-1\uparrow}^\dagger}{\partial b_n^\dagger} \langle \gamma_{-1\uparrow} f_{-1\uparrow}^\dagger \rangle^< + c.c. \right) \\ &+ \sum_s it_{+1s} \left(\frac{\partial z_{+1s}^\dagger}{\partial b_n^\dagger} \langle \gamma_{+1s} f_{+1s}^\dagger \rangle^< + c.c. \right), \end{aligned} \quad (4)$$

and $\Delta \tilde{E}_n = \{\lambda e, (\lambda_{ls} + \lambda) p_{ls}, (U + \sum_s \lambda_{ls} + \lambda) d_l, (U + \lambda_{ls} + \lambda_{l\bar{s}} + \lambda) d_{s's'}, (3U + \lambda_{ls} + \sum_s \lambda_{l\bar{s}} + \lambda) \bar{t}_{ls}, (6U + \sum_{ls} \lambda_{ls} + \lambda) f\}$. The correlators in Eqs. (3-4) can be written in the form:

$$\begin{aligned} \langle f_{ls}^\dagger f_{ls} \rangle^< &= \int_{-W}^{+W} \frac{dE G_{ls,ls}^<}{2\pi i} \\ \sum_k \tilde{t}_{0ls} \langle c_{k\alpha ls}^\dagger f_{ls} \rangle^< &= \sum_k \tilde{t}_{0ls} \int_{-W}^{+W} \frac{dE G_{k\alpha ls,ls}^<}{2\pi i} \\ i\tilde{t}_{ls} \langle \gamma_{ls} f_{ls}^\dagger \rangle^< &= i\tilde{t}_{ls} \int_{-W}^{+W} \frac{dE G_{ls,ls}^<}{2\pi i} \end{aligned} \quad (5)$$

where $G_{ls,ls}^<$, $G_{k\alpha ls,ls}^< = \tilde{t}_{0ls} (G_{ls,ls}^R g_{k\alpha ls}^< + G_{ls,ls}^< g_{k\alpha ls}^A)$ and $G_{ls,ls}^<$ are the non-equilibrium Green's functions calculated using the EOM and Keldysh formalism for the Hamiltonian (2) [56, 123, 124]. The retarded and lesser Green's functions in the $\nu = ls$ channel (decoupled from the TSC) are given by $G_{\nu,\nu}^R(E) = (E - \tilde{E}_\nu + i\tilde{\Gamma}_\nu)^{-1}$ and $G_{\nu,\nu}^<(E) = G_{\nu,\nu}^R \tilde{\Sigma}_\nu^< G_{\nu,\nu}^A$. $\tilde{\Sigma}_\nu^< = \sum_\alpha \tilde{t}_{0\nu} g_{\alpha\nu}^< = i\tilde{\Gamma}_\nu \sum_\alpha f_\alpha$ is the lesser self-energy and $f_\alpha = (e^{\frac{E \pm V_\alpha}{k_B T}} + 1)^{-1}$ is the Fermi-Dirac function. The Green's functions in the ν' channel (the channel coupled to the TSC) can be written in the matrix form as follows:

$$\begin{aligned} \hat{G}_{\nu'}^R &= (E - \hat{E}_{\nu'} - \hat{\Sigma}_{\nu'}^R)^{-1} \\ &= \begin{pmatrix} E - \tilde{E}_{\nu'} + i\tilde{\Gamma}_{\nu'} & 0 & -i\tilde{t}_{\nu'} \\ 0 & E + \tilde{E}_{\nu'} + i\tilde{\Gamma}_{\nu'} & -i\tilde{t}_{\nu'} \\ i\tilde{t}_{\nu'} & i\tilde{t}_{\nu'} & E + i\delta \end{pmatrix}^{-1} \end{aligned} \quad (6)$$

where $\hat{E}_{\nu'}$ is the matrix of the diagonal energies $\{\pm \tilde{E}_{\nu'}, 0\}$, the remaining elements are the matrix of retarded self-energy $\hat{\Sigma}^R$. δ is the lifetime of the Majorana fermion, and is the lowest energy in the system

$\delta \ll T_K$ (in our calculations $\delta = 10^{-8}$). In practice this is the consequence of the disappearance of the overlap term between the Majorana fermions at the ends of the proximitized wire ($i\Delta_{(0)}\gamma_{Als}\gamma_{Bls}$) in the self-energy of the TSC $\tilde{\Sigma}_t^R = (\tilde{t}^2 z)/(z^2 - \Delta_{(0)}^2)$ [69, 119]. Therefore, in our model we used the self-energy with the finite lifetime of the Majorana fermion δ , where in the asymptotic limit: $\lim_{\Delta_{(0)} \rightarrow 0} \tilde{\Sigma}_t^R = \tilde{t}^2/z = \tilde{t}^2/(E + i\delta)$. The lesser Green's function matrix can be written as $\hat{G}_{\nu'}^< = \hat{G}_{\nu'}^R \hat{\Sigma}_{\nu'}^< \hat{G}_{\nu'}^A$, where $\hat{\Sigma}_{\nu'}^< = \hat{\Sigma}_{\nu'}^R \sum_{\alpha} f_{\alpha}$. The mean-field slave-boson approach has self-consistent solutions for finite temperature T and bias voltage $V_{\alpha=L(R)} = \pm V/2$ below and around the the Kondo temperature T_K .

III. THE RESULTS

A. The Hilbert space and the states of the isolated CNTQD-TSC devices

The tunneling term with the Majorana fermion (MF) can be written in the form : $it_{ls}\gamma_{ls}(d_{ls}^{\dagger} + d_{ls}) = it_{ls}(d_{ls}^{\dagger}\tilde{c}_{ls}^{\dagger} - d_{ls}\tilde{c}_{ls} - d_{ls}^{\dagger}\tilde{c}_{ls} - \tilde{c}_{ls}^{\dagger}d_{ls})$, where $\gamma_{ls} = \gamma_{Als} = \tilde{c}_{ls} + \tilde{c}_{ls}^{\dagger}$ is the Majorana operator and \tilde{c}_{ls} is the complex Dirac fermion operator in one-dimensional topological superconductor (1d TSC)[69]. As we can see, the term consists of the superconducting part $d_{ls}^{\dagger}\tilde{c}_{ls}^{\dagger}$, proportional to the isospin and the normal tunneling part $\tilde{c}_{ls}^{\dagger}d_{ls}$. The Majorana fermion states are spatially separated at the ends A and B in the 1d TSC (Fig. 1). Taking two spatially separated MFs and the electron creation operator $\tilde{c}_{ls}^{\dagger} = \tilde{c}_{Als}^{\dagger} = (1/2)(\gamma_{Als} - i\gamma_{Bls})$, we can define the occupation number operator in the topological superconductor as: $\tilde{n}_{ls} = \tilde{c}_{ls}^{\dagger}\tilde{c}_{ls} = (1 + i\gamma_{Als}\gamma_{Bls})/2$, what is the consequence of the number of the states $\{0, \uparrow\}$. Therefore the occupation number \tilde{n}_{ls} is either 0 or 1. In the limit of the vanishing overlap between the Majorana fermions, there is still a nonlocal half-fermionic state in the single or zero quantum state, which is the main argument and attraction in the the topological quantum computation.

The Majorana fermions obey the Clifford algebra $\{\gamma_{\nu}, \gamma_{\nu'}^{\dagger}\} = \delta_{\nu,\nu'}$ ($[\gamma_{\nu}, \gamma_{\nu'}^{\dagger}] = 0$), where $\delta_{\nu,\nu'}$ is the Kronecker delta and ν, ν' are Majorana indices. Moreover, unlike the complex fermions, Majoranas do not square to zero, but $\gamma_{\nu}^2 = 1/2$ ($\gamma_{\nu}^3 = \gamma_{\nu}/2$). The quasiparticle parity $\tilde{c}_{ls}^{\dagger}\tilde{c}_{ls}$ is accessible by a joint measurement on both Majoranas. So we are talking about new half-fermions on the both sides of the topological wire, and γ_{ls} are the real operators and are own antiparticles. We neglect in our calculation the effect of overlapping between Majorana fermions in the form $i\Delta_{(0)}\gamma_{Als}\gamma_{Bls}$, which leads to a bowtie-like mismatch in the zero energy non-local Majorana state [40, 125]. $\Delta_{(0)} = e^{-w/\lambda_K}$, where w is the separation length between Majoranas in the TSC, and λ_K determines the quality of the MFs and is the superconducting coherence length, which strongly suppresses

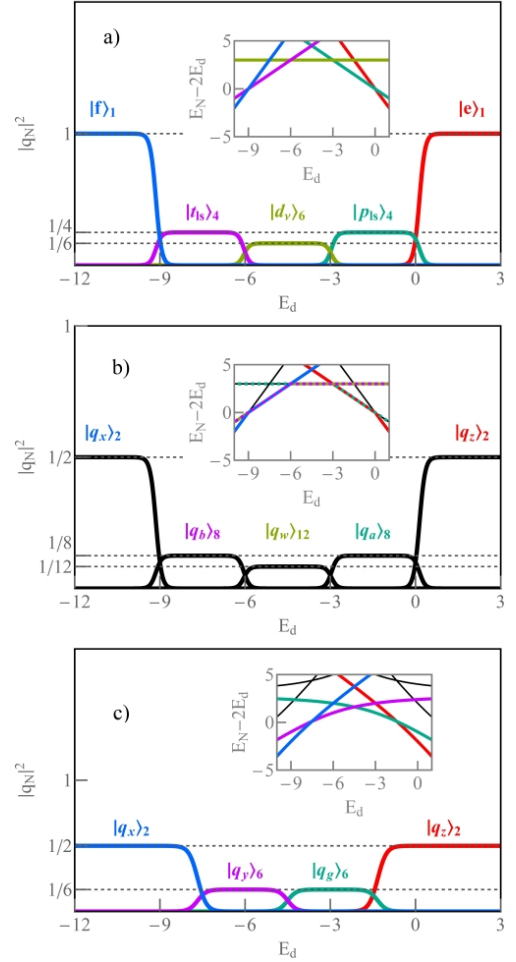


FIG. 2. (Color online) Isolated states of the CNTQD-TSC hybrid device: a-c) The quantum amplitudes $|q_N|^2$ of the ground states as a function of the quantum dot level E_d for decoupled ($t = 0$), weakly ($t = 10^{-2}$) and strongly ($t = 2$) coupled CNTQD with TSC. The insets show the spectrum of the energies $E_N - 2E_d$ with low energy ground states indicated by colors. $|q_N>_d$ represents the topological entangled quantum states except the pure quantum states in Fig. a ($T = 10^{-1}$).

the overlap between two Majoranas. For the Hamiltonian $\mathcal{H}_{ls} = (ls\Delta - E_g)\hat{\sigma}_Z \otimes \hat{\sigma}_X + \Delta_{(l)} \sum_{k=\pm} \mp \hat{\sigma}_k \otimes \hat{\sigma}_Y$ in the Nambu basis $\Psi = (c_{Als}, c_{Bls}, c_{Als}^{\dagger}, c_{Bls}^{\dagger})$, where Δ is the spin-orbit coupling strength [8], $E_g = N\Delta_l$ is the perturbation gap and Δ_l is the triplet AB-site superconducting order parameter (different for orbital $l = \pm$), we can find four independent Majorana bound state solutions at the zero energy level: $\gamma_{Als} = \Psi \cdot (1/\sqrt{2})\{1, 0, 1, 0\}^T$ and $\gamma_{Bls} = \Psi \cdot (i/\sqrt{2})\{0, 1, 0, -1\}^T$ for $\Delta = \Delta_l/(N - ls)$. In this simple toy model, we consider the TSC wire with the Zeeman-like SOI term [8] and the orbital dependent AB triplet superconducting pairing strength. The proximitized term in the Hamiltonian \mathcal{H}_{ls} is the crucial point of the toy model and will be a major challenge for experimental research [65].

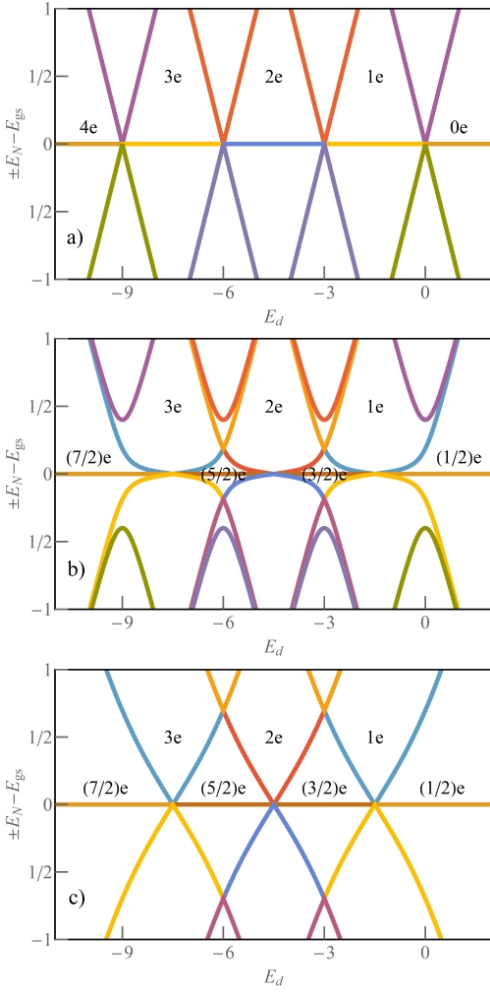


FIG. 3. (Color online) a-c) The difference between the excited states $\pm E_N$ and the ground state E_{gs} for decoupled, weakly and strongly coupled CNTQD with a single Majorana fermion state $\gamma_{+\uparrow}$. The numbers represent the integer and fractional charge on the quantum dot near the zero energy.

Our proposed device, shown in Figure 1 is the hybrid carbon nanotube quantum dot (CNTQD) with side-attached topological superconductor (TSC) fabricated on the 1d nanotube in the spin-triplet p-wave superconducting coat. The real fermion particles $\gamma_{ls} = \gamma_{l_s}^\dagger$ are located at the edges of the TSC. γ_{ls} consist of equal parts of electrons and holes with the same spin orbital. In contrast to the Bogoliubov quasiparticle operator $a_{ks}^\dagger = \Psi_k^\dagger \cdot \{u_k, v_k\}^T = u_k c_{ks}^\dagger + \text{sgn}(s)v_k c_{-k\bar{s}}$, where $a_{ks}^\dagger \neq a_{ks}$.

In our case, the Majorana fermions are well-prepared quantum states and are indexed by spin and orbital number, which determines the selective tunneling coupling term to ls states on CNTQD. The main discussion in the experiments is about the preparation of the states [83–85]. We should always look on the both sides of the wire and selectively detect the non-local Majoranas, e.g. using the doubling effect in the supercurrent [126, 127]. For this

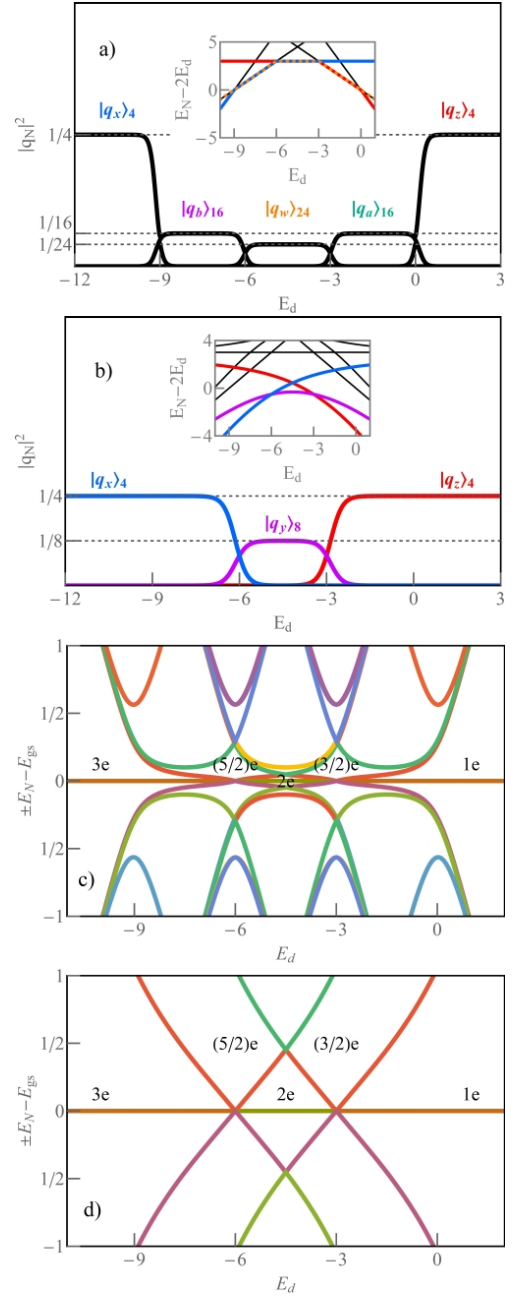


FIG. 4. Isolated states of the CNTQD-2TSC hybrid device: a, b) $|q_N|^2$ as a function of E_d for weakly ($t = 10^{-2}$) and strongly ($t = 2$) coupled CNTQD with two Majorana fermion states ($\gamma_{\pm\uparrow}$). c, d) E_d dependence of $\pm E_N - E_{gs}$ for the weak and strong tunnel coupling regime with TSCs.

reason, we focus on the problem of the side-attached TSC to the CNTQD in the Kondo state, which plays the role of a detector of non-Abelian MFs, especially observed in the quantum conductance, thermoelectric power and in the fractional noise measurements.

Let's first discuss the effect of the MF states on the quantum states in the isolated CNTQD ($t_0 = 0$). For finite Coulomb interaction $U = 3$, the two-orbital An-

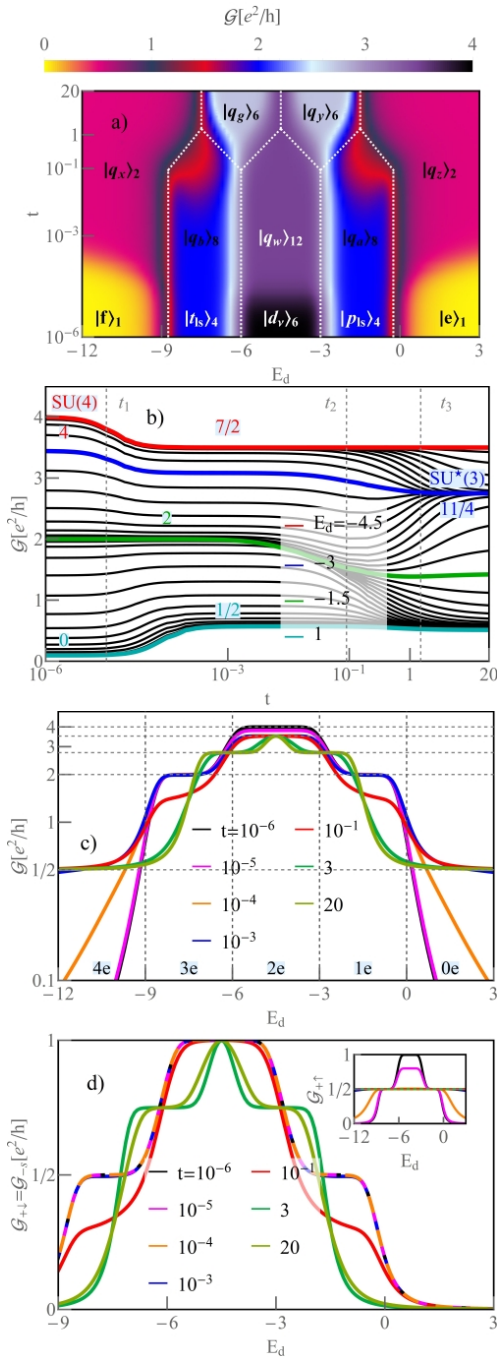


FIG. 5. (Color online) Quantum conductance for the fractional $SU^*(3)$ Kondo state: a) The density plot of \mathcal{G} as a function of E_d and t . $|q_N\rangle_d$ represents the ground state configuration in the CNTQD-TSC device. b) The landscape plot of \mathcal{G} as a function of t . The black lines are plotted with an increment of $\delta E_d = 0.15$ from $E_d = -4.5$ to $E_d = 1$. c, d) E_d dependence of the total and spin-orbital conductances with increasing t . The inset in Fig. d shows $\mathcal{G}_{\uparrow\downarrow}$ ($U = 3$, $\Gamma = 0.03$, $T = 10^{-8}$).

derson model can be written in the representation of occupation number on both orbitals $|n_+n_-\rangle$. The system describe the sixteenth quantum states: $|e\rangle = |00\rangle, |p_{ls}\rangle =$

$|s0\rangle = |0s\rangle, |d_\nu\rangle = |\nu\rangle = |20\rangle = |02\rangle = |ss\rangle = |s\bar{s}\rangle, |t_{ls}\rangle = |s2\rangle = |2s\rangle, |f\rangle = |22\rangle$. Figure 2a shows the probability of the quantum amplitudes $|q_N|^2$ for decoupled CNTQD with TSC ($t = 0$). $|q_N|^2 = e^{-E_N/(k_B T)}/Z_N$ are calculated for $U = 3$ and $T = 0.1$. $Z_N = \sum_N e^{-E_N/(k_B T)}$ is the partition function and E_N are the energies of the

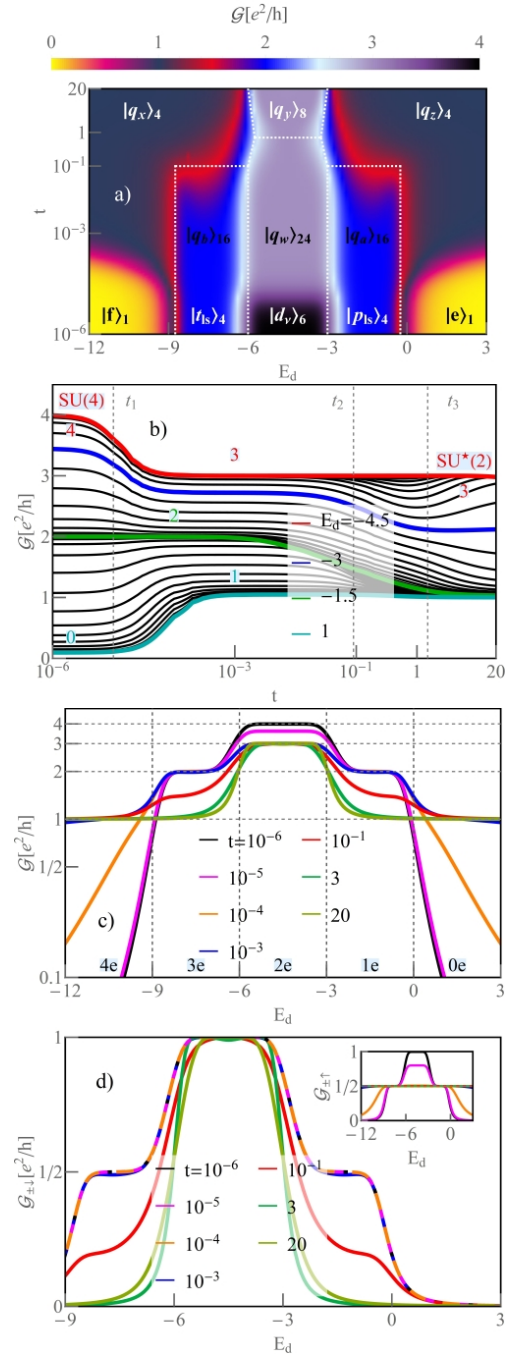


FIG. 6. (Color online) Quantum conductance for the integer $SU^*(2)$ Kondo state in the CNTQD-2TSC system: a) The density plot of \mathcal{G} as a function of E_d and t . b) The landscape plot of \mathcal{G} as a function of t ($\delta E_d = 0.15$). c, d) E_d dependence of \mathcal{G} and \mathcal{G}_{ls} .

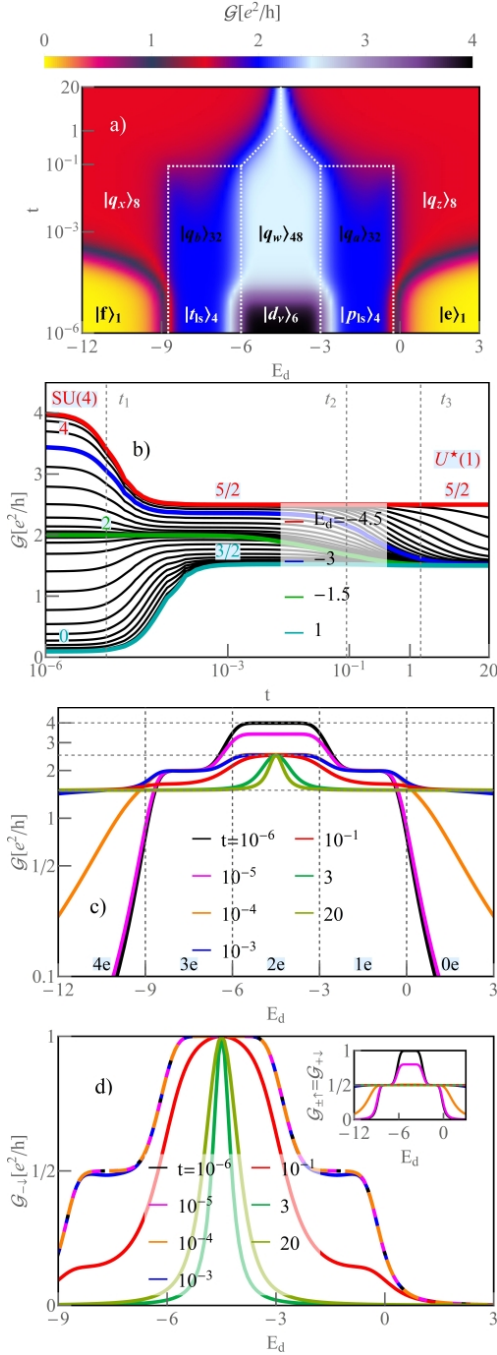


FIG. 7. (Color online) Quantum conductance in the CNTQD-3TSC device: a, b) The density plot and the landscape plot of G as a function of E_d and t ($\delta E_d = 0.15$). c, d) G and $G_{\pm 1}$ as a function of E_d with increasing t .

individual quantum states. Above $E_d = 0$ and below $E_d = -3U$, the empty $|e\rangle_1$ and the fully occupied states $|f\rangle_1$ without (0e) and with four electrons on CNTQD (4e) dominate. In the three-electron (3e) and one-electron (1e) charge region, the ground states $|t_{ls}\rangle_4$ and $|p_{ts}\rangle_4$ are the quadruplets with $|q_N|^2 = 1/4$. For two electrons (2e), the two-orbital Anderson model determines the six

quantum states $|d_\nu\rangle_6$ with $|q_N|^2 = 1/6$. The lower index \underline{d} in $|q_N\rangle_{\underline{d}}$ is the number of degenerate states. The inset shows the energies $E_N - 2E_d$. The lowest energies represent the ground state energy E_{gs} of the system and are represented by colored lines in the insets.

Taking the isolated CNTQD from the normal leads with tunneling term to the Majorana fermion state, we plotted $|q_N|^2$ and the energies E_N with the ground states for weak ($t = 10^{-3}$) and strong coupling limit to TSC ($t = 2$) (Fig. 2). The quantum states are spanned by the basis vectors, which consist from the normal part (quantum dot) $|n_+n_-\rangle$ and the topological segment $|n_1n_2n_3\rangle$. In the normal part, the states are defined by $n_{\pm} = \{0, \uparrow, \downarrow, 2\}$. The topological segment with two topological edge states is defined by a wave function describing one-qubit states for $|\underline{0}\rangle$ and $|\underline{\uparrow}\rangle$, and for the last two topological states $n_{2(3)}$, the allowed configurations are $|\underline{0}\rangle$, $|\underline{\uparrow}\rangle$ and $|\underline{0}\rangle$, $|\underline{\downarrow}\rangle$. The states are orthogonal and degenerate at zero energy, forming a two-dimensional Hilbert space for a single qubit state. Maximally, in the topological segment, the Hilbert space is the direct product of three Hilbert spaces and the many-body ground states are given by: $|n_1n_2n_3\rangle = |n_1\rangle \otimes |n_2\rangle \otimes |n_3\rangle$. The ground state degeneracy of 1d topological superconductors is $2^{N_{TS}}$. On CNTQD we have $2^n = 2^4 = 16$ quantum states ($|n_+n_-\rangle$). If we couple TSC to our setup, the number of states grows to the number $2^{n+N_{TS}}$. The quantum amplitudes in Fig. 2b reach the half value for $|q_z\rangle_{\underline{d}}$ and $|q_x\rangle_{\underline{d}}$. In the extended Hilbert space ($2^5 = 32$, $|n_+n_-\rangle$) for $E_d > 0$ and $E_d < -3U$ dominates $|q_z\rangle_2 = |q_{-z_1(\bar{1})}\rangle = \frac{1}{\sqrt{2}}(-|000(\underline{\uparrow})\rangle + |\uparrow 0(\underline{0})\rangle)$ and $|q_x\rangle_2 = |q_{-x_1(\bar{1})}\rangle = \frac{1}{\sqrt{2}}(-|\downarrow 20(\underline{\uparrow})\rangle + |22(\underline{0})\rangle)$. The minus sign in the lower index refers to the lower energy, the plus sign is reserved for the excited quantum states. In the following discussion, we have omitted the minus sign in the lower index, because we are focusing on the ground state. This is interesting because TSC entangles the pure quantum states from the even $|00(22)\rangle$ and the odd $|\uparrow 0(\downarrow 2)\rangle$ charge number sectors and opens the possibility of manipulating the states at the boundary of the integer charge numbers ($Q = 0e, 1e, 2e, 4e$). The topological qubit forms two doublets for fractional charge numbers $Q = (1/2)e$ and $Q = (7/2)e$. This scenario is observed for weak and strong coupling strengths t (Fig. 2a, b). Fig.2b shows the highly degenerate states for the weak coupling limit: two octuplets $|q_a\rangle_8(|q_b\rangle_8)$ and one duodecuplet $|q_w\rangle_{12}$. The low energy octuplets $|q_a\rangle_8$ in the 1e charge sector are given by:

$$\begin{aligned}
 |q_{-a_1(\bar{1})}\rangle &= -a'|000(\underline{\uparrow})\rangle + a|\uparrow 0(\underline{0})\rangle \\
 |q_{-a_2(\bar{2})}\rangle &= -a|0\uparrow 0(\underline{\uparrow})\rangle + a'|\uparrow\uparrow \underline{\uparrow}(\underline{0})\rangle \\
 |q_{-a_3(\bar{3})}\rangle &= -a|\downarrow 00(\underline{\uparrow})\rangle + a'|20(\underline{\uparrow}(\underline{0}))\rangle \\
 |q_{-a_4(\bar{4})}\rangle &= -a|0\downarrow 0(\underline{\uparrow})\rangle + a'|\uparrow\downarrow \underline{\uparrow}(\underline{0})\rangle
 \end{aligned} \tag{7}$$

and the high energy octuplets $|q_b\rangle_8$ can be written as

follows:

$$\begin{aligned}
|q_{-b_1(\overline{1})}\rangle &= -a|\downarrow 2\mathcal{Q}(\uparrow)\rangle + a'|2\mathcal{2}\uparrow(\mathcal{Q})\rangle \\
|q_{-b_2(\overline{2})}\rangle &= -a'|\downarrow\uparrow\mathcal{Q}(\uparrow)\rangle + a|2\uparrow\uparrow(\mathcal{Q})\rangle \\
|q_{-b_3(\overline{3})}\rangle &= -a'|0\mathcal{2}\mathcal{Q}(\uparrow)\rangle + a|\uparrow\uparrow 2\uparrow(\mathcal{Q})\rangle \\
|q_{-b_4(\overline{4})}\rangle &= -a'|\downarrow\downarrow\mathcal{Q}(\uparrow)\rangle + a|2\downarrow\uparrow(\mathcal{Q})\rangle
\end{aligned} \tag{8}$$

In the 2e charge region, the ground state of the system represents the duodecuplet $|q_w\rangle_{12}$ in the form:

$$\begin{aligned}
|q_{-w_1(\overline{1})}\rangle &= -a'|0\uparrow\mathcal{Q}(\uparrow)\rangle + a|\uparrow\uparrow\uparrow(\mathcal{Q})\rangle \\
|q_{-w_2(\overline{2})}\rangle &= -a'|\downarrow\mathcal{Q}\mathcal{Q}(\uparrow)\rangle + a|2\mathcal{Q}\uparrow(\mathcal{Q})\rangle \\
|q_{-w_3(\overline{3})}\rangle &= -a'|0\downarrow\mathcal{Q}(\uparrow)\rangle + a|\uparrow\downarrow\uparrow(\mathcal{Q})\rangle \\
|q_{-w_4(\overline{4})}\rangle &= a'|2\uparrow\mathcal{Q}(\uparrow)\rangle - a|\downarrow\downarrow\uparrow(\mathcal{Q})\rangle \\
|q_{-w_5(\overline{5})}\rangle &= a'|\uparrow\uparrow 2\mathcal{Q}(\uparrow)\rangle - a|0\mathcal{2}\uparrow(\mathcal{Q})\rangle \\
|q_{-w_6(\overline{6})}\rangle &= a'|2\downarrow\mathcal{Q}(\uparrow)\rangle - a|\downarrow\downarrow\downarrow(\mathcal{Q})\rangle
\end{aligned} \tag{9}$$

$a(a')$ are the amplitudes as the function of E_d , U and the coupling strength t . Despite the fact that $a' \ll a$ in the weak coupling limit to TSC, the states are entangled and the Hilbert space is extended (this is particularly important and visible in the $Q = 2e$ charge region). Fig. 2b shows $|q_N|^2 = 1/8$ for the two octuplets and $1/12$ for the single duodecuplet.

In the strong coupling limit $a \approx a'$ for $Q = (3/2)e$ and $Q = (5/2)e$, two sextuplets are the ground states of the system. The low energy quantum states $|q_g\rangle_6$ can be expressed as:

$$\begin{aligned}
|q_{-g_1(\overline{1})}\rangle &= -a|\downarrow\uparrow\mathcal{Q}(\uparrow)\rangle + a'|2\uparrow\uparrow(\mathcal{Q})\rangle \\
|q_{-g_2(\overline{2})}\rangle &= -a'|0\mathcal{2}\mathcal{Q}(\uparrow)\rangle + a|\uparrow\uparrow 2\uparrow(\mathcal{Q})\rangle \\
|q_{-g_3(\overline{3})}\rangle &= -a'|\downarrow\downarrow\mathcal{Q}(\uparrow)\rangle + a|2\downarrow\uparrow(\mathcal{Q})\rangle
\end{aligned} \tag{10}$$

and the high energy ground states $|q_y\rangle_6$ are described by: $|q_{-y_1(\overline{1})}\rangle = -a|0\uparrow\mathcal{Q}(\uparrow)\rangle + a'|\uparrow\uparrow\uparrow(\mathcal{Q})\rangle$, $|q_{-y_2(\overline{2})}\rangle = -a|\downarrow\mathcal{Q}\mathcal{Q}(\uparrow)\rangle + a'|2\mathcal{Q}\uparrow(\mathcal{Q})\rangle$ and $|q_{-y_3(\overline{3})}\rangle = -a|0\downarrow\mathcal{Q}(\uparrow)\rangle + a'|\uparrow\downarrow\uparrow(\mathcal{Q})\rangle$. The insets in Fig. 2 show the energies E_N . The lower colored lines are the ground state energies. As the tunneling strength increases, the lines on the insets, especially for intermediate couplings t , are the nonlinear function of E_d .

Figure 3 shows the difference between the energies E_N and the ground state energy for low bias $\pm E_N + E_{gs}$. At the zero energy line the system is determined by the ground state E_{gs} and all lines above and below this point show the excited states $\pm E_N + E_{gs}$. The excited states can be observed in the range of finite bias voltages $|V_{s(d)}| > 0$, higher than the Kondo temperature of the strongly correlated system. For decoupled CNTQD with TSC we observed the integer charge regions $Q = 1e, 2e, 3e$, where for $\pm E_N - E_{gs} = 0$ the $SU(4)$ Kondo state is realized. In the range of weak coupling strength regime the fractional charge regions $Q = (1/2)e, (3/2)e, (5/2)e$ and $(7/2)e$ are formed. For $Q = (1/2)e$

and $(7/2)e$ the ground state of the system is determined by two doublets $|q_z\rangle_2$ and $|q_x\rangle_2$, opening the Majorana channel in transport measurements. For the strong coupling t , the Majorana channel is independent and separate from the channels involved in the fractional $SU^*(3)$ Kondo effect. The Kondo state is denoted by \star because, in the contrast to the standard $SU(3)$ Kondo effect [45, 46], the quasiparticle state is formed for the fractional charges $Q = (3/2)e$ and $Q = (5/2)e$, which is non-trivial and the main result of the paper. The $SU^*(3)$ Kondo state is a signature of sixfold degenerate states: low $|q_g\rangle_6$ and $|q_y\rangle_6$ high energy sextuplets.

For the CNTQD-2TSC device, two spin-orbital channels $+\uparrow$ and $-\uparrow$ are correspondingly coupled to two selected Majorana quasiparticles $\gamma_{+\uparrow}$ and $\gamma_{-\uparrow}$. The Hilbert space for the isolated system CNTQD-2TSC is spanned by $2^{4+2} = 64$ quantum states. In the weak coupling regime (Fig. 4a), the probability amplitudes $|q_{a(b)}|^2$ lead to $1/16$ for $1e$ and $3e$ on the quantum dot. In the 2e charge region, the amplitudes reach the value $|q_N|^2 = 1/24$ and the lowest energy state is represented by the twenty-fourfold degenerate state $|q_w\rangle_{24}$. The sum of all degeneracies in the weak coupling limit leads to the number $\underline{d} = 4 + 16 + 24 + 16 + 4 = 64$, which is the number of all quantum states in the system. A similar relation can be written for CNTQD-TSC, where $\underline{d} = 2 + 8 + 12 + 8 + 2 = 32$. With increasing t (Fig. 4c, d) the four charge regions are reduced, and we observe the three quantum integer charge numbers $Q = 1e, 2e$ and $3e$. Empty $|e\rangle_1$ and full $|f\rangle_1$ occupied quantum states are switched to two quartets $|q_x\rangle_4$ and $|q_z\rangle_4$, which are visible in the transport measurements with the channels coupled to Majorana fermions. In the strong coupling regime the quantum states $|q_z\rangle_4$ are represented by:

$$\begin{aligned}
|q_{-z_1(\overline{1})}\rangle &= \frac{1}{2}(\mp|00\mathcal{Q}\mathcal{Q}(\uparrow\overline{\uparrow})\rangle \pm |0\uparrow\mathcal{Q}\overline{\uparrow}(\uparrow\overline{0})\rangle \\
&+ |\uparrow\uparrow 0\overline{\uparrow}(\mathcal{Q}\overline{0})\rangle + |\uparrow\uparrow\uparrow\overline{\uparrow}(\mathcal{Q}\overline{0})\rangle) \\
|q_{-z_2(\overline{2})}\rangle &= \frac{1}{2}(\pm|00\mathcal{Q}\overline{\uparrow}(\uparrow\overline{0})\rangle \pm |0\uparrow\mathcal{Q}\overline{0}(\uparrow\overline{\uparrow})\rangle \\
&- |\uparrow\uparrow 0\overline{\uparrow}(\mathcal{Q}\overline{0})\rangle + |\uparrow\uparrow\uparrow\overline{\uparrow}(\mathcal{Q}\overline{0})\rangle)
\end{aligned} \tag{11}$$

and the high energy quartets $|q_x\rangle_4$ have the following forms: $|q_{-x_1(\overline{1})}\rangle = \frac{1}{2}(|2\mathcal{2}\uparrow\overline{\uparrow}(\mathcal{Q}\overline{0})\rangle + |2\downarrow\uparrow\overline{0}(\mathcal{Q}\overline{\uparrow})\rangle \mp |\downarrow 2\mathcal{Q}\overline{\uparrow}(\uparrow\overline{0})\rangle \pm |\downarrow\downarrow\mathcal{Q}\overline{0}(\uparrow\overline{\uparrow})\rangle)$ and $|q_{-x_2(\overline{2})}\rangle = \frac{1}{2}(|2\mathcal{2}\overline{0}(\mathcal{Q}\overline{\uparrow})\rangle - |2\downarrow\uparrow\overline{\uparrow}(\mathcal{Q}\overline{0})\rangle \mp |\downarrow 2\mathcal{Q}\overline{0}(\uparrow\overline{\uparrow})\rangle \mp |\downarrow\downarrow\mathcal{Q}\overline{0}(\uparrow\overline{0})\rangle)$. The probability amplitudes for these states have the following value $|q_N|^2 = 1/4$ (Fig. 4b). As we can see in the inset of Fig. 4b, the energy ground states $E_N - 2E_d$ are the quadratic function of the atomic level E_d . For $Q = 2e$ the ground state is the octuplet $|q_y\rangle_8$ with eightfold degenerate states. All states contributing to the $SU^*(2)$ Kondo effect. The strongly correlated state is realized for even number of electron in the system, which is typical e.g for the charge Kondo state with polarons. The

octuplet quantum states can be written in the form:

$$\begin{aligned}
|q_{-y_1(\overline{1})}\rangle &= a|20\uparrow\overline{0}(\underline{0}\overline{\uparrow})\rangle + a'|2\uparrow\uparrow\overline{\uparrow}(\underline{0}\overline{0})\rangle \\
&\mp a'|\downarrow 0\overline{0}(\underline{\uparrow}\overline{\uparrow})\rangle \pm a|\downarrow\uparrow\overline{\uparrow}(\underline{\uparrow}\overline{0})\rangle \\
|q_{-y_2(\overline{2})}\rangle &= -a|20\uparrow\overline{\uparrow}(\underline{0}\overline{0})\rangle + a'|2\uparrow\uparrow\overline{0}(\underline{0}\overline{\uparrow})\rangle \\
&\pm a'|\downarrow 0\overline{\uparrow}(\underline{\uparrow}\overline{0})\rangle \pm a|\downarrow\uparrow\overline{0}(\underline{\uparrow}\overline{\uparrow})\rangle \quad (12) \\
|q_{-y_3(\overline{3})}\rangle &= \mp a|02\overline{0}\uparrow(\underline{\uparrow}\overline{0})\rangle \pm a'|0\downarrow\overline{0}(\underline{\uparrow}\overline{\uparrow})\rangle \\
&+ a'|\uparrow 2\uparrow\overline{\uparrow}(\underline{0}\overline{0})\rangle + a|\uparrow\downarrow\overline{\uparrow}(\underline{0}\overline{\uparrow})\rangle \\
|q_{-y_4(\overline{4})}\rangle &= \mp a|02\overline{0}\overline{0}(\underline{\uparrow}\overline{\uparrow})\rangle \mp a'|0\downarrow\overline{0}\uparrow(\underline{\uparrow}\overline{0})\rangle \\
&+ a'|\uparrow 2\uparrow\overline{0}(\underline{0}\overline{\uparrow})\rangle - a|\uparrow\downarrow\overline{\uparrow}(\underline{0}\overline{0})\rangle
\end{aligned}$$

The states are the combination of one single, one triple and two double quantum states spanned by Majorana fermion quantum states in TSCs. For the coupling strength $\tilde{t}_\nu \gg \tilde{\Gamma}_\nu$, the amplitudes in Eq. (12) are comparable $a' \approx a$ ($|q_N|^2 = 1/8$). All these eight states are the linear combination of the four extended states $|n_+n_-(n_1n_2)\rangle$. Figures 4c, d show that except for the zero energy state, which is represented by the integer charge $Q = 1e, 2e, 3e$, the excited states are determined by fractional charges $Q = (3/2)e$ and $(5/2)e$. All excited states can be observed in tunneling spectroscopy measurements. The fractional charges are manifested in the spin dependent conductances of a quantum dot side-attached to the topological superconductor [128]. For example, in [63] the authors have shown that non-Abelian rotations within the degenerate ground state manifold of a set of Majorana fermions and the quantum dot in the Coulomb blockade regime can be realized by adding or removing a single electron, and by exchanging electrons we can generate rotations similar to braiding operations. In the paper [63] the authors proposed the scheme to manipulate the state of a set of two Majorana fermions by changing the even/odd parity and degeneracy of the dot qubit states with the quantum flux $\varphi_1 = 2n\pi$.

The carbon nanotube quantum dot with side-attached three Majorana fermions (CNTQD-3TSC) remains in the strongly correlated Kondo phase only in the weak coupling strength regime. The CNTQD-3TSC device is determined in the weak coupling limit for $Q = 1(3)e$ by the states $|q_{a(b)}\rangle_{32}$. $|q_w\rangle_{48}$ is the ground state for $Q = 2e$ and is squeezed to the e-h symmetry point in the strong coupling limit. The squeezing mechanism created the new type of the $U^*(1)$ charge symmetry for even number of electrons in the system. In the normal state, this symmetry exists only for the points with the fractional charge in the quantum dot system. Beyond this line, the system defines the low and high energy octuplets $|q_{x(z)}\rangle_8$. One of the interesting points is the opposite charge-leaking mechanism (observed in the general susceptibilities, nonlinear current and shot noise) - directly visible in the structure of the topological qubit states (the leaking states are marked in red in Eqs. (13-14)). The

high energy octuplet $|q_z\rangle_8$ can be expressed, as follows:

$$\begin{aligned}
|q_{-z_1}\rangle &= \frac{1}{\sqrt{8}}(-|000\overline{0}\overline{0}\rangle + |0\uparrow\overline{0}\overline{\uparrow}\overline{0}\rangle - |20\uparrow\overline{0}\underline{\uparrow}\rangle \\
&\color{red}+ |2\uparrow\uparrow\overline{\uparrow}\underline{\uparrow}\rangle - |\downarrow\uparrow\overline{0}\underline{\uparrow}\rangle + |\uparrow 0\overline{0}\underline{\uparrow}\rangle \\
&+ |\uparrow 0\uparrow\overline{0}\overline{0}\rangle - |\uparrow\uparrow\overline{\uparrow}\overline{0}\rangle) \\
|q_{-z_2}\rangle &= \frac{1}{\sqrt{8}}(-|000\overline{0}\underline{\uparrow}\rangle + |0\uparrow\overline{0}\underline{\uparrow}\rangle - |20\uparrow\overline{0}\overline{0}\rangle \\
&\color{red}+ |2\uparrow\uparrow\overline{\uparrow}\overline{0}\rangle + |\downarrow 0\overline{0}\overline{0}\rangle - |\downarrow\uparrow\overline{0}\overline{0}\rangle \\
&+ |\uparrow 0\uparrow\overline{0}\underline{\uparrow}\rangle - |\uparrow\uparrow\overline{\uparrow}\underline{\uparrow}\rangle) \quad (13) \\
|q_{-z_3}\rangle &= \frac{1}{\sqrt{8}}(-|000\overline{0}\overline{0}\rangle + |0\uparrow\overline{0}\overline{0}\rangle - |20\uparrow\overline{0}\underline{\uparrow}\rangle \\
&\color{red}+ |2\uparrow\uparrow\overline{\uparrow}\underline{\uparrow}\rangle + |\downarrow 0\overline{0}\underline{\uparrow}\rangle - |\downarrow\uparrow\overline{0}\underline{\uparrow}\rangle \\
&+ |\uparrow 0\uparrow\overline{\uparrow}\overline{0}\rangle - |\uparrow\uparrow\overline{\uparrow}\overline{0}\rangle) \\
|q_{-z_4}\rangle &= \frac{1}{\sqrt{8}}(-|00\overline{0}\underline{\uparrow}\overline{0}\rangle + |0\uparrow\overline{0}\underline{\uparrow}\overline{0}\rangle - |20\overline{0}\underline{\uparrow}\underline{\uparrow}\rangle \\
&\color{red}+ |2\uparrow\overline{0}\underline{\uparrow}\underline{\uparrow}\rangle + |\downarrow 0\overline{0}\underline{\uparrow}\underline{\uparrow}\rangle - |\downarrow\uparrow\overline{0}\underline{\uparrow}\underline{\uparrow}\rangle \\
&+ |\uparrow 0\overline{0}\overline{0}\rangle - |\uparrow\uparrow\overline{0}\overline{0}\rangle)
\end{aligned}$$

$|q_{-z_1}\rangle, |q_{-z_2}\rangle, |q_{-z_3}\rangle$ and $|q_{-z_4}\rangle$ are the states with opposite configuration in the topological part. The $|2\uparrow n_1n_2n_3\rangle$ states penetrate into the forbidden charge sectors in the CNTQD-3TSC quantum device. The states leak from the triple occupied states on the quantum dot to the charge states above the e-h symmetry point. The mechanism is related to the entanglement of eight spanned states by the tunneling strength between CNTQD and the three Majorana fermions. The charge-leaking states appear around the e-h symmetry point, indicating the strong dependence on the Coulomb interaction. The low energy states, which show the same charge-leaking mechanism can be written as follows:

$$\begin{aligned}
|q_{-x_1}\rangle &= \frac{1}{\sqrt{8}}(|02\overline{0}\overline{0}\rangle - |0\downarrow\overline{0}\overline{0}\rangle + |22\uparrow\overline{\uparrow}\underline{\uparrow}\rangle \\
&- |2\downarrow\uparrow\overline{0}\underline{\uparrow}\rangle - |\downarrow 20\overline{\uparrow}\underline{\uparrow}\rangle + |\downarrow\downarrow\overline{0}\underline{\uparrow}\rangle \\
&- |\uparrow 2\uparrow\overline{\uparrow}\overline{0}\rangle + |\uparrow\downarrow\overline{\uparrow}\overline{0}\rangle) \\
|q_{-x_2}\rangle &= \frac{1}{\sqrt{8}}(|02\overline{0}\underline{\uparrow}\underline{\uparrow}\rangle - |0\downarrow\overline{0}\underline{\uparrow}\underline{\uparrow}\rangle + |22\uparrow\overline{\uparrow}\overline{0}\rangle \\
&- |2\downarrow\uparrow\overline{0}\overline{0}\rangle - |\downarrow 20\overline{\uparrow}\overline{0}\rangle + |\downarrow\downarrow\overline{0}\overline{0}\rangle \\
&- |\uparrow 2\uparrow\overline{\uparrow}\underline{\uparrow}\rangle + |\uparrow\downarrow\overline{\uparrow}\underline{\uparrow}\rangle) \\
|q_{-x_3}\rangle &= \frac{1}{\sqrt{8}}(|02\overline{0}\overline{0}\rangle - |0\downarrow\overline{0}\underline{\uparrow}\underline{\uparrow}\rangle + |22\uparrow\overline{0}\underline{\uparrow}\rangle \\
&- |2\downarrow\uparrow\overline{\uparrow}\underline{\uparrow}\rangle - |\downarrow 20\overline{0}\underline{\uparrow}\rangle + |\downarrow\downarrow\overline{0}\underline{\uparrow}\rangle \\
&- |\uparrow 2\uparrow\overline{0}\overline{0}\rangle + |\uparrow\downarrow\overline{\uparrow}\overline{0}\rangle) \quad (14) \\
|q_{-x_4}\rangle &= \frac{1}{\sqrt{8}}(|02\overline{0}\underline{\uparrow}\overline{0}\rangle - |0\downarrow\uparrow\overline{0}\overline{0}\rangle + |22\overline{0}\underline{\uparrow}\underline{\uparrow}\rangle \\
&- |2\downarrow\overline{0}\underline{\uparrow}\underline{\uparrow}\rangle - |\downarrow 2\uparrow\overline{\uparrow}\underline{\uparrow}\rangle + |\downarrow\downarrow\overline{\uparrow}\underline{\uparrow}\rangle \\
&- |\uparrow 2\overline{0}\overline{0}\rangle + |\uparrow\downarrow\overline{0}\overline{0}\rangle)
\end{aligned}$$

$|q_{-x_1}\rangle$, $|q_{-x_2}\rangle$, $|q_{-x_3}\rangle$ and $|q_{-x_4}\rangle$ are the states with opposite configuration in the topological sector of ket states. Three Majorana fermions do not allow the formation of the Kondo state. These three channels $\{\pm \uparrow, + \downarrow\}$ are involved in interference with the Majorana fermion quantum states. The effect is qualitatively similar to result for the SU(2)-Kondo dot with a side-attached MF, where in the strong coupling limit the quantum conductance at the e-h symmetry point reaches $\mathcal{G} = (3/2)(e^2/h)[110, 119]$.

B. Thermodynamics of the Kondo system

The thermodynamic potential \tilde{F} in the KR-sbMFA approach is given by the partition function \tilde{Z} at the saddle point of the action function \tilde{S} (see [129]):

$$\begin{aligned} \tilde{F} &= -T \ln(\tilde{Z}) = \tilde{F}_b + \tilde{F}_f + \Delta\tilde{F} = U \sum_{\nu} d_{\nu}^{\dagger} d_{\nu} \\ &+ 3U \sum_{l_s} t_{l_s}^{\dagger} t_{l_s} + 6U f^{\dagger} f + \lambda(\mathcal{I} - 1) - \lambda_{l_s} \sum_{l_s} Q_{l_s} \\ &+ \tilde{F}_f + \Delta\tilde{F} \end{aligned} \quad (15)$$

where $\tilde{F}_{b(f)}$ are the bosonic and fermionic parts of the free energy. $\Delta\tilde{F}$ is the correction to the thermodynamic potential (it includes the two- and three-body fluctuations introduced by the FL theory [52, 53, 57]). The \tilde{F}_f can be written in terms of the Matsubara Green's functions using the contour integral method with cut along the real frequency axis [87, 130]:

$$\begin{aligned} \tilde{F}_f &= -T \sum_{\nu, i\omega_n} \ln[\Lambda_{\nu} - i\omega_n] \\ &- T \sum_{m\nu', i\omega_n} a_m \ln[\Lambda_{m\nu'} - i\omega_n] = \sum_{\nu} \int_{-\infty}^{\Lambda_{\nu}} \text{Im}\{X[z]\} dz \\ &+ \sum_{m\nu'} \int_{-\infty}^{\Lambda_{m\nu'}} \text{Im}\{a_m X[z]\} dz \end{aligned} \quad (16)$$

$i\omega_n$ is the Matsubara frequency, and $\Lambda_{\nu(m\nu')}$ are the complex poles of the quasiparticle Kondo resonance. The poles of the channel ν' coupled to the TSC are represented by $\Lambda_{m\nu'}$ where $m = 0, \pm$ ($m = 0$ is associated with the zero Majorana bound state and $m = \pm$ represents the states excited by t). The complex poles can be written in the form $\Lambda_{0\nu'} = (-2i\tilde{\Gamma}_{\nu'} - i\delta + c)/3 + b/(3c)$ and $\Lambda_{\pm\nu'} = (-2i\tilde{\Gamma}_{\nu'} - i\delta \pm ie^{mi(\pi/6)})/3 \pm (ie^{\overline{m}i(\pi/6)}b)/(3c)$, where $c = \sqrt[3]{d + \sqrt{b^3 + d^2}}$, $b = -3\tilde{E}_{\nu'}^2 - 6\tilde{t}^2 + \tilde{\Gamma}_{\nu'}^2$, and $d = -2i\tilde{\Gamma}_{\nu'}(9\tilde{E}_{\nu'}^2 - 9\tilde{t}^2 + \tilde{\Gamma}_{\nu'}^2)$. The coefficients are defined by $a_m = (-\tilde{t}^2 + (\Lambda_{m\nu'} + i\delta)(\Lambda_{m\nu'} + \tilde{E}_{\nu'} + i\delta + i\tilde{\Gamma}_{\nu'}))/\prod_{m' \neq m} (\Lambda_{m\nu'} - \Lambda_{m'\nu'})$. Here $\nu' = + \uparrow, - \uparrow, + \downarrow$ are the quantum numbers addressed to one (two) and three TSCs coupled with CNTQD. $X[z] = (1/(2\pi)) \sum_{\alpha=L,R} \{\Psi_0[1/2 + (z \pm V_{\alpha})/(2\pi iT)] - \ln[W/(2\pi iT)]\}$ where Ψ_0 is the hypergeometric digamma

function, and $X[z]$ is written for the non-equilibrium case.

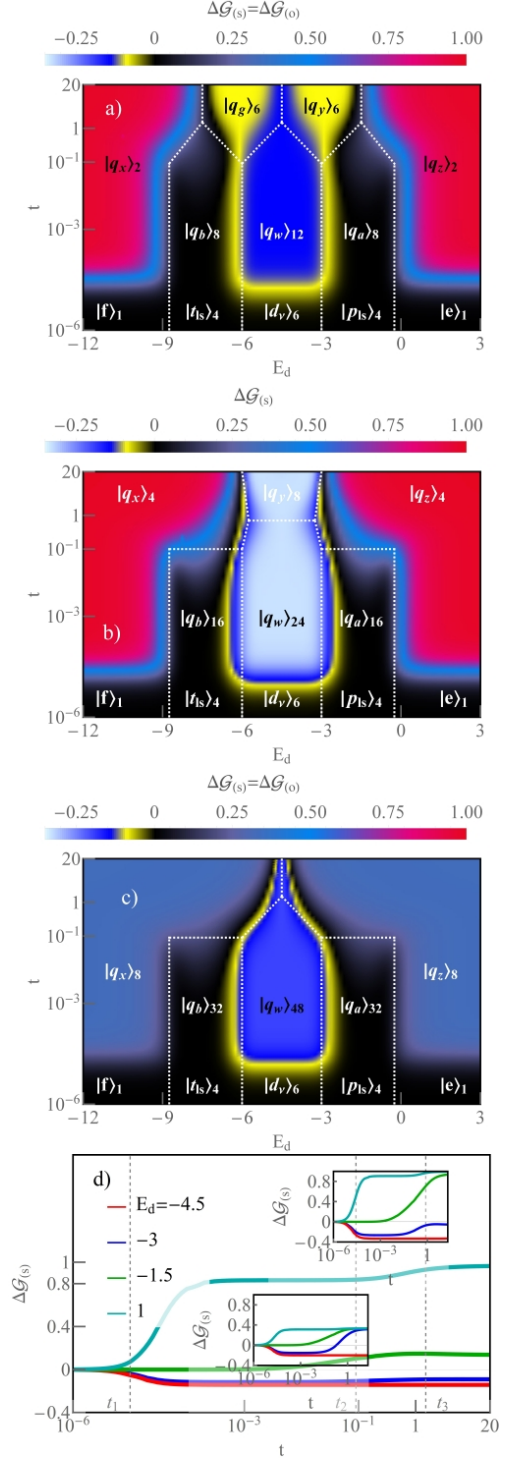


FIG. 8. (Color online) a-c) The density plot of the spin $\Delta\mathcal{G}_s$ and orbital $\Delta\mathcal{G}_o$ polarization of the conductance as a function of E_d and t for CNTQD coupled to single, double and triple MF states. d) t dependence of $\Delta\mathcal{G}_s$ for CNTQD-TSC. The upper and lower insets in Fig. d show $\Delta\mathcal{G}_s$ for QD coupled to 2TSC and 3TSC.

The Fermi liquid theory describes the low-energy regime and is based on the following assumptions: the Kondo singlet elastically scatters conduction electrons, the dressed polarization of the singlet leads to the weak interactions between electrons with different spin orbitals, and the energy of the system is a function of the bare energies E_k and the relative quasiparticle occupancy numbers δn_ν . Using the FL theory [11] and adopting the results of [52, 56], $\Delta\tilde{F}$ can be expressed in the following

general form:

$$\begin{aligned} \Delta\tilde{F} = & -\frac{1}{\pi T_K} \sum_{\nu, E} \left(\alpha_{1,\nu} E + \frac{\alpha_{2,\nu} E^2}{T_K} \right) \delta n_\nu + \\ & \frac{1}{\pi T_K} \sum_{\nu < \nu', EE'} \left(\varphi_{1,\nu\nu'} + \frac{\varphi_{2,\nu\nu'}(E+E')}{2T_K} \right) \delta n_\nu \delta n_{\nu'} + \\ & -\frac{1}{\pi T_K} \sum_{\nu < \nu' < \nu'', EE'E''} \frac{\varphi_{2,\nu\nu'\nu''}}{(N-2)T_K} \delta n_\nu \delta n_{\nu'} \delta n_{\nu''} \end{aligned} \quad (17)$$

where $\alpha_{1,\nu}/\pi = \tilde{\chi}_{\nu\nu}$ ($\alpha_{2,\nu}/\pi = -(1/2)\tilde{\chi}_{\nu\nu\nu}^{[3]}$), $\varphi_{1,\nu\nu'}/\pi = -\tilde{\chi}_{\nu\nu'}$ ($\varphi_{2,\nu\nu'\nu''}/\pi = 2\tilde{\chi}_{\nu\nu'\nu''}^{[3]}$) are the FL coefficients [see [53][57]], which are the functions of the renormalized spin-orbital two- ($\tilde{\chi}_{\nu_1\nu_2}$) and three-body static correlators ($\tilde{\chi}_{\nu_1\nu_2\nu_3}^{[3]}$).

In this approach, we can integrate the energies E by δn_ν in Eq. (17) and find $\Delta\tilde{F}$ in the form intended for sbMFA calculations, determined by the general susceptibilities:

$$\begin{aligned} \Delta\tilde{F} = & -\sum_{\nu} \left(\frac{\tilde{\chi}_{\nu\nu} \delta\tilde{E}_\nu}{2} + \frac{\tilde{\chi}_{\nu\nu\nu}^{[3]} \delta\tilde{E}_\nu^2}{6} \right) \delta\tilde{E}_\nu + \\ & \sum_{\nu < \nu'} \left(-\tilde{\chi}_{\nu\nu'} - \frac{\tilde{\chi}_{\nu\nu'\nu''}^{[3]} (\delta\tilde{E}_\nu + \delta\tilde{E}_{\nu'})}{4} \right) \delta\tilde{E}_\nu \delta\tilde{E}_{\nu'} + \\ & \sum_{\nu < \nu' < \nu''} \frac{\tilde{\chi}_{\nu\nu'\nu''}^{[3]}}{2} \delta\tilde{E}_\nu \delta\tilde{E}_{\nu'} \delta\tilde{E}_{\nu''} \end{aligned} \quad (18)$$

$\tilde{\chi}_{\nu\nu'} = -\frac{\partial^2 \Delta\tilde{F}}{\partial \delta\tilde{E}_\nu^2}$ and $\tilde{\chi}_{\nu\nu'\nu''}^{[3]} = -\frac{\partial^3 \Delta\tilde{F}}{\partial \delta\tilde{E}_\nu \partial \delta\tilde{E}_{\nu'} \partial \delta\tilde{E}_{\nu''}}$. $\delta\tilde{E}_\nu = \sqrt{\langle \tilde{E}_\nu^2 \rangle - \tilde{E}_\nu^2}$ is the fluctuation of the quasiparticle level and $\delta\tilde{E}_\nu \ll \tilde{E}_\nu$. In the weak coupling ansatz ($\tilde{t} \ll t$), $\Delta\tilde{F}$ does not fundamentally change the solution of the equations in the self-consistent sbMFA procedure. Formally, we can prove this by considering $\delta\tilde{E}_\nu = (\Delta\tilde{\Gamma}_\nu) \cot[\pi Q_\nu]$, where $\Delta\tilde{\Gamma}_\nu = \Gamma_\nu \delta z_\nu^2 \ll \Gamma_\nu z_\nu^2$ and $\delta z_\nu = \sqrt{\sum_{\nu'} z_\nu^\dagger \cdot \sum_{\nu'} z_\nu - z_\nu^2}$. The expected values of the boson fields b_n and the constraints λ, λ_{ls} we found by solving the non-equilibrium self-consistent equations from Eq.(3), modified by the $\Delta\tilde{F}$ and completed with an additional equation:

$$\begin{aligned} \frac{\partial \tilde{F}}{\partial b_n} &= \Delta\tilde{\mathcal{H}}_n + \Delta\tilde{E}_n + \frac{\partial \Delta\tilde{F}}{\partial b_n} = 0 \\ \frac{\partial \tilde{F}}{\partial \lambda} &= \mathcal{I} - 1 = 0 \\ \frac{\partial \tilde{F}}{\partial \lambda_{ls}} &= \langle f_{ls}^\dagger f_{ls} \rangle - Q_{ls} + \frac{\partial \Delta\tilde{F}}{\partial \lambda_{ls}} = 0 \\ \frac{\partial \tilde{F}}{\partial \delta\tilde{E}_\nu} &= 0 \end{aligned} \quad (19)$$

Another approach that can be applied to the sbMFA method is presented in [131], where quantum fluctuations are taken into account at the level of individual

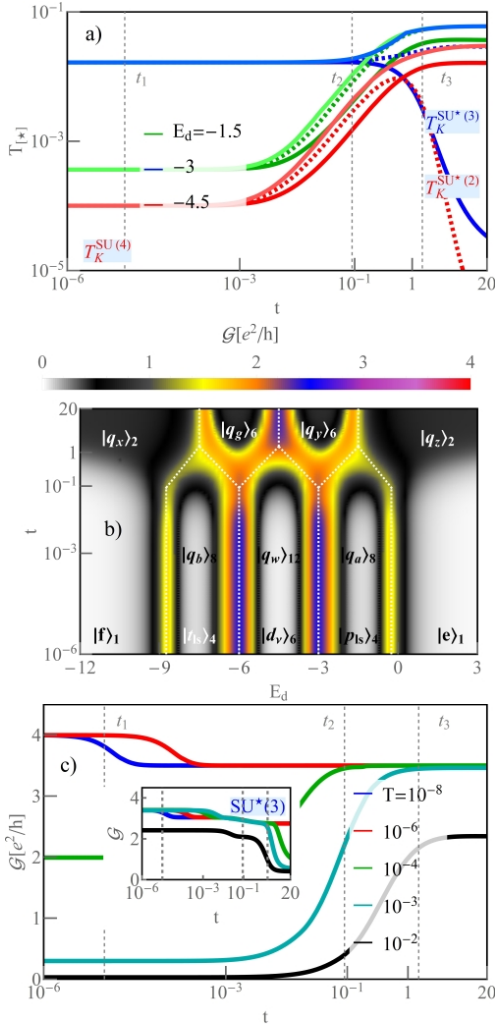


FIG. 9. (Color online) a) The characteristic temperature $T_{[*]}$ as a function of t . $T_K^{SU^*(4)}$, $T_K^{SU^*(3)}$ and $T_K^{SU^*(2)}$ are the Kondo temperatures. The dark, dark dashed, and light lines present $T_{[*]}$ for CNTQD-TSC, CNTQD-2TSC and CNTQD coupled to 3MFs. b) G of the CNTQD-TSC device as a function of E_d and t for finite temperature $T = 10^{-3} > T_K$. c) t dependence of G with increasing T for $E_d = -4.5$ and $E_d = -3$ (inset). The quantum conductances are obtained for CNTQD associated with a single MF.

boson fields and Lagrange multipliers. By integrating over the Grassmann variables and expanding to second order in the boson variables, one obtains Gaussian corrections to the saddle-point action. The alternative methods are based on the spin-rotation invariant (SRI) representation of the auxiliary bosons, where by finding the Z-component and the transverse components of the spin operators, the charge and spin density fluctuations can be obtained in terms of the auxiliary boson fields [132].

Differentiating \tilde{F}_f with respect to \tilde{E}_ν we get the spin-orbital occupation number $n_{\nu=ls}$ in the following way:

$$n_\nu = Q_\nu = \langle f_{ls}^\dagger f_{ls} \rangle^< = \frac{\partial \tilde{F}_f}{\partial \tilde{E}_\nu} = \frac{\delta_\nu}{\pi} \quad (20)$$

$$\sum_\alpha \text{Im} \left\{ \frac{-\ln \left[\frac{W}{2\pi iT} \right] + \Psi_0 \left[1/2 + \frac{\tilde{E}_\nu + i\tilde{\Gamma}_\nu \pm V_\alpha}{2\pi iT} \right]}{2\pi} \right\}.$$

In further calculations (especially for the shot noise and the current in the nonlinear voltage range), the general two- and three-body susceptibilities will be relevant. Thermodynamically, we can define two- and three-body correlation functions as follows $\tilde{\chi}_{\nu_1\nu_2} = \int_0^{1/T} d\tau \langle \delta n_{\nu_2}(\tau) \delta n_{\nu_1}(0) \rangle^<$ and $\tilde{\chi}_{\nu_1\nu_2\nu_3}^{\tilde{\chi}} = -\int_0^{1/T} d\tau_3 \int_0^{1/T} d\tau_2 \langle T_{[\tau]} \delta n_{\nu_3}(\tau_3) \delta n_{\nu_2}(\tau_2) \delta n_{\nu_1}(0) \rangle^<$ (for diagonal parts $\nu_1 = \nu_2 = \nu_3 = \nu$). According to the definitions, the static nonequilibrium partial susceptibilities of the renormalized quasiparticle cloud can be expressed by the following (as used in the NRG calculations [56]):

$$\tilde{\chi}_{\nu\nu} = -\frac{\partial^2 \tilde{F}_f}{\partial \tilde{E}_\nu^2} = \sum_\alpha \text{Im} \left\{ \frac{-\Psi_1 \left[1/2 + \frac{\tilde{E}_\nu + i\tilde{\Gamma}_\nu \pm V_\alpha}{2\pi iT} \right]}{4\pi^2 iT} \right\} \quad V=\underline{T}=0 \quad (21)$$

$$\frac{\tilde{\Gamma}_\nu}{\pi(\tilde{E}_\nu^2 + \tilde{\Gamma}_\nu^2)} = \frac{\tilde{\Gamma}_\nu}{\pi T_{K,\nu}^2} = \frac{\sin^2[\delta_\nu]}{\pi \tilde{\Gamma}_\nu} = \frac{\sin^2[\delta_\nu] \delta n_\nu}{\pi \Gamma \tilde{z}_\nu^2}$$

$$\tilde{\chi}_{\nu\nu\nu}^{[3]} = -\frac{\partial^3 \tilde{F}_f}{\partial \tilde{E}_\nu^3} = \sum_\alpha \text{Im} \left\{ \frac{\Psi_2 \left[1/2 + \frac{\tilde{E}_\nu + i\tilde{\Gamma}_\nu \pm V_\alpha}{2\pi iT} \right]}{8\pi^3 T^2} \right\} \quad V=\underline{T}=0 \quad (22)$$

$$\frac{-2\tilde{\Gamma}_\nu \tilde{E}_\nu}{\pi(\tilde{E}_\nu^2 + \tilde{\Gamma}_\nu^2)^2} = \frac{-2\tilde{\Gamma}_\nu \tilde{E}_\nu}{\pi T_{K,\nu}^4} = \frac{-2 \cos[\delta_\nu] \sin^3[\delta_\nu]}{\pi \tilde{\Gamma}_\nu^2}$$

The diagonal $\nu' = \nu$ static susceptibilities, according to Yamada and Yosida [133] are determined by the renormalization factor $1/\tilde{z}_\nu^2$. In the channel directly coupled to the Majorana fermion ν' , two and three-body correlation

functions can be expressed as follows:

$$\tilde{\chi}_{\nu\nu'} \quad V=\underline{T}=0 \quad \frac{\tilde{\Gamma}_{\nu'} + \frac{\tilde{z}_{\nu'}^2}{\delta}}{\pi(\tilde{E}_{\nu'}^2 + \tilde{\Gamma}_{\nu'}^2 + \frac{2\tilde{z}_{\nu'}^2 \tilde{\Gamma}_{\nu'}}{\delta})} \quad (23)$$

$$\tilde{\chi}_{\nu\nu'\nu'}^{[3]} = \frac{\partial \tilde{\chi}_{\nu\nu'}}{\partial \tilde{E}_{\nu'}} = \frac{-2(\tilde{\Gamma}_{\nu'} + \frac{\tilde{z}_{\nu'}^2}{\delta}) \tilde{E}_{\nu'}}{\pi(\tilde{E}_{\nu'}^2 + \tilde{\Gamma}_{\nu'}^2 + \frac{2\tilde{z}_{\nu'}^2 \tilde{\Gamma}_{\nu'}}{\delta})^2} \quad (24)$$

In both cases the two-body static correlation functions are equal to the quasiparticle density of states at the Fermi level: $\tilde{\chi}_{\nu\nu} = \langle \langle f_\nu; f_\nu^\dagger \rangle \rangle|_{E=0} = \tilde{g}_\nu(0)$ ($\tilde{\chi}_{\nu\nu'} = \tilde{g}_{\nu'}$). The diagonal and off-diagonal two- and three-body correlation functions result from the FL theory and the spin-orbital fluctuations can be obtained by using the derivatives in the following form:

$$\tilde{\chi}_{\nu\nu} = -\frac{\partial^2 \Delta \tilde{F}}{\partial \delta \tilde{E}_\nu^2} = \tilde{\chi}_{\nu\nu} + \sum_{\nu'} \tilde{\chi}_{\nu\nu'\nu'}^{[3]} \delta \tilde{E}_{\nu'} \quad \delta \tilde{E}_{\nu'} \approx 0 \quad \tilde{\chi}_{\nu\nu}$$

$$\tilde{\chi}_{\nu\nu\nu}^{[3]} = -\frac{\partial^3 \Delta \tilde{F}}{\partial \delta \tilde{E}_\nu^3} = \tilde{\chi}_{\nu\nu\nu}^{[3]} = \frac{\partial \tilde{\chi}_{\nu\nu}}{\partial \tilde{E}_\nu}$$

$$\tilde{\chi}_{\nu\nu'} = -\frac{\partial^2 \Delta \tilde{F}}{\partial \delta \tilde{E}_\nu \partial \delta \tilde{E}_{\nu'}} = \tilde{\chi}_{\nu\nu'} + \tilde{\chi}_{\nu\nu'\nu'}^{[3]} \delta \tilde{E}_{\nu'} + \tilde{\chi}_{\nu'\nu\nu}^{[3]} \delta \tilde{E}_\nu$$

$$-(1/2) \sum_{\nu'' \neq (\nu, \nu')} \tilde{\chi}_{\nu\nu'\nu''}^{[3]} \delta \tilde{E}_{\nu''} \quad \delta \tilde{E}_{\nu(\nu', \nu'')} \approx 0 \quad \tilde{\chi}_{\nu\nu'} =$$

$$-(W_{\nu\nu'} - 1) \sqrt{\tilde{\chi}_{\nu\nu} \tilde{\chi}_{\nu'\nu'}} \quad (25)$$

$$\tilde{\chi}_{\nu\nu'\nu'}^{[3]} = -\frac{\partial^3 \Delta \tilde{F}}{\partial \delta \tilde{E}_\nu \partial \delta \tilde{E}_{\nu'}^2} = \tilde{\chi}_{\nu\nu'\nu'}^{[3]} = \frac{\partial \tilde{\chi}_{\nu\nu'}}{\partial \tilde{E}_{\nu'}} =$$

$$-(W_{\nu\nu'} - 1) \frac{\partial \sqrt{\tilde{\chi}_{\nu\nu} \tilde{\chi}_{\nu'\nu'}}}{\partial \tilde{E}_{\nu'}} + W_{\nu\nu'} \sqrt{\tilde{\chi}_{\nu\nu} \tilde{\chi}_{\nu'\nu'}} =$$

$$-K_{\nu\nu'} \tilde{\chi}_{\nu'\nu'\nu'}^{[3]}$$

where $W_{\nu\nu'} \equiv 1 - \tilde{\chi}_{\nu\nu'} / \sqrt{\tilde{\chi}_{\nu\nu} \tilde{\chi}_{\nu'\nu'}}$ is the Wilson ratio [10, 17, 29, 58, 130]. By definition, $W_{\nu\nu'}$ is expressed by the susceptibilities and, in its original form, is experimentally determinable by the ratio of the spin susceptibility $\chi_{(s)}$ and the linear coefficient of the specific heat γ_N , as will be discussed later in this subsection. Two-body correlation functions written on the basis of $\Delta \tilde{F}$ are more general and include the correction for the fluctuation $\delta \tilde{E}_\nu$. For the systems where $\delta \tilde{E}_\nu \sim \tilde{E}_\nu$ the additive part can play a crucial role. In practice, to compute 2-body even correlation functions $\tilde{\chi}_{\nu\nu'}$ and 3-body odd correlation functions $\tilde{\chi}_{\nu\nu'\nu'}$, we can formally adopt the Random Phase Approximation (RPA) method and its correction for non-zero frequency susceptibility [130, 134]. This alternative approach introduces the imaginary and real parts of the higher-order correlations and will be useful for discussing of the frequency dependent shot noise and the current. In this paper we have proposed to use the weak coupling approach to calculate the Wilson ratios and consequently the higher-order correlation functions. The weak coupling approach is based on the low renormalization coupling strength of the Kondo resonance to

the normal electrodes (z_ν^2) ($t_0 \ll t_0$). Finally, in the general case for SU(N) Anderson model, we found that the Wilson ratio $W_{\nu\nu'} = 1 - \tilde{\chi}_{\nu\nu'}/\sqrt{\tilde{\chi}_{\nu\nu}\tilde{\chi}_{\nu'\nu'}} \approx 1 + 1/(N-1)$ and as we can see $-\tilde{\chi}_{\nu\nu'}/\sqrt{\tilde{\chi}_{\nu\nu}\tilde{\chi}_{\nu'\nu'}} = 1/(N-1)$ is the correction from two-particle correlators. $W_{\nu\nu'} > 1$ is the consequence of the finite Coulomb (residual) interaction between the quasiparticles and depends on the degree of degeneracy N [58]. In general terms, using the weak coupling ansatz and exact expression for the partition function Z_N , the Wilson ratio can be written as follows:

$$W_{\nu\nu'} - 1 = \frac{n_\nu n_{\nu'} - n_{\nu\nu'}}{\sqrt{\delta n_\nu^2 \delta n_{\nu'}^2}} = \quad (26)$$

$$\frac{Q_\nu Q_{\nu'} - Q_{\nu\nu'}}{\sqrt{Q_\nu(I - Q_\nu)Q_{\nu'}(I - Q_{\nu'})}} = \frac{\delta Q_{\nu\nu'}}{\Delta Q_{\nu\nu'}} \quad (27)$$

$$K_{\nu\nu'} = \frac{\delta Q_{\nu\nu'}}{\delta n_{\nu'}^2} \quad (27)$$

where Q_ν is the charge expressed by the boson fields operators (averaged over the time, in the static susceptibilities) and $Q_{\nu\nu'} = \sum_{\nu\nu''} b_{\nu\nu''}^2 I$ is the sum over all boson fields amplitudes at which the two-particle state $\nu\nu'$ exists. Surprisingly, the ansatz quantitatively reproduces the NRG result, which use the self-energy and the Ward identities to calculate 2(3)-body quantities [56, 135]. $\dot{W}_{\nu\nu'}$ in Eq. (25) is the derivative of the Wilson ratio and plays the important role in the 3-body correlation function. Formally, $\dot{W}_{\nu\nu'}$ can be expressed in terms of $K_{\nu\nu'}$, but using the weak coupling approach, it can be defined as:

$$\dot{W}_{\nu\nu'} = -\frac{\partial W_{\nu\nu'}}{\partial \tilde{E}_{\nu\nu'}} = \quad (28)$$

$$\frac{\delta n_{\nu'}^2 \delta Q_{\nu\nu'} [Q_\nu(Q_\nu + Q_{\nu'} - I - 2Q_{\nu\nu'}) + Q_{\nu\nu'}]}{2\Delta Q_{\nu\nu'}^3}$$

Using the two-body correlators, we can write down the charge, spin and pseudospin susceptibilities in the forms (following A.C. Hewson et al. in [58]): $\chi_{(c)} = \int_0^{1/k_B T} d\tau \langle \delta Q(\tau) \delta Q(0) \rangle < = \sum_{lsl's'} \int_0^{1/k_B T} d\tau \langle \delta n_{ls}(\tau) \delta n_{l's'}(0) \rangle < = \sum_{\nu=ls} (1 - \sum_{\nu' \neq \nu} \tilde{U}^{\nu\nu'} \tilde{q}_{\nu'}) \tilde{q}_\nu = \sum_{\nu\nu'} \tilde{\chi}_{\nu\nu'}$, $\chi_{(s)} = \sum_l \int_0^{1/k_B T} d\tau \langle \delta S_l^Z(\tau) \delta S_l^Z(0) \rangle < = \frac{1}{4} \sum_{ls} s\bar{s} \int_0^{1/k_B T} d\tau \langle \delta n_{ls}(\tau) \delta n_{ls}(0) \rangle < = \frac{1}{4} \sum_{\nu=ls} (1 + \tilde{U}^{\nu\nu'} \tilde{q}_{\nu'=l\bar{s}}) \tilde{q}_\nu = \frac{1}{4} \sum_{lss's'} s\bar{s}' \tilde{\chi}_{lsls'}$ and $\chi_{(ps)} = \frac{1}{4} \int_0^{1/k_B T} d\tau \langle \delta T^Z(\tau) \delta T^Z(0) \rangle < = \frac{1}{4} \sum_{lsl's'} ll' \int_0^{1/k_B T} d\tau \langle \delta n_{ls}(\tau) \delta n_{l's'}(0) \rangle < = \frac{1}{4} \sum_{\nu=ls} (1 - \tilde{U}^{\nu\nu'} \tilde{q}_{\nu'=l\bar{s}} + \sum_{\nu'=l\bar{s}} \tilde{U}^{\nu\nu'} \tilde{q}_{\nu'}) \tilde{q}_\nu = \frac{1}{4} \sum_{\nu=ls\nu'=l's'} ll' \tilde{\chi}_{\nu\nu'}$, where $\delta n_\nu = n_\nu - \langle n_\nu \rangle$, $\delta Q = \sum_\nu n_\nu - \langle \sum_\nu n_\nu \rangle$, $\delta S_l^Z = (1/2)(n_{l\uparrow} - n_{l\downarrow} - \langle n_{l\uparrow} - n_{l\downarrow} \rangle)$ and $\delta T^Z = (1/2)(n_+ - n_- - \langle n_+ - n_- \rangle)$ are the total charge, spin and pseudospin fluctuations. Consequently, the residual quasiparticle interaction is given by $\tilde{U}^{\nu\nu'} \equiv -\tilde{\chi}_{\nu\nu'}/(\tilde{\chi}_{\nu\nu}\tilde{\chi}_{\nu'\nu'})$ [33, 56, 58]. The

linear coefficient of the quasiparticle specific heat for SU(4) Kondo symmetry in a Fermi liquid theory is given by $\gamma_N = \frac{\pi^2}{3} \sum_{\nu=ls} \tilde{q}_\nu$. For a fully symmetric SU(4) Kondo effect, the spin, charge and pseudospin susceptibilities are determined by the quasiparticle two-body correlation function as follows: $\chi_{(c)} = \tilde{\chi}_{\nu\nu} [1 - (\tilde{U}^{\nu\nu} + 2\tilde{U}^{\nu\bar{\nu}}) \tilde{\chi}_{\nu\nu}] = \tilde{\chi}_{\nu\nu} [1 - 3/(N-1)] \approx 0$, $\chi_{(s)} = \tilde{\chi}_{\nu\nu} [1 + \tilde{U}^{\nu\nu} \tilde{\chi}_{\nu\nu}] = \tilde{\chi}_{\nu\nu} [1 + 1/(N-1)] = \tilde{\chi}_{\nu\nu} W_{(s)}$ and $\chi_{(ps)} = \tilde{\chi}_{\nu\nu} [1 - (\tilde{U}^{\nu\nu} - 2\tilde{U}^{\nu\bar{\nu}}) \tilde{\chi}_{\nu\nu}] = \tilde{\chi}_{\nu\nu} [1 + 1/(N-1)] = \tilde{\chi}_{\nu\nu} W_{(ps)}$. For the fully symmetric SU(4) Kondo state, both Wilson ratios are the equal $W_{ps} = W_s = W_{\nu\nu'} = (\pi^2 N \chi_{(s)}) / (3\gamma_N) = (4/3)$ [58].

To discuss the expected value of the local pseudospin for SU(4) symmetry, we used a quadratic Casimir operator, which is the bilinear sum of $N^2 - 1$ generators belonging to the Lie group. The quadratic Casimir operator is proportional to the fluctuations of the local pseudospin momentum. For the SU(4) Kondo effect, the pseudospin is screened by the conduction electrons. Based on the Lie algebra generators \hat{O} we can define the total local Casimir operator: $C = \sum_{i\nu\nu'} d_\nu^\dagger \hat{O}_{\nu\nu'}^i d_{\nu'}$, where $i = 1 \dots N^2 - 1$ [43, 46]. The Z-component of the Casimir operator can be constructed from $N - 1$ diagonal Lie generators of SU($N = 4$) symmetry as follows: $C_Z = \sum_{i=3,8,15\nu\nu'} d_\nu^\dagger \hat{O}_{\nu\nu'}^i d_{\nu'}$ [136]. Finally, we can express the total quadratic Casimir operator and its Z-component in

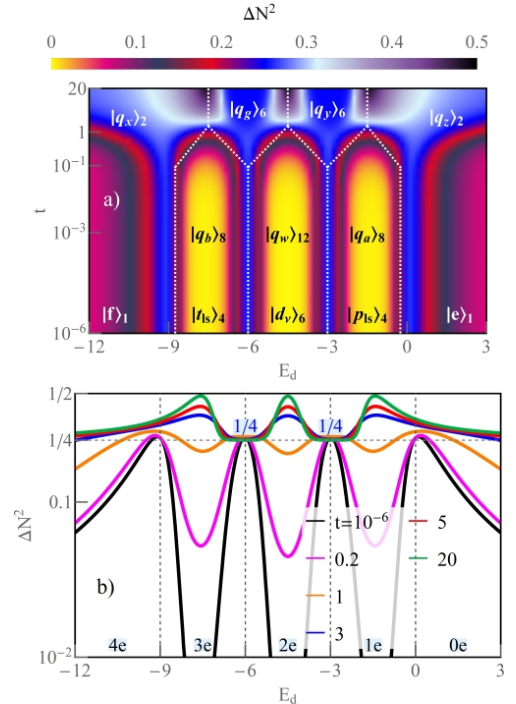


FIG. 10. (Color online) a) The density plot of the charge fluctuation ΔN^2 as function of E_d and t for the CNTQD-TSC hybrid device. b) The E_d dependence of ΔN^2 with increasing of tunnel coupling to a single TSC. $\Delta N^2 = 1/4$ shows the saturation value in the strong coupling with MF.

the following way: $C^2 = (15/8)(\sum_\nu Q_\nu - (2/3)\sum_\nu Q_\nu \cdot Q_{\bar{\nu}})$, and $C_Z^2 = (3/8)(\sum_\nu Q_\nu - (2/3)\sum_\nu Q_\nu \cdot Q_{\bar{\nu}}) = (1/4)(\sum_{\nu\nu'} \chi_{\nu\nu'} - \sum_\nu \chi_{\nu\bar{\nu}})$. The local Z-component, depending on the coupling strength with 1TSC, 2TSC or 3TSC. For further discussion, we can express C_Z^2 in the boson fields operators and separate in the following sum $C_Z^2 = C_{Z(K)}^2 + C_{Z(M)}^2$, where $C_{Z(K)}^2$ describes the fluctuations in the normal (Kondo-like) channel and $C_{Z(M)}^2$ is related to the Majorana fermion part. For the CNTQD-1TSC device, the relations of the quadratic Casimir operators can be expressed as:

$$C_{Z(K)}^2 = (1/3)(p_{\uparrow\downarrow}^2 + \sum_s p_{-s}^2 + \sum_\nu d_\nu^2 + \bar{t}_{\uparrow\downarrow}^2 + \sum_s \bar{t}_{-s}^2) \quad (29)$$

$$C_{Z(M)}^2 = (1/24)(9p_{\uparrow\downarrow}^2 + p_{\uparrow\downarrow}^2 + \sum_s p_{-s}^2 + 4\sum_\nu d_\nu^2 + \bar{t}_{\uparrow\downarrow}^2 + 9\bar{t}_{\uparrow\downarrow}^2 + \sum_s \bar{t}_{-s}^2). \quad (30)$$

C_Z^2 for two Majoranas that are coupled to CNTQD can be obtained in the following way:

$$C_{Z(K)}^2 = (1/4)(\sum_l p_{l\downarrow}^2 + \sum_l d_l^2 + d_{\uparrow\downarrow}^2 + d_{\downarrow\uparrow}^2 + \bar{t}_{\uparrow\downarrow}^2 + \bar{t}_{\downarrow\uparrow}^2) \quad (31)$$

$$C_{Z(M)}^2 = (1/8)(3\sum_l p_{l\uparrow}^2 + \sum_l p_{l\downarrow}^2 + 2\sum_l d_l^2 + 2d_{\uparrow\downarrow}^2 + 2d_{\downarrow\uparrow}^2 + 4\sum_s d_{ss}^2 + \bar{t}_{\uparrow\downarrow}^2 + 3\bar{t}_{\uparrow\downarrow}^2 + 3\bar{t}_{\downarrow\uparrow}^2 + \bar{t}_{\downarrow\uparrow}^2). \quad (32)$$

The quadratic Casimir operator for the CNTQD-3TSC system can be written using the following formulas:

$$C_{Z(K)}^2 = (1/24)(\sum_s p_{\uparrow s}^2 + p_{\uparrow\downarrow}^2 + 9p_{\downarrow\downarrow}^2 + 4\sum_\nu d_\nu^2 + \sum_s \bar{t}_{\uparrow s}^2 + \bar{t}_{\uparrow\downarrow}^2 + 9\bar{t}_{\downarrow\downarrow}^2) \quad (33)$$

$$C_{Z(M)}^2 = (1/3)(\sum_s p_{\uparrow s}^2 + p_{\uparrow\downarrow}^2 + \sum_\nu d_\nu^2 + \sum_s \bar{t}_{\uparrow s}^2 + \bar{t}_{\uparrow\downarrow}^2). \quad (34)$$

In the calculations we used the invariant of the two-body susceptibility $\chi_{(z)}$, which is equal to C_Z^2 in the isolated (local) case (or when $T \gg T_K$). $\chi_{(z)}$ is the quantum metric in the two-body correlation space and can be expressed as follows $\chi_{(z)} = (1/4)(\sum_\nu \tilde{\chi}_{\nu\nu} - \sum_{\nu' \neq \nu} \tilde{\chi}_{\nu\nu'})$. The charge susceptibility is given by: $\chi_{(c)} = \sum_{\nu\nu'} \tilde{\chi}_{\nu\nu'}$. The three-body susceptibility can be written as $\chi_{(z)}^{[3]} = (1/4)(\sum_\nu \tilde{\chi}_{\nu\nu\nu}^{[3]} - \sum_{\nu' \neq \nu} \tilde{\chi}_{\nu\nu'\nu'}^{[3]})$ - in fact, the cubic Casimir operator C^3 would be more appropriate. However, after expanding this in terms of the conformal Lie group generators, it turns out that it is

simply proportional to the quadratic Casimir (by the explicit relation $C^3 = (d/2)C^2$). Formally, the conformal group in d dimensions (in our case $d = 4$) consists of a single dilation operator \hat{D} , d translations \hat{P} , d special conformal transformations \hat{K} and $d(d-1)/2$ rotations \hat{J} [137].

Using the quadratic Casimir operator we have computed $T_{[\star]}\chi_{(z)}$, $T_{[\star]}\chi_{(c)}$ and $T_{[\star]}^2\chi_{(z)}^{[3]}$ which are quantized at zero temperature. $T_{[\star]} = \min\{T_{K,\nu}\}$ is the scaling characteristic energy. In the Fermi liquid phase it corresponds to the Kondo temperature. $T_{[\star]}\chi_{(z,c)}(T = 0K)$ and $-T_{[\star]}^2\chi_{(z)}^{[3]}(0)$ are the frozen effective spin/charge and the three-body correlator in the system [60]. Last year the physicists crossed the Rubicon, and measured the spin susceptibility in the SU(2) Kondo quantum dot, in fact it was the fundamental measurement of the spin of the Kondo impurity, using the charge-sensing method [138]. One of the most important results in this matter is the measurement of the three-body correlations, indirectly using the lock-in technique to detect linear and nonlinear shot noise [60].

C. Transport measurements

At the Fermi level, the system in Fig. 1 satisfies the Friedel sum rule, and the linear conductance for the normal (Kondo) channel can be written as follows:

$$\mathcal{G}_\nu(V) = \frac{e^2}{h} \sum_\alpha \text{Re} \left\{ \frac{\tilde{\Gamma}_\nu \Psi_1 \left[\frac{1}{2} + \frac{\tilde{E}_\nu + i\tilde{\Gamma}_\nu \pm V_\alpha}{2\pi iT} \right]}{4\pi T} \right\} \\ v \equiv T=0 \quad \frac{e^2}{h} \frac{\tilde{\Gamma}_\nu^2}{T_{K,\nu}^2} = \frac{e^2}{h} \sin^2[\delta_\nu] \quad (35)$$

where the quantum conductance in the ν' channels that are coupled to the TSC is given by :

$$\mathcal{G}_{\nu'}(V) = \frac{e^2}{h} \sum_{\alpha m} \text{Re} \left\{ \frac{\tilde{\Gamma}_{\nu'} a_m \Psi_1 \left[\frac{1}{2} + \frac{\Lambda_{m\nu'}^* \pm V_\alpha}{2\pi iT} \right]}{4\pi T} \right\} \\ v \equiv T=0 \quad \frac{e^2}{h} \frac{\tilde{\Gamma}_{\nu'} (\tilde{\Gamma}_{\nu'} + \frac{\tilde{t}_{\nu'}}{\delta})}{\tilde{E}_{\nu'}^2 + \tilde{\Gamma}_{\nu'}^2 + \frac{2\tilde{t}_{\nu'}^2 \tilde{\Gamma}_{\nu'}}{\delta}} \\ = \frac{e^2}{h} \frac{\delta \tilde{\Gamma}_{\nu'} + \tilde{t}_{\nu'}^2}{\delta \tilde{\Gamma}_{\nu'} \csc^2[\delta_{\nu'}] + 2\tilde{t}_{\nu'}^2}. \quad (36)$$

The total conductance can be expressed as $\mathcal{G} = \sum_\nu \mathcal{G}_\nu + \sum_{\nu'} \mathcal{G}_{\nu'}$ where $\nu' = \pm 1 \uparrow, +1 \downarrow$ and depends on the number of the spin-orbital channels coupled to the TSC. The quantum conductance \mathcal{G} develops from the current formula in the following way $\mathcal{G}(0) = dI/dV|_{V \rightarrow 0}$. The thermal fluctuations (thermal noise) can be related to the linear conductance via the fluctuation-dissipation theorem and the nonlinear temperature part, as shown in [56]: $S_T = 4k_B T \sum_\nu (\mathcal{G}_\nu(0) - (e^2/h) \sum_\nu c_{T,\nu} (\pi k_B T)^2 + \dots)$,

where $c_{T,\nu}$ is the temperature coefficient explicitly expressed by the higher-order correlations. In our analysis we have focused on the zero temperature shot noise and, therefore the equilibrium fluctuations are negligible in the further discussion of the shot noise S . Using the Keldysh formalism for nonequilibrium Green's functions, and zero-frequency limit for the shot noise, we can write the zero temperature current I and the shot noise S as a function of the unitary transmission T_ν for the ν channel, in the Landauer-Büttiker form:

$$I = \langle \hat{I} \rangle = (e/h) \int_{-|V|/2}^{|V|/2} \sum_\nu T_\nu(E) dE \quad (37)$$

$$\begin{aligned} S(t, t') &= (1/4) \sum_\alpha S_{\alpha\alpha}^>(t, t') + S_{\alpha\alpha}^<(t, t') \\ -S_{\alpha\bar{\alpha}}^>(t, t') - S_{\alpha\bar{\alpha}}^<(t, t') &= S(\tau, 0) \\ &= (1/2) \langle \{ \hat{I}(\tau), \hat{I}(0) \} \rangle - I^2 \\ S &= \lim_{\omega \rightarrow 0} 2 \int_{-\infty}^{+\infty} e^{i\omega\tau} S(\tau, 0) d\tau \quad (38) \\ &= 2(e^2/h) \int_{-|V|/2}^{|V|/2} \sum_\nu T_\nu(E) [1 - T_\nu(E)] dE \end{aligned}$$

where $\hat{I} = \frac{ie}{\hbar} [\tilde{\mathcal{H}}, \sum_{k\alpha=L(R)\nu} \pm(1/2)c_{k\alpha\nu}^\dagger c_{k\alpha\nu}]$ is the current operator. Applying the Wick theorem, to compute contour-ordered auto and cross-correlation functions, the shot noise can be expressed in the following way $S_{\alpha\alpha'}^{>(<)}(t, t') = 2(\frac{ie}{\hbar})^2 \sum_{kq\nu\nu'} \tilde{t}_{0\nu} \tilde{t}_{0\nu'} [G_{\nu, q\alpha'\nu'}^{>(<)}(t, t') G_{\nu', k\alpha\nu}^{<(>)}(t', t) + G_{k\alpha\nu, \nu'}^{>(<)}(t, t') G_{q\alpha'\nu', \nu}^{<(>)}(t', t) - G_{\nu, \nu'}^{>(<)}(t, t') G_{q\alpha'\nu', k\alpha\nu}^{<(>)}(t', t) - G_{k\alpha\nu, q\alpha'\nu'}^{>(<)}(t, t') G_{\nu', \nu}^{<(>)}(t', t)]$. Two-correlation functions in S are decoupled in Hartree-Fock approximation (HFA) for two-particle Green's functions [139]. T_ν in Eqs. (37-38) is the transmission, expressed by the formulas for decoupled and coupled channel to TSC in the following form: $T_\nu(E) = \tilde{\Gamma}_\nu^2 / [(E - \tilde{E}_\nu)^2 + \tilde{\Gamma}_\nu^2]$ and $T_{\nu'}(E) = -\tilde{\Gamma}_{\nu'} \text{Im}[G_{\nu'\nu'}^R]$, where $G_{\nu'\nu'}^R = \hat{G}_{11}^R$ is the retarded Green's function in the matrix Eq. (6). In general, we have developed the current and the shot noise in the series: $I = I_0 V - \sum_\nu c_{V,\nu} V^3 + 0[V^5]$ and $S = S_0 V + \sum_\nu c_{S,\nu} V^3 + 0[V^5]$ where $F_0 = \lim_{V \rightarrow 0} S_0 / 2eI_0 = \frac{\sum_\nu T_\nu(0)(1-T_\nu(0))}{\sum_\nu T_\nu(0)}$ is the linear Fano factor expressed by the linear shot noise S_0 and the current I_0 . For identical transmissions in both spin-orbital channel ($\nu = \nu'$), the linear Fano factor can be written as follows: $F_0 = 1 - T_\nu(0)$. The nonlinear contribution is described by $F_K = |S - S_0| / (2e|I - I_0|) = |S_K| / (2e|I_K|) = \frac{\delta S_K}{\delta I_K} = \frac{e^*}{e}$. S_K and I_K measurements contain the information about the effective charge e^* of the current-carrying particles. The charge differs from the electron charge e . The nonlinear shot noise S_K and the nonlinear current I_K are defined as the absolute values and scaled by the characteristic temperature expression: $\delta S_K = T_{[*]}^2 |S_K|$ and $\delta I_K = 2eT_{[*]}^2 |I_K|$. These definitions simplify the following discussion, emphasize

the Fermi liquid behavior, and are formulated by the expressions of the two- and three-body correlation functions. The coefficients can be written as separate parts of the sum: $c_{V,\nu} = c_{V,\nu}|_{W_{\nu\nu'}-1=0} + \delta c_{V,\nu}|_{W_{\nu\nu'}-1>0}$ and $c_{S,\nu} = c_{S,\nu}|_{W_{\nu\nu'}-1=0} + \delta c_{S,\nu}|_{W_{\nu\nu'}-1>0}$, where $\delta c_{V(S),\nu}|_{W_{\nu\nu'}-1>0}$ is the correction developed from the residual interaction $\tilde{U}^{\nu\nu'}$ between the Kondo quasiparticles. $\delta c_{S,\nu}|_{W_{\nu\nu'}-1=0}$ is related to the elastic scattering processes and $\delta c_{S,\nu}|_{W_{\nu\nu'}-1>0}$ includes the elastic and inelastic scattering contribution [52, 55, 59]. If we write the equations in the series: $T_\nu \approx i_1 + i_2 E + i_2 E^2 + 0[E^3]$, $T_\nu(1 - T_\nu) \approx s_1 + s_2 E + s_2 E^2 + 0[E^3]$, we can find that $I_0 = i_1$, $c_{V,\nu}|_{W_{\nu\nu'}-1=0} = i_2/12$ and $S_0 = s_1$, $c_{S,\nu}|_{W_{\nu\nu'}-1=0} = s_2/12$. Based on the main results of [56], where the authors found the nonlinear transport coefficients to the shot noise and the current for the SU(N) Anderson model using vertex corrections, we adopted the general expressions to calculate the nonlinear Fano factor $F_K = |c_S|/|c_V| = \sum_\nu |c_{S,\nu}| / \sum_\nu |c_{V,\nu}|$. The transport coefficients are determined by the static linear and nonlinear susceptibilities at low energies. The authors showed that the Ward identities, between the casual self-energies and the Feynman diagrams for the Keldysh vertex function of the zero temperature formalism, can be expressed in terms of the collision integrals. The formulas derived in [56], as suggested by the authors are applicable to a wide class of quantum dots without particle-hole or time-reversal symmetry. According to [56], the coefficients $c_{V,\nu}$ and $c_{S,\nu}$ can be expressed in the following way:

$$\begin{aligned} c_{S,\nu} &= \frac{\pi^2}{12} (\cos[4\delta_\nu] \chi_{\nu\nu}^2 + (2 + 3\cos[4\delta_\nu]) \sum_{\nu' \neq \nu} \chi_{\nu\nu'}^2 + \\ &4 \sum_{\nu' \neq \nu} \cos[2\delta_\nu] \cos[2\delta_{\nu'}] \chi_{\nu\nu'}^2 \quad (39) \end{aligned}$$

$$\begin{aligned} &+ 3 \sum_{\nu' \neq \nu} \sum_{\nu'' \neq \nu, \nu'} \sin[2\delta_\nu] \sin[2\delta_{\nu'}] \chi_{\nu\nu''} \chi_{\nu'\nu''} \\ &- (\chi_{\nu\nu\nu} + 3 \sum_{\nu' \neq \nu} \chi_{\nu\nu'\nu'}) \frac{\sin[4\delta_\nu]}{4\pi} \\ c_{V,\nu} &= \frac{\pi^2}{12} (-\cos[2\delta_\nu] (\chi_{\nu\nu}^2 + 5 \sum_{\nu' \neq \nu} \chi_{\nu\nu'}^2) + \\ &(\chi_{\nu\nu\nu} + 3 \sum_{\nu' \neq \nu} \chi_{\nu\nu'\nu'}) \frac{\sin[2\delta_\nu]}{2\pi}). \quad (40) \end{aligned}$$

The factors are calculated for symmetric coupling to the normal electrodes $\tilde{\Gamma}_L = \tilde{\Gamma}_R$ and are derived from the Keldysh vertex corrections to the current and the shot noise using the principles of Fermi liquid theory. The main contribution to the current and shot noise coefficients is determined by the charge (in the phase shift δ_ν), 2-body (susceptibilities) and 3-body correlation functions. In connection with the previous results, the authors introduced the higher-order fluctuations into the shot-noise formula and expressed the transport coefficients in the elegant form of the general static sus-

ceptibilities [56]. In this article we propose to calculate the dressed susceptibilities ($\tilde{\chi}_{\nu_1\nu_2}$) and the 3-body correlations ($\tilde{\chi}_{\nu_1\nu_2\nu_3}^{[3]}$) using the extended K-R slave boson mean-field approach [40, 130, 140] and the weak coupling ansatz to calculate the Wilson ratio ($\tilde{t}_0 \ll t_0$).

In this paper, we also theoretically investigate the thermoelectric power using the Onsager equations [32]. In the linear response theory, the electric and thermal currents can be expressed as: $I = e^2 \sum_{\nu} L_{\nu}^{(0)} \delta V - (e/T) \sum_{\nu} L_{\nu}^{(1)} \delta T$ and $I_Q = -e \sum_{\nu} L_{\nu}^{(1)} \delta V + (1/T) \sum_{\nu} L_{\nu}^{(2)} \delta T$, where $\delta V = V_L - V_R$ and $\delta T = T_d - T_s$ are the difference of the bias voltage and the temperature gradient. Finally, we can write the conductance \mathcal{G} and the thermoelectric power $\mathcal{S} = (\delta V / \delta T)|_{T=0}$ using the integral $L_{\nu}^{(n)} = T \sum_{\alpha} \int_{-\infty}^{+\infty} (E - V_{\alpha})^n T_{\nu}(E) \left(-\frac{\partial f_{\alpha}}{\partial E}\right) dE$ - in the following forms:

$$\begin{aligned} \mathcal{G} &= dI/dV = \sum_{\nu} L_{\nu}^{(0)}/T \\ \mathcal{S} &= -\frac{k_B}{|e|T} \frac{\sum_{\nu} L_{\nu}^{(1)}}{\sum_{\nu} L_{\nu}^{(0)}} = \\ &= -\frac{k_B}{|e|T} \frac{\sum_{\alpha m \nu} \text{Im} \left\{ \frac{\tilde{\Gamma}_{\nu} a_m (\Lambda_{m\nu} + V_{\alpha})}{4\pi i} \Psi_1 \left[\frac{1}{2} + \frac{\Lambda_{\nu} - V_{\alpha}}{2\pi i T} \right] \right\}}{\sum_{\alpha m \nu} \text{Re} \left\{ \frac{\tilde{\Gamma}_{\nu} a_m}{4\pi} \Psi_1 \left[\frac{1}{2} + \frac{\Lambda_{m\nu} - V_{\alpha}}{2\pi i T} \right] \right\}} \end{aligned} \quad (41)$$

where for the normal channels: $a_m = 1$, $\Lambda_{m\nu} = \Lambda_{\nu}$ and the sums run only over the $\alpha\nu$. For $t = 0$ the system is in the symmetric SU(4) Kondo state, and the thermoelectric power is given by:

$$\mathcal{S} = -\frac{\pi^2}{3|e|} \frac{\sum_{\nu} \tilde{\chi}_{\nu\nu} (\sin[2\delta_{\nu}]/\tilde{\Gamma}_{\nu})}{\sum_{\nu} (\sin^2[\delta_{\nu}]/(\pi\tilde{\Gamma}_{\nu}))} T + 0[T^3] \quad (42)$$

If we measure \mathcal{S} below the Kondo temperature T_K , the Seebeck effect of the quasiparticles is determined by the linear part of the thermoelectric power and FL corrections give the same results as the sbMFA ($\gamma_{\mathcal{S}} \approx -\cos[\delta_{\nu}]$). Finally we can introduce the linear thermoelectric power coefficient in the form $\gamma_{\mathcal{S}} = (\mathcal{S}T_K)/(2\pi T)$. For the SU(4) Kondo state, the coefficient leads to $\gamma_{\mathcal{S}} = -(k_B/|e|)(\pi/3)(\tilde{E}_{\nu}/T_K) = -(k_B/|e|)(\pi/3) \cos[\delta_{\nu}]$. The quantity $\gamma_{\mathcal{S}}$ is given by the phase shift δ_{ν} and changes its sign at the electron-hole symmetry point [114]. The coefficient contains the information about the position and the width of the quasiparticle resonance and the SU(N) symmetry of the Kondo state. For the SU(4) Kondo effect, the linear TEP coefficient is related to the numbers $\mp\pi/(3\sqrt{2})$ in the $1e(3e)$ charge sector, and for the fully symmetric SU(3) Kondo state, $\gamma_{\mathcal{S}}$ reaches $\mp\pi/6$ [45]. Generally, TEP developed to the lowest order in terms of temperature is given by the Mott's formula $\mathcal{S} = -\frac{\pi^2}{3|e|} \frac{\sum_{\nu} d\tilde{q}_{\nu}/dE|_{E=0}}{\sum_{\nu} \tilde{q}_{\nu}} T$. In particular, for the fractional SU*(3) Kondo state in the whole range

of the coupling strength t , we obtain $\gamma_{\mathcal{S}}$ as follows:

$$\begin{aligned} \gamma_{\mathcal{S}} &= \\ &= \frac{-\pi T_K \left\{ 3\tilde{q}_{\nu}^{\dagger}(0) + \frac{\cot[\delta_{\nu'}][\tilde{\Gamma}_{\nu'}\delta^2 + \tilde{t}_{\nu'}^2(\delta - \tilde{\Gamma}_{\nu'})]}{\pi\tilde{\Gamma}_{\nu'}(2\tilde{t}_{\nu'}^2 + \tilde{\Gamma}_{\nu'}\delta \csc^2[\delta_{\nu'}])} \right\}}{3\tilde{q}_{\nu}(0) + \tilde{q}_{\nu'}(0)} \end{aligned} \quad (43)$$

where $\tilde{q}_{\nu}^{\dagger}(0) = -\tilde{\chi}_{\nu\nu\nu}^{[3]}/2 = \frac{\cos[\delta_{\nu}]\sin^3[\delta_{\nu}]}{\pi\tilde{\Gamma}_{\nu}^2}$ (see Eq.(22)). In the limit of the strong coupling strength to the Majorana fermion ($\tilde{t}_{\nu'} \mapsto \infty$), the linear TEP factor reaches $\gamma_{\mathcal{S}} = \mp \frac{\pi \sin[\delta_{\nu}]\sin[2\delta_{\nu}]}{-4+3\cos[2\delta_{\nu}]} = \mp 3\pi/22 \approx \mp 0.42.. < \mp\pi/6$ [45]. $\gamma_{\mathcal{S}}$ in the strong coupling limit leads to the number $\mp 3\pi/22$ and, in contrast to the SU(3) Kondo state, the value is modified by the coupling term to TSC. The result is different from the broken Kondo state e.g. by the magnetic field, because the topological channel with an increase of \tilde{t}_{ν} is active in \mathcal{S} . The results suggest that the symmetry of the Kondo effect is violated and is associated with the fractional SU*(3) Kondo state.

In our device we use the finite bias $V_{s(d)}$ and the temperature gradient δT to study the quantum conductance, shot noise and thermoelectric power. In all the results we can distinguish three sectors of the coupling strengths: $t_1 = \sqrt{\delta\Gamma}/6$, which shares the normal and crossover region in the transport, $t_2 = \Gamma U$ is the upper limit of the transport in the intermediate coupling strength, and $t_3 = U/2$ is the starting point of the strong coupling region, where the new Kondo phase is realized.

D. SU*(3) and SU*(2) Kondo states and the U*(1) charge symmetry phase in CNTQD-TSC devices

Figure 5a shows the density plot of the quantum conductance for the weak, intermediate and strong coupling regions in the CNTQD-TSC system. For $t \approx 0$ the unitary conductance can be expressed directly from the phase shift δ_{ν} of the Kondo quasiparticle resonance $\mathcal{G} = (e^2/h) \sum_{\nu} \sin^2[\delta_{\nu}]$.

In this limit, the full SU(4) Kondo effect is realized in the device. For $Q = 1e$ and $3e$, the total conductance reaches $\mathcal{G} = 2(e^2/h)$ (black lines in Figure 5c-d and blue area in Figure 5a). SU(4) Kondo effect emerges from the fourfold degeneracy of the states $|p_{ls}\rangle_4$ and $|t_{ls}\rangle_4$. In the case of $Q = 2e$ (two electrons on the quantum dot), the conductance is quantized to $4e^2/h$ for $t = 0$ (dark black area in Figure 5a). The half-filling region is determined by the six states $|d_{\nu}\rangle_6$. The SU(4) Kondo effect in the CNTQD was first observed by [26] and confirmed by the measurements of the other groups [5, 27]. In comparison with the results of the sbMFA method [40], the NRG calculation also showed the two-stage quantized conductance for the SU(4) Kondo state in CNTQD [42, 43].

As the coupling strength increases, the multiplet states are formed in the system. Below t_1 , as we can see in Figure 5b, in the intermediate coupling range there is a decrease in the conductance for the $Q = 2e$ region, the conductance reaches $(7/2)(e^2/h)$ (red line on

the landscape plot). The Kondo effect is determined by the duodecuplet states $|q_w\rangle_{12}$. The conductance in the channel coupled to the Majorana fermion is quantized to $\mathcal{G}_{+\uparrow} = (1/2)(e^2/h)$ (inset in Figure 5d), the remaining conductance value comes from the Kondo channels and reaches $3(e^2/h)$. With increasing the coupling to the TSC, the conductance at the e-h symmetry point ($E_d = E_{e-h} = -3U/2 = -4.5$) does not change, this is due to the number of twelve states $|q_w\rangle_{12}$ and $|q_y\rangle_6$, $|q_g\rangle_6$ involved in the quantum transport (red curve in Figure 5b and dark purple area in Figure 5a).

The quantum conductance for the low and high energy octuplets $|q_a\rangle_8$ and $|q_b\rangle_8$ in the weak coupling regime reaches $2(e^2/h)$, of which in the Majorana-coupled channel $\mathcal{G}_{+\uparrow} = (1/2)(e^2/h)$, and the other three normal channels contribute to $\mathcal{G} = \mathcal{G}_{+\downarrow} + \sum_s \mathcal{G}_{-s} = (3/2)(e^2/h)$. In the strong coupling regime above t_2 , especially near t_3 , the conductance for $E_d = -1.5$ (respectively $E_d = -7.5$) reaches $(3/2)(e^2/h)$ (green line in Figure 5b). As can be seen from the partial contributions of the total conductance (Figure 5d), the conductance in the Majorana channel remains unchanged $\mathcal{G}_{+\uparrow} = (1/2)(e^2/h)$ but in the other channels it reaches $\mathcal{G}_{+\downarrow(-s)} = (1/3)(e^2/h)$, due to the charge degeneracy between the d and p states. For $E_d = 1$, above the t_1 (cyan line in Figure 5b), the conductance reaches a constant value of $\mathcal{G}_{+\uparrow} = 1/2(e^2/h)$ and originates only from the Majorana fermion-coupled channel (a value previously confirmed by calculations within NRG [110–113], EOM and sbMFA method [128]). The half-quantum conductance originates from the ground state of the doublet $|q_x\rangle_2$ and $|q_z\rangle_2$. The transition to the strong coupling strength regime depends on the ratio of U/Γ . $t_1 = \sqrt{\delta\Gamma}/6$ separates the normal and the entangled qubit states by TSC. The quantum measurements above $t_3 = U/2$ show only well-defined quantum states in the strong coupling regime. t_1 and t_2 , shown as vertical dashed gray lines in Figure 5b, can be shifted by reducing the coupling to the normal electrodes $\tilde{\Gamma}$.

The most significant result predicted by the theory is the transition with increasing the coupling strength t from the charge degeneracy line between $Q = 1e, 2e$ and $Q = 2e, 3e$ to the $SU^*(3)$ Kondo state in the fractional charge region. The symmetry type of the Kondo effect is upper indexed by \star due to the fact that the Kondo state appears in three channels with quantized conductance $\mathcal{G}_{+\downarrow(-s)} = (3/4)(e^2/h)$ for the half-occupancy region $Q = 3/2e$ and $Q = 5/2e$ (green lines in Figs. 5c, d). This is a surprising result in contrast to the fully $SU(3)$ Kondo effect [46], where it occurs for integer charges $Q = 1e$ and $2e$. This is mainly due to the degeneracy of the six quantum states, the low and high energy sextuplets $|q_g\rangle_6$ and $|q_y\rangle_6$ (Eq.(10)). The Kondo state does not follow from the degeneracy of the three pure quantum states $|p_{ls}\rangle_3$ or $|d_{ls}\rangle_3$ [45], but from the degeneracy of the six entangled states $|q_y\rangle_6$ for $Q = (5/2)e$ and six high energy quantum states $|q_g\rangle_6$ for $Q = (3/2)e$. In the quantum conductance map, we observe the light violet sector of the $SU^*(3)$ Kondo effect, where the to-

tal conductance reaches $\mathcal{G} = (\mathcal{G}_{+\downarrow} + \sum_s \mathcal{G}_{-s}) + \mathcal{G}_{+\uparrow} = (9/4)(e^2/h) + (1/2)(e^2/h) = (11/4)(e^2/h)$ (blue line in Fig. 5b). The conductance in the channel coupled to the Majorana fermion is independent of the coupling strengths t and E_d . The contribution of $\mathcal{G}_{\nu'}$ to the total conductance is $(1/2)(e^2/h)$.

Figure 6 shows the quantum conductance for the CNTQD-2TSC system. The quantum dot is coupled to two Majorana fermions $\gamma_{+\uparrow}$ and $\gamma_{-\uparrow}$ (Fig. 1). Two half-fermions can also be prepared, e.g. in DIII class superconductors, where the quantum state with two Majoranas can be realized as a Majorana Kramers pairs at the edge of a single topological superconducting wire [87, 103, 104]. The conductance of the CNTQD-2TSC device reaches $\mathcal{G} = \sum_l \mathcal{G}_{l\uparrow} + \sum_l \mathcal{G}_{l\downarrow} = (e^2/h) + 2(e^2/h) = 3(e^2/h)$ for $E_d = -4.5$ and $t > t_1$. For the subsequent growth of the coupling strength, \mathcal{G} is unchanged (red curve in Fig. 6b, light violet region in Fig. 6a). Around t_1 we observe a transition in the state configuration from $|d_\nu\rangle_6$ to $|q_w\rangle_{24}$. In the weak coupling regime, the quantum state of the system is determined by twenty-four states $|q_w\rangle$ in $2^{4+2} = 64$ dimensional Hilbert space. The $SU^*(2)$ Kondo state is mainly realized for $t > t_2$ and includes the eight entanglement quantum states. The ground state is the octuplet $|q_y\rangle_8$ (Eq. (12)). The channels coupled to the Majorana states contribute (e^2/h) to the quantum conductance, the other two channels are related to the Kondo effect. It is difficult to determine the moment of the transition between strongly and weakly coupled systems with TSCs - based only on the quantum conductance. However, the quantum transition will be detectable in the nonlinear shot noise and the current measurements, in the temperature dependent effective pseudospin or in the entropy detection [138], which we will discuss later. In the $Q = 1e$ and $3e$ charge region, the total conductance is quantized to $\mathcal{G} = 2(e^2/h)$ for the intermediate coupling strength. The conductance in the channels associated with the Kondo states contributes $\mathcal{G}_{\pm\downarrow} = (1/2)(e^2/h)$ and is determined by the degeneracy of the sixteen quantum states $|q_b\rangle_{16}$ and $|q_a\rangle_{16}$. Beyond the Kondo solutions for weak and strong coupling with TSCs, the total conductance reaches e^2/h , for two quartets $|q_x\rangle_4$ and $|q_z\rangle_4$ as the ground states. For the strong coupling to the Majorana fermion, the conductance for $Q = 1, 3e$ in the channels associated with the Kondo state is suppressed to e^2/h , because the next two quantum channels are operated by Majorana fermions (green lines in Figures 6c,d).

Figure 7 shows the quantum conductance as a function of E_d and the effect of breaking the $SU(4)$ Kondo state by increasing the coupling strength to three Majorana fermion in the CNTQD-3TSC device. For $Q = 0e$ and $Q = 4e$ with increasing the coupling strength we observe a transition from empty and fully occupied states to high and low energy octuplets: $|q_z\rangle_8$ and $|q_x\rangle_8$. The conductance reaches $\mathcal{G} = \sum_s \mathcal{G}_{+s} + \mathcal{G}_{-\uparrow} = (3/2)(e^2/h)$, when the transport goes through the channels coupled to three Majorana fermions (red region in Figure 7a). The

number of available states in the system is $2^{4+3} = 128$, and all quantum states are spanned by the basis vectors $|n_+n_-n_1n_2n_3\rangle$. The total charge on the quantum dot is $Q = 5/2e$ and $Q = 3/2e$ for two octuplets $|q_x\rangle_8$ and $|q_z\rangle_8$, defined in Eqs. (13-14). Each of these states is a linear combination of eight pure quantum states mutually mixed with a topological segment. The transitions from $|p_{ls}\rangle_4$ via $|q_a\rangle_{32}$ to $|q_z\rangle_8$ and from $|t_{ls}\rangle_4$ via $|q_b\rangle_{32}$ to $|q_x\rangle_8$ are observed as an increase mechanism from integer charges $Q = 1e$ and $Q = 3e$ to the fractional charges $Q = (3/2)e$ and $Q = (5/2)e$.

The conductance for $E_d = -1.5$ (green line in Fig. 7b) changes the quantized value from $2(e^2/h)$ to $(3/2)(e^2/h)$ (contributed by the channels in the conjunction with the MFs). For $E_d = -4.5$ we observe a transition from $|d_\nu\rangle_6$ to the entangled quantum states with the highest degeneracy in the hybrid system $|q_w\rangle_{48}$. In this case the conductance decreases from $4(e^2/h)$ to $(5/2)(e^2/h)$ (red curve in Fig. 7b). In the normal channel $\mathcal{G}_{-\downarrow} = 1(e^2/h)$, the remaining contribution from the channels coupled to the TSC is quantized to $(3/2)(e^2/h)$ and dominates in the quantum transport measurements. In the strong coupling regime for $t > t_3$ at the e-h symmetry point, the conductance is fixed and quantized to $5/2(e^2/h)$. Two quantum octuplets $|q_x\rangle_8$ and $|q_z\rangle_8$ degenerate on this line. The system at this point is determined by the charge degrees of freedom and we observe a $U^*(1)$ charge symmetry solution. $U(1)$ symmetry is observed in the normal state between the charge regions for the fractional charge on the quantum dot. $U^*(1)$ symmetry appears for $Q = 2e$. The analogous result was found for $Q = 1e$ in the QD coupled to 1TSC [112], since in this system we have only two channels $s = \uparrow, \downarrow$, where $s = \uparrow$ is coupled to the single Majorana fermion, consequently the total conductance at this point reaches a value of $(3/2)(e^2/h)$ [141]. It is worth noting that saturation occurs at the e-h symmetry point, so applying an external magnetic field or polarization would allow this point to be moved along the E_d axis (see the effect of the exchange field on the Kondo state [142]). The analogy can be found in the charge Kondo effect with the polarons, where the Kondo temperature for the charge Kondo state decreases with increasing coupling strength to the phonon bath [143]. For the CNTQD-3TSC device, the characteristic energy scale $T_{[*]}$ is saturated (light red curve in Fig. 9a). Comparing the results from Figures 5-7b, we observe the effect of squeezing the conductance around the value $2\sin^2[\pi/2] = 2(e^2/h)$. From this we can conclude that for the Kondo effect with even $SU(N)$ symmetry, the squeezed conductance will be seen around the value $(N/2)(e^2/h)$ when all quantum states in the quantum dot are coupled to TSC segments.

Let us introduce the magnitude of the spin and orbital polarization in terms of $\Delta\mathcal{G}_s = \sum_i(\mathcal{G}_{i\uparrow} - \mathcal{G}_{i\downarrow})/\mathcal{G}$ and $\Delta\mathcal{G}_o = \sum_s(\mathcal{G}_{+s} - \mathcal{G}_{-s})/\mathcal{G}$. TSC strongly polarizes the conduction channels. In two cases, namely coupling with 1TSC and 3TSC, the orbital and spin polarization are equal $\Delta\mathcal{G}_s = \Delta\mathcal{G}_o$. In Figure 8a we see a negatively polar-

ized conduction for $Q = 2e$ and for twelfold degenerate quantum states $|q_w\rangle_{12}$. The value of the spin (orbital) polarization for $|q_w\rangle_{12}$ reaches $-1/7$ and saturates for $t > t_1$ (red lines in Figure 8d and lower inset in Figure 8d). In the case where the sextuplets $|q_{g(y)}\rangle_6$ are the ground states of the fractional $SU^*(3)$ Kondo effect, the spin polarization of the conductance is negative and corresponds to the rational number $-1/11$. For $Q = 1(3)e$ and $t < t_2$ the polarizations are equal to zero. For $t > t_2$, $\Delta\mathcal{G}_s$ is positive and reached $+1/9$ for the CNTQD-1TSC device and $+1/3$ for the CNTQD-3TSC (green lines in Fig. 8d). The highest spin(orbital) polarization in the hybrid systems is dominated by the conductance contribution of the Majorana channels and occurs for doublet $|q_{x(z)}\rangle_2$ and quartet $|q_{x(z)}\rangle_4$ states. The spin and orbital polarizations reach a value of $+1$ for these ground states. For the Majorana-Kondo state, the polarizations are always negative, in contrast to cases where the channels coupled to the Majorana fermions dominate, where they are positive. The reversal of the polarization sign is observed for $E_d = -3$, where the value of $\Delta\mathcal{G}_s$ changes from negative to positive enhancement for the CNTQD-3TSC device and is suppressed for the CNTQD-2TSC system (blue lines in the insets in Fig. 8d). For the CNTQD-2TSC device, due to the type of the coupling strength ($\tilde{t}_{\pm\uparrow}$), the orbital polarization is equal to zero, and we only observed the spin polarization of the conductances in the system (Fig. 8b). The spin and orbital polarization of the conductance for the CNTQD-3TSC system reaches a positive rational number $+1/3$ when the transport is determined by the two octuplets $|q_x\rangle_8$ and $|q_z\rangle_8$ (light blue region in Fig. 8c). For $|q_w\rangle_{48}$ the spin(orbital) polarization of the conductance of CNTQD with side-attached three Majorana fermions is saturated at the negative quantized value $-1/5$ (red curve in the lower inset in Fig. 8d and dark blue region in Fig. 8c).

The transport in the channel coupled to the Majorana fermion is determined by the anomalous Green's function, which significantly modifies the Kondo temperature T_K in the system (Eq. (6)). Looking at the quantum conductance in terms of linear transport, we can see that the channels associated with the Kondo state are described by Eq. (35), while in the case of a channel coupled to the TSC we have found the relation in Eq. (36). Both formulas are determined by the characteristic temperature $T_{K,\nu}^2 = \tilde{E}_\nu^2 + \tilde{\Gamma}_\nu^2$ and for the channel coupled to MFs, $T_{K,\nu'}^2 = \tilde{E}_\nu^2 + \tilde{\Gamma}_\nu^2 + (2\tilde{t}_{\nu'}^2\tilde{\Gamma}_{\nu'})/\delta$. Within the sb-MFA formalism, \tilde{E}_ν^2 and $\tilde{\Gamma}_\nu^2$ determine the position and width of the quasiparticle Kondo resonance. In an elegant way, following Coleman [130], we can relate the complex pole of the quasiparticle Green function with T_K and the charge Q_ν in the following form $\ln[\tilde{E}_\nu - i\tilde{\Gamma}_\nu] = \ln[T_K] - i\pi Q_\nu$, where in the context of FL theory, Q_ν is given by the phase shift δ_ν (Eq. (20)). If we write the expression as $e^{i\pi Q_\nu} = T_K/\Lambda_\nu^*$, we get the Euler's formula, which materializes in the physics. This is why we talk about the logarithmic scaling of the Kondo

effect at low temperatures. In my opinion, the wide range of mathematical functions (in particular the hypergeometric functions [144]) opens up to experimental physics a multiversum of a new type of correlated states, not yet discovered. In summary, if we find a functional relation (correlation) between the charge (spin etc.) and the pole of the Green's function of a new quantum state - then we have a simple recipe to open the door to a new world of correlated systems of spin(electron) and other particles. Perhaps AI, with its uncompromising approach to finding solutions, will be a great tool in this research, the future will tell us.

Figure 9a shows the characteristic temperatures, defined as $T_{[\star]} = \min\{T_{K,\nu}, T_{K,\nu'}\}$. In the decoupled CNTQD with TSC ($t = 0$), the system is determined by the SU(4) Kondo temperature $T_K^{SU(4)}$. For $E_d = -4.5$ the Kondo resonance is centered on the Fermi level due to the phase shift $\delta_\nu = \pi/2$, and the sixfold degenerate quantum states $|d_\nu\rangle_6$ determines the Kondo temperature (red lines in Fig. 9a). However, the number of six states for $2e$ is higher than the fourfold degeneracy for $Q = 1(3)e$, $T_{K,Q=1e(3)}^{SU(4)} > T_{K,Q=2e}^{SU(4)}$, as is well documented in the literature [42, 43, 145]. From the extended K-R sbMFA we obtained the relation $T_{K,2e}^{SU(4)}/T_{K,1e(3)}^{SU(4)} \equiv e^{\frac{-\pi U}{4\Gamma\Lambda}}$, where $\Lambda = 60$ and follows from the derivatives of the renormalization of the tunneling rates with respect to the boson fields operators for two charge regions $Q = 1(2)e$. The characteristic temperature $T_{[\star]}$ in the weak coupling limit at the charge degeneracy line for $Q = (3/2)e$ and $E_d = -3$ (similarly for $Q = (5/2)e$) is proportional to the hybridization parameter Γ , which determines the width of the charge resonances (all blue lines in Fig. 9a). For $E_d = -1.5$, increasing the coupling strength to the TSC leads to an increase in the characteristic temperature (the temperature in the Majorana channel determines the saturation of $T_{[\star]}$, green curves in Fig. 9a). We have shown that rise of the number of N_{TS} topological segments in the strong coupling regime leads to the enhancement and saturation of $T_{[\star]}$ for $E_d = -1.5$ (dark, dotted and light green lines represent the results for CNTQD-1TSC, CNTQD-2TSC and CNTQD-3TSC). Similar effects are observed for $E_d = -3$ and $E_d = -4.5$, in the case where the transport determines the channel directly coupled to the Majorana fermions.

A fractional Kondo effect with SU*(3) symmetry is observed in the CNTQD-1TSC system for $Q = (3/2)e$ and $Q = (5/2)e$. The transport is mainly determined by the channels associated with the Kondo effect ($\mathcal{G}_\nu = (9/4)(e^2/h)$), which is manifested by a decrease in the characteristic temperature $T_{[\star]}$ (dark blue line for $E_d = -3$ in Fig. 9a). For $E_d = -4.5$, in the CNTQD coupled with two Majorana fermions, $T_{[\star]}$ decreases with increasing the coupling strength to the topological wire, and we observe a strong decrease of $T_K^{SU^*(2)}$. By increasing t for the CNTQD-2TSC device, we start from the SU(4) Kondo effect and end up in the SU*(2) Kondo state with the reduced characteristic temperature scale

$T_K^{SU^*(2)}$. Between these two types of strongly correlated states we observed a strong enhancement of $T_{[\star]}$, which is characteristic of crossover [40]. The similar effects of the Kondo temperature boost, have been observed with an increase of the spin-orbital interaction (SOI) in the CNTQD system, as indicated by sbMFA [40] and the NRG method [43]. Based on the NRG framework it is difficult to explain the increase of T_K , in the sb-MFA method we can relate it to the trends in the bosonic fields, more precisely to the products of operators in the renormalization parameter of the quasiparticle resonance z_{ls} . An increase of the Coulomb interaction U in CNTQD increases the values of these products and finally we observe the enhancement of T_K in the crossover region [40]. We expect the same effects for the CNTQD-2TSC device with an increase of the coupling strength t .

Furthermore, the fact that the characteristic temperature increases with t determines the behavior of the quantum conductance at finite temperature T . Fig.9b shows the density plot of the quantum conductance for CNTQD coupled to a single Majorana fermion at finite temperature $T = 10^{-2}$. The SU(4) and SU*(3) Kondo states are destroyed by the temperature effects, leading to a suppression of the quantum conductance in the unitary Kondo regions ($\mathcal{G} \mapsto 0$ for $|q_{a(b)}\rangle_8$, $|q_w\rangle_{12}$ and $\mathcal{G} \mapsto \mathcal{G}_{\nu'} = (1/2)(e^2/h)$ for $|q_{g(y)}\rangle_6$). The transport takes place along the line of charge degeneracy, e.g. between the quantum states $|q_{a(b)}\rangle_8$ and $|q_w\rangle_{12}$ and between $|q_g\rangle_8$ and $|q_g\rangle_8$ we observe a value of finite quantum conductance at a level of $(5/2)(e^2/h)$. Between $|q_{a(b)}\rangle_8$ and $|q_{x(z)}\rangle_2$ the conductance reaches a value of $(3/2)(e^2/h)$. Since $T_{[\star]}$ is higher than T for the $|q_{x(z)}\rangle_2$ states, the Majorana fermion channel remains active in the quantum transport. The doublet states $|q_{x(z)}\rangle_2$ in the weak coupling regime are collapsed, and the transport is determined by two singlets $|e\rangle_1$ and by the fully occupied quantum state $|f\rangle_1$. Figure 9c shows the evolution of the conductance as a function of t for different temperatures T . It can be seen that the transition from $|d_\nu\rangle_6$ to $|q_w\rangle_{12}$ is shifted at low temperatures (red line in Fig. 9c). For $T = 10^{-4}$ the quantum conductance decreases to $2(e^2/h)$ and gradually approaches zero. In the strong coupling regime the quantum conductance reaches $\mathcal{G} = (7/2)(e^2/h)$, and after passing $T = 10^{-3}$, \mathcal{G} is quantized to $(5/2)(e^2/h)$ (black line in Fig. 9c). The inset shows the evolution of the quantum conductance with increasing temperature for $E_d = -3$. For $T > T_K^{SU^*(3)}$, the fractional SU*(3) Kondo state is destroyed and the quantum conductance reduces to $(1/2)(e^2/h)$. The inset of Fig. 9c shows the gradual decrease of the quantum conductance for $Q = (3/2)e$ and shift to the characteristic coupling strength t_3 . In the weak coupling regime, \mathcal{G} leads to $(5/2)(e^2/h)$ for the charge degeneracy line (black curve in the inset of Fig.9c).

In this section, we will now turn to discussing the charge fluctuations that occur in the CNTQD-TSC device. The total occupancy number of CNTQD is given by $N = \sum_\nu Q_\nu + \sum_{\nu'} Q_{\nu'}$. The quadratic charge fluctuation

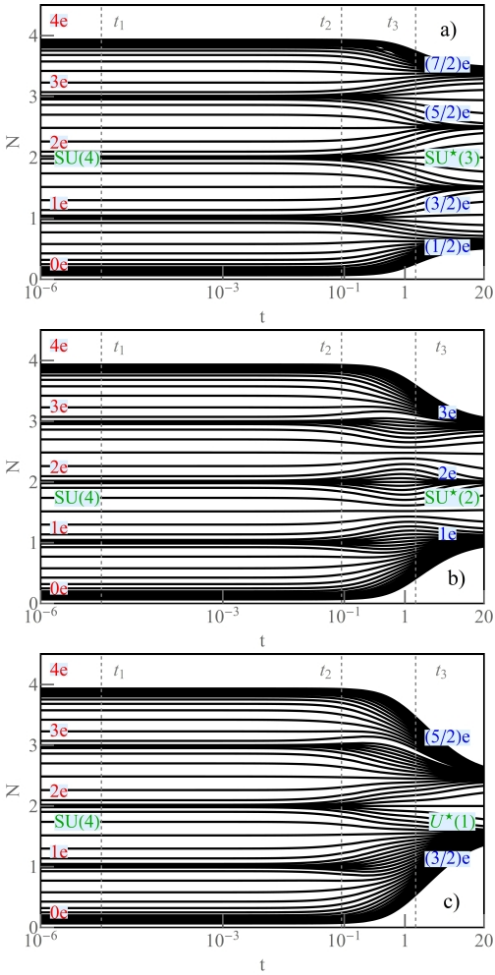


FIG. 11. (Color online) Total occupancy number N for CNTQD coupled to 1MF (a), 2MFs (b) and 3MFs (c). The numbers indicate the integer and fractional electron charge in the system. $SU(4)$, $SU^*(3)$, $SU^*(2)$ and $U^*(1)$ symbolize the spin-orbital, fractional, integer Kondo states and the charge degeneracy line.

tuation is evaluated by the difference of the expectation value of $\langle N^2 \rangle$ and $\langle N \rangle^2$ in the following form: $\Delta N^2 = \langle N^2 \rangle - \langle N \rangle^2$. The magnitude ΔN^2 can be expressed in terms of the boson fields: $\Delta N^2 = \sum_{l_s} p_{l_s}^2 + 4 \sum_{\nu} d_{\nu}^2 + 9 \sum_{l_s} \bar{t}_{l_s}^2 + 16 f^2 - (\sum_{l_s} p_{l_s}^2 + 2 \sum_{\nu} d_{\nu}^2 + 3 \sum_{l_s} \bar{t}_{l_s}^2 + 4 f^2)^2$. In Figures 10a and 10b we can see that for the $SU(4)$ Kondo state, in the regime of weak and intermediate coupling strengths determined by $|p_{l_s}\rangle_4$, $|t_{l_s}\rangle_4$ and $|d_{\nu}\rangle_6$ ($|q_{a(b)}\rangle_8$ and $|q_w\rangle_{12}$) quantum states, the charge fluctuation ΔN^2 is strongly suppressed, comparable to $T_{[\ast]}$ (more precisely to T_K) [45]. By increasing the coupling t to the TSC for $Q = (3/2)(e^2/h)$, the charge fluctuation remains at the level $\Delta N^2 = 1/4$, which is the significant result for the fractional $SU^*(3)$ Kondo state (dark blue areas in Fig. 10a and blue curve in Fig. 10b). At the charge boundary for $Q = 1e$ and $Q = 2e$, the charge fluctuation reaches $1/2$. The main contribution to the large finite value of ΔN^2 comes from the Majorana

fermion-coupled channel. N^2 is determined by the expected values of the boson fields operators. For the $SU^*(3)$ Kondo state, ΔN^2 reaches $1/4$ and the value is associated with $p_{+\downarrow(-s)}^2 = d_{20,\uparrow\uparrow,\uparrow\downarrow}^2 = 1/6$ for $Q = (3/2)e$ and $\bar{t}_{+\uparrow(-s)}^2 = d_{02,\downarrow\downarrow,\downarrow\uparrow}^2 = 1/6$ for $Q = (5/2)e$. In contrast to the region where the MF-coupled channel dominates in the quantum transport, $\Delta N^2 = 1/4$ but is determined by the amplitudes $e^2 = p_{+\uparrow}^2 = 1/2$ for the quantum states $|q_z\rangle_2$ and $f^2 = p_{+\downarrow}^2 = 1/2$ for $|q_x\rangle_2$.

Fig. 11 shows the evolution of the occupancy number $N = \sum_{\nu} Q_{\nu}$ with the increase of the coupling strength to 1TSC, 2TSC and 3TSC. The black lines on the landscape plots represent the total occupancy number N with an increment $\delta E_d = +0.15$ for E_d in the range -12 to $+3$. We observed a significant change in the value of the total charge for $t > t_2$. The strong influence of the anomalous Green's function $\hat{G}_{12}^R = \langle \langle f_{\nu'}^{\dagger}; f_{\nu'}^{\dagger} \rangle \rangle^R$ on the statistical value of the total charge N is manifested by an increase in the value of the correlator $i\tilde{t}_{\nu'} \langle \gamma_{\nu'} f_{\nu'}^{\dagger} \rangle^<$. In the total charge number Q we observe the leakage of the charge by finite value of the tunnel correlator and additional degrees of freedom of the Majorana fermion. Formally, by decomposing the tunneling term into two parts (see Sec. IIIA), we can say that the local isospin $\langle f_{\nu'}^{\dagger}, f_{\nu'}^{\dagger} \rangle$ in the system increases and at the same time the value of the charge is modified by tunneling processes. In the CNTQD-TSC device we observe characteristic fractional charges $Q = (1/2)e$ and $Q = (7/2)e$ when the system is determined by two doublets $|q_x\rangle_2$ and $|q_z\rangle_2$. In terms of the fractional $SU^*(3)$ Kondo state, the charge values are quantized to $3/2e$ and $5/2e$, where two sextuplets $|q_g\rangle_6$ and $|q_y\rangle_6$ are the ground states. In the CNTQD-2TSC system the $SU^*(2)$ effect is realized in the strong coupling regime. For the Kondo state, the quantum conductance reaches $3(e^2/h)$ and the total charge is $N = Q = 2e$ (Fig. 11b), where the octuplet quantum states $|q_y\rangle_8$ are the ground state. In the channel coupled to the Majorana fermion, the occupancy number reaches $Q = 1e$ and $3e$ for the quantum states $|q_z\rangle_2$ and $|q_x\rangle_2$. The coupling strength to the three Majoranas with chirality $l_s = +s$ and $l_s = -\uparrow$ leads with increasing t to the degeneracy line of the two octuplets $|q_x\rangle_8$ and $|q_z\rangle_8$. The transport here occurs through three Majorana fermion-coupled channels and one normal channel between the charges $Q = 5/2e$ and $Q = 3/2e$, i.e. exactly for $Q = 2e$ (Fig. 11c). The CNTQD-3TSC system is determined by the $U^*(1)$ charge symmetry state.

Figure 12 presents the absolute values of the X- and Z-components of the spin and isospin as a function of the atomic level of the quantum dot (E_d). The spin components can be written as $\hat{S}_X = (1/2) \sum_l (d_{l\downarrow}^{\dagger} d_{l\uparrow} + d_{l\uparrow}^{\dagger} d_{l\downarrow})$ and $\hat{S}_Z = (1/2) \sum_l (n_{l\uparrow} - n_{l\downarrow})$ and the isospin components can be expressed by $\hat{I}_X = (1/2) \sum_l (d_{l\downarrow} d_{l\uparrow} + d_{l\uparrow}^{\dagger} d_{l\downarrow}^{\dagger})$ and $\hat{I}_Z = (1/2) \sum_{l_s} n_{l_s} - 1$. The operators of the local X- and Z-spin components are defined by the boson fields

operators in the following terms:

$$\begin{aligned}
\hat{S}_X &= (1/2) \left(\sum_{ls} p_{ls}^\dagger p_{l\bar{s}} + \sum_s d_{s\bar{s}}^\dagger (d_{ss} + d_{\bar{s}\bar{s}}) \right. \\
&+ \sum_s d_{ss}^\dagger (d_{s\bar{s}} + d_{\bar{s}s}) + \sum_{ls} \bar{t}_{ls}^\dagger \bar{t}_{l\bar{s}} \left. \right) \\
\hat{S}_Z &= (1/2) \left(\sum_l (p_{l\uparrow}^\dagger p_{l\uparrow} - p_{l\downarrow}^\dagger p_{l\downarrow}) \right. \\
&+ 2d_{\uparrow\uparrow}^\dagger d_{\uparrow\uparrow} - 2d_{\downarrow\downarrow}^\dagger d_{\downarrow\downarrow} + \sum_l (\pm \bar{t}_{l\uparrow}^\dagger \bar{t}_{l\uparrow} \mp \bar{t}_{l\downarrow}^\dagger \bar{t}_{l\downarrow}) \left. \right) \quad (44)
\end{aligned}$$

The Majorana fermion leads to the local pairing-induced on CNTQD and modifies the X- and Z-isospin components in quantum dot. \hat{I}_X and \hat{I}_Z can be written in the bilinear form of the slave boson operators in the following

way:

$$\begin{aligned}
\hat{I}_X &= (1/2) \left(-p_{-\downarrow}^\dagger p_{-\uparrow} + \sum_s (p_{+s}^\dagger \bar{t}_{+s} + p_{-s}^\dagger \bar{t}_{-s}) \right. \\
&+ d_{20}^\dagger (-e + f) + e^\dagger (d_{20} + d_{02}) + d_{02}^\dagger f - f^\dagger d_{02} \\
&- d_{\downarrow\downarrow}^\dagger d_{\downarrow\downarrow} - d_{\uparrow\downarrow}^\dagger d_{\uparrow\downarrow} - \bar{t}_{-\uparrow}^\dagger \bar{t}_{-\downarrow} - \sum_s \bar{t}_{-s}^\dagger p_{-s} \left. \right) \\
\hat{I}_Z &= (1/2) \left(\sum_{ls} p_{ls}^\dagger p_{ls} + 2 \sum_\nu d_\nu^\dagger d_\nu \right. \\
&+ 3 \sum_{ls} \bar{t}_{ls}^\dagger \bar{t}_{ls} + 4f^\dagger f \left. \right) - 1 \quad (45)
\end{aligned}$$

The dashed and solid lines in Fig. 12 represent the spin and isospin components for the intermediate coupling to the topological superconductor ($t = 10^{-3}$) and for the strong coupling strength to a Majorana fermions (solid lines, $t = 20$). The spin X-component in Fig. 12a leads to $1/2$ and $1/\sqrt{2}$ for the quantum states $|q_{b(a)}\rangle_8$ and $|q_w\rangle_{12}$, where in the $SU^*(3)$ Kondo state $|S_X| = 1/3$ for $|g_y\rangle_6$ and at the e-h symmetry point the expectation value of the transverse spin leads to $|S_X| = 1/2$. The spin Z-component reaches ≈ 0 for $t = 10^{-3}$, in the strong coupling region $|S_Z| = 1/12$ for $|g_y\rangle_6$ and $|S_Z| = 1/4$ for $|g_{x(z)}\rangle_2$ (solid magenta line in Fig. 12a). The isospin $|I_Z|$ for $t = 10^{-3}$ (dashed blue line) is quantized to $1/2$ for the octuplets $|q_{b(a)}\rangle_8$ and $|I_Z| = 0$ for the duodecuplet state $|q_w\rangle_{12}$. The Z-component of the isospin for $t = 20$ (solid blue line) reaches the value $|I_Z| = 1/4$ for sextuplets $|q_{g(y)}\rangle_6$ and $|I_Z| = 3/4$ for the doublet quantum states $|q_{x(z)}\rangle_2$. The transverse component of the isospin is also modified, under the weak coupling strength to TSC: $|I_X|$ approaches $1/8$ for octuplets and $|I_X| = 1/6$ for duodecuplets. For the $SU^*(3)$ Kondo state, the transverse isospin component leads to a quantized value of $|I_X| = 1/6$ for the fractional charges on the quantum dot $Q = (3/2)e$ and $Q = (5/2)e$ (orange solid line in Fig. 12a).

Figure 12b shows the values of $|S_{X(Z)}|$ and $|I_{X(Z)}|$ for the CNTQD-2TSCs system. We can see that, in terms of coupling strengths for the octuplet states $|q_y\rangle_8$ and the $SU^*(2)$ Kondo effect: $|S_Z| = |I_Z| = 0$, and for the quartets $|q_{x(z)}\rangle_4$, $|S_Z| = |I_Z| = 1/2$. The X-components for $|q_{x(z)}\rangle_4$ reach the values $|S_X| = 1/12$ and $|I_X| = 0$. Figure 12c presents the expected values of the local spin and isospin for the CNTQD coupled to the three Majorana fermions $\{\gamma_{+s}, \gamma_{-\uparrow}\}$. The Z-components of the spin and isospin vanish $|S_Z| = |I_Z| = 0$ in the e-h symmetry point at the boundary of the octuplets $|q_{x(z)}\rangle_8$. At this point, the charge state $U^*(1)$ is realized and the local transverse spin leads to $|S_X| = 1/2$. For the quantum states $|q_{x(z)}\rangle_8$, when $Q = (5/2)e$ and $Q = (3/2)e$, the spin and isospin components reach $|S_X| = 1/3$, $|S_Z| = 1/4$ and $|I_X| = 0$, $|I_Z| = 1/3$.

Since the Majorana mode is assumed to be coupled to the spin-orbital energy level of the CNTQD with four-fold degeneracy, it breaks the spin and orbital symmetry of the system and is manifested in the temperature dependence of the entropy. Figure 13a shows the total

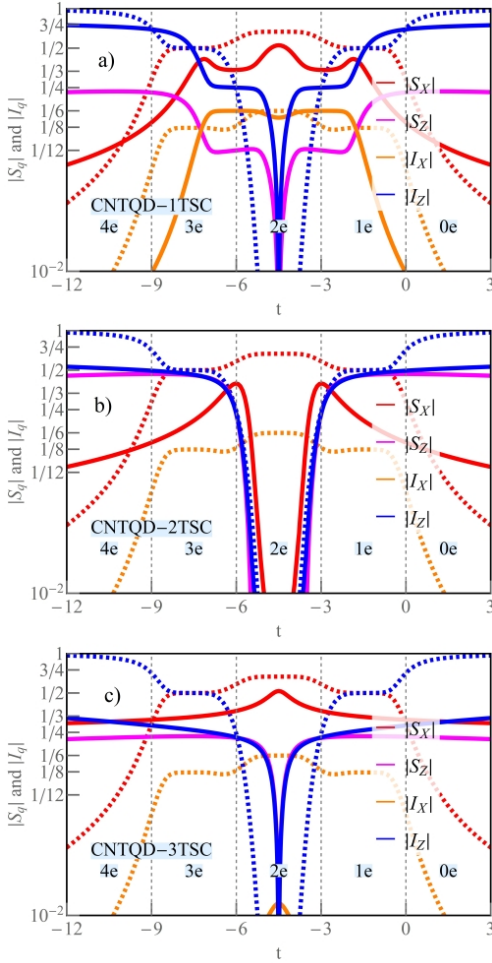


FIG. 12. (Color online) The absolute value of the spin $S_{q=X,Z}$ and the isospin $I_{q=X,Z}$ components plotted for $t = 10^{-3}$ (dashed lines) and $t = 20$ (solid lines) in: a) CNTQD-1TSC, b) CNTQD-2TSC and c) CNTQD-3TSC devices.

entropy S_{tot} for the CNTQD-1TSC system as the sum of the quantum dot entropy S_{QD} , the tunneling entropy S_T and the entropy of the topological superconductor S_{TS} . We can express these quantities following the author [146] in the form $S_{tot} = -\frac{\partial \tilde{F}_f}{\partial T}$, using the thermodynamic potential \tilde{F}_f and Matsubara Green's functions [17, 130]:

$$S_{tot} = S_{QD} + S_T + S_{TS}$$

$$S_{QD} = -\sum_{\alpha\nu} \text{Im} \left\{ i \log \Gamma \left[\frac{1}{2} + \frac{z \pm V_\alpha}{2\pi iT} \right] + \frac{(z \pm V_\alpha) \Psi_0 \left[\frac{1}{2} + \frac{z \pm V_\alpha}{2\pi iT} \right]}{2\pi T} \right\} \Big|_{z=\Lambda_\nu}^{z=\Lambda_\nu - W} \quad (46)$$

$$S_T = \sum_{\alpha\nu'} \int_{-\infty}^{+\infty} \text{Re} \left\{ \frac{(E \pm V_\alpha) \ln[\delta G_{\nu'}]}{16\pi iT^2 \cosh^2 \left[\frac{E \pm V_\alpha}{2T} \right]} \right\} dE$$

$$S_{TS} = -\sum_{\alpha\nu'} \text{Im} \left\{ i \log \Gamma \left[\frac{1}{2} + \frac{z \pm V_\alpha}{2\pi iT} \right] + \frac{(z \pm V_\alpha) \Psi_0 \left[\frac{1}{2} + \frac{z \pm V_\alpha}{2\pi iT} \right]}{2\pi T} \right\} \Big|_{z=iT_1}^{z=iT_1 - 2T_2} \quad (47)$$

where $\log \Gamma[z]$ is the logarithm of the Euler gamma function, $T_1 = \delta$ and T_2 are the characteristic temperatures in the entropy of the isolated TSC (T_2 is a characteristic temperature found in the tunneling entropy S_T and is related to the vanishing of the first derivative of $\delta G_{\nu'}$). $\delta G_{\nu'}$ in the tunneling entropy is given by [146]:

$$\delta G_{\nu'} = \frac{\sum_{k=1,2} \pm \hat{G}_{1k}^A(-E) \hat{G}_{k1}^R(E)}{\sum_{k=1,2} \pm \hat{G}_{1k}^R(-E) \hat{G}_{k1}^A(E)}. \quad (48)$$

where $\hat{G}_{ik}^{R(A)}(-E)$ are the Green's function of the matrix in Eq. (6). In the evolution of S_T as a function of T , we observed the third characteristic temperature $T_3 = \tilde{t}_\nu^2/2|\tilde{E}_{\nu'}|$, where S_T goes to zero.

Figure 13a shows the saturation of the total entropy at the value $S_{tot} = \ln[4]$, which corresponds to the fraction of the four quantum states in the high temperature limit above T_K . The value of the coupling is $t = 10^{-3}$, and the SU(4)-like Kondo state is realized by the octuplet quantum states $|q_a\rangle_8$, where $S_{tot} = 0$. It is an SU(4)-like state, because $\mathcal{G} \approx 2(e^2/h)$ and the octuplet states $|q_{a(b)}\rangle_8$ are different from the pure quantum states $|p_{ls}\rangle_4$ ($|t_{ls}\rangle_4$) (even if $a \gg a'$, see Eq.(7)). At intermediate temperatures between T_K and T_2 , the first entropy plateau $S_{tot} = \ln[4]/4$ is observed. This is strictly related to the Majorana fermion-coupled channel in the CNTQD-TSC device. Analogous results are reported in the literature for the SU(2) Kondo dot coupled to a single Majorana fermion [71, 146], where $S_{tot} = \ln[2]/2$. Below the temperature T_2 the sign of S_T changes to $S_T = -\ln[4]/4$. In this case the contribution of the tunneling entropy is compensated by the entropy of the topological superconductor $S_{TS} = \ln[4]/4$. The characteristic temperature $T_1 = \delta$ is directly related to the lifetime of the

Majorana fermion. In an analogous way the problem was defined in the paper [146], but there the author assumed the finite value of the overlap strength $\Delta_{(0)}$ between the two Majorana fermions in the TSC wire, and S_T has an opposite sign. S_T is positive in the range between T_1 and $T_2 = \Delta_{(0)}$ and takes a negative sign below T_2 . This is a consequence of the self-energy expression in [146]. For the model with the overlapping between Majorana fermions, the self-energy can be expressed as $\tilde{\Sigma}_t^R = (\tilde{t}^2 z)/(z^2 - \Delta_{(0)}^2)$. In our calculations we assumed $\Delta_{(0)} = 0$ (highly coherent TSC wire, where $\lambda_K \approx 0$) and therefore $\tilde{\Sigma}_t^R = \tilde{t}^2/z = \tilde{t}^2/(E + i\delta)$, where δ is a finite lifetime of the Majorana fermion (see [119]). The sign reversal of S_T is observed for the SU*(2) Kondo effect (Fig. 13d), where $T_2 < T_3$ and $T_K < T_2$ in opposite to the SU(4)-like Kondo state for the low coupling regime, where $T_2 < T_3$ and $T_K > T_2$ (the ground state is determined by the octuplet $|q_a\rangle_8$).

Figure 13b shows the entropy for the weak coupling to a single Majorana fermion ($t = 10^{-3}$) with two electrons on the quantum dots $Q = 2e$. The ground state is determined by the duodecuplet $|q_w\rangle_{12}$ (Eq. (9)). The conductance reaches $\mathcal{G} = (7/2)(e^2/h)$, in contrast to the fully SU(4) Kondo state, where \mathcal{G} is quantized to $4(e^2/h)$ (here the Kondo effect is determined by the six quantum states $|d_\nu\rangle_6$). For the duodecuplet state, the tunneling entropy is negative $S_T < 0$ and is compensated by the S_{TS} contribution. In S_{tot} we observe a small boost above $\ln[6]$, around T_2 .

For the strong coupling strength ($t = 20$), the SU*(3) Kondo state is realized in the system for a fractional charge on the quantum dot $Q = (3/2)e$. The quantum conductance reaches $\mathcal{G} = (11/4)(e^2/h) = (1/2)(e^2/h) + (9/4)(e^2/h)$. In the high temperature limit $S_{tot} = \ln[3]$ and is dominated by the S_{QD} contribution. In the low temperature regime, the SU*(3) Kondo state is formed and the contribution of S_T is completely compensated by S_{TS} (blue and red lines in Figure 13c). For the CNTQD-2TSC system with strong coupling t (Fig. 13d) we observe the sign reversal of the tunneling entropy $S_T = \mp \ln[6]/2$ (blue line). The negative entropy of S_{TS} is the consequence of a high order topological state. The ordered part below the temperature T_2 is compensated by the entropy S_{TS} , and for $T > T_2$ we observe an increase of the entropy to a value of $S_{tot} = \ln[6] + \ln[6]/2$ (between T_2 and T_3) at the expense of the tunneling entropy S_T (transient states effect). This is due to the mechanism of expanding the Hilbert space by a topological segment and the realization of the SU*(2) Kondo state by the octuplet state $|q_y\rangle_8$ (Eq. (12)). The Hilbert space is expanded and allows the higher entropy than $\ln[6]$ for 2e on the quantum dots.

Figure 14 shows the influence of the number of Majorana fermions on the SU(4)-like Kondo effect for 1e on QD, i.e. in terms of the weak coupling strength $t = 10^{-3}$, where $T_K > T_2$. The Kondo state for the CNTQD-1TSC system is determined by the octuplet state. In Figure 14 the dark lines symbolize the tunneling en-

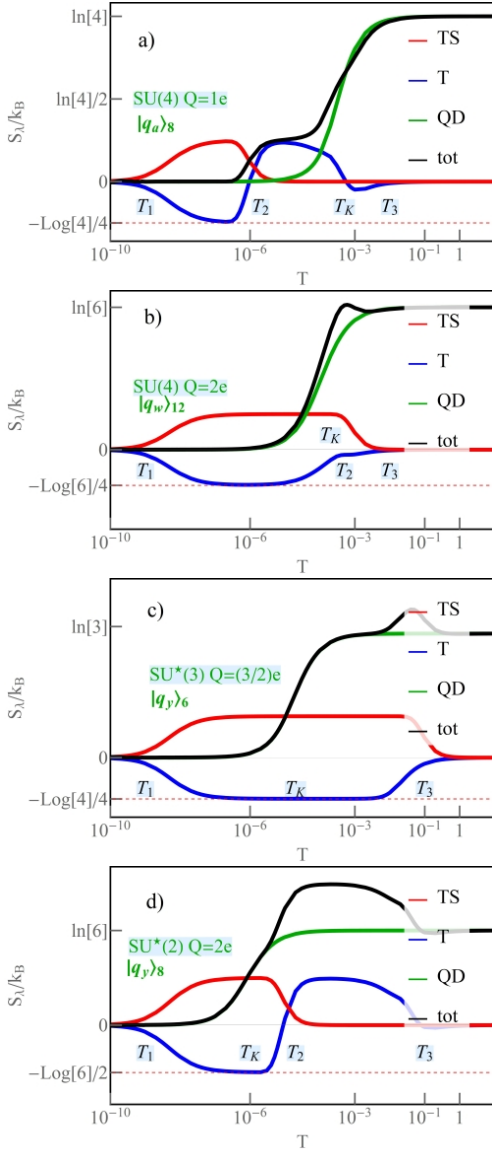


FIG. 13. (Color online) The total entropy S_{tot} , the tunneling entropy S_T , the entropy of the isolated topological superconductor S_{TS} and the entropy of the quantum dot S_{QD} as a function of temperature T for a-c) CNTQD-1TSC device and d) CNTQD-2TSC device. Figures a, b) and Figs. c, d) are plotted for $t = 10^{-2}$ and $t = 20$.

erties S_T and the light curves are associated with the total entropy S_{tot} . For $|q_a\rangle_8$, in the temperature range between T_2 and T_K , the total entropy reaches a quantized value of $S_{tot} = \ln[4]/4$ (blue curves in Fig.14). For $T < T_2$, the tunneling entropy is compensated by the S_T contribution. The SU(4)-like Kondo state is observed from $T_1 = \delta$ to T_K . In the CNTQD-2TSC system the value of the total entropy reaches $S_{tot} = \ln[4]/2$, which is related to the quantum states defined by $|q_a\rangle_{16}$ and the expanding of the Hilbert space via the topological segments $\{|0\rangle, |\uparrow\rangle\}$ and $\{|\bar{0}\rangle, |\bar{\uparrow}\rangle\}$. The inclusion of a third Majorana state γ_{\downarrow} in the CNTQD-3TSC device

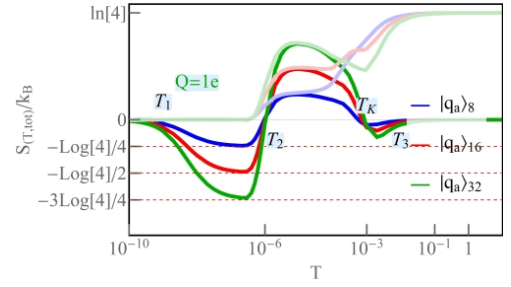


FIG. 14. (Color online) The total entropy S_{tot} , the tunneling entropy S_T , the entropy of the isolated topological superconductor S_{TS} and the entropy of the quantum dot S_{QD} as a function of temperature T for $Q=1e$ and $t = 10^{-2}$. S_T and S_{tot} are represented by dark and light curves. Colors are assigned to the model: CNTQD-1TSC (blue lines), CNTQD-2TSC (green lines) and CNTQD-3TSC (red lines).

increases the value of the total entropy in the range between T_2 and T_K . The total entropy is quantized to $S_{tot} = (3 \ln[4])/4$. The tunneling entropy in this case changes the sign below T_2 , and reaches a maximum positive value of $S_T = S_{tot} = (3 \ln[4])/4$ above the characteristic temperature. In the high temperature limit S_{tot} is saturated for all devices and the quantum limit $S_{tot} = \ln[4]$ is reached. The first plateau in S_{tot} is associated with the Majorana-coupled channels. The normal channels are temperature resistant and participate in the Kondo effect ($T_K > T_2$). The number N_{TS} of Majorana fermions [146], determines the value of the total entropy as follows $S_{tot} = N_{TS} \ln[4]/4$, and contains the information about the SU(4) symmetry of the Kondo state and about the spin-orbital degrees of freedom of the MF state.

There are already several papers in the literature investigating the thermoelectric power in a QD system with a Majorana fermion using the equation of motion technique [114] and the renormalization group [112, 113, 117]. In the first article, the authors analyze a single quantum dot device coupled to a Majorana fermion. The thermoelectric power in this system undergoes a transverse modification, and the authors observe a change in the sign of \mathcal{S} . In the paper [114], the authors analyzed the non-interacting QD-TSC system ($U = 0$) and showed that the thermoelectric transport measurements can be used to detect the Majorana fermion. The authors pointed out that a finite phase shift for the Kondo SU(4) effect could significantly affect the value and sign of the thermal conductivity [114]. In the second paper [117], the authors discussed the spin-resolved thermal signatures of the Majorana-Kondo effect in the DQD-T-shaped system. Using the numerical renormalization group method the authors focus on the two-stage Kondo effect and the leakage of Majorana quasiparticles into the double dot system. Majorana-induced interference with strong electron correlations on the DQD system and is observed in the spin-Seebeck effect. For these problems, the authors have modified the linear response current

$I_s = e^2 L_s^{(0)} \delta V \pm e^2 L_s^{(0)} \delta V_S - (e/T) L_s^{(1)} \delta T$ by adding the spin-dependent voltage in the form $\delta V_S = \delta V_\uparrow - \delta V_\downarrow$. This introduces the possibility to detect spin (orbital) contributions of the TEP, which is particularly interesting for spin (valley) dependent quantum calorimetry.

In terms of the linear response at small temperature δT and voltage difference δV , the electric current I and the thermal current I_Q obey the linear equations presented in Sec. IIIC, where $L_\nu^{(0)}$ and $L_\nu^{(1)}$ are the kinetic transport coefficients. In this paper we study the thermoelectric power (TEP), which can be expressed as follows $\mathcal{S} = (\delta V / \delta T)|_{I=0} = -(1/eT)(\sum_\nu L_\nu^{(0)} / \sum_\nu L_\nu^{(1)})$. Since we mainly want to relate the value of the thermoelectric power to a symmetry of the Kondo effect [45], we introduced the linear coefficient of the thermoelectric power $\gamma_{(S)} = (ST_K)/(2\pi T)$. In general, we can express the TEP for the CNTQD-TSCs device by the following Mott's formula $\mathcal{S} = -(\pi^2/3|e|)[(\sum_\nu d\tilde{q}_\nu/dE|_{E=0} + \sum_{\nu'} d\tilde{q}_{\nu'}/dE|_{E=0})/(\sum_\nu \tilde{q}_\nu + \sum_{\nu'} \tilde{q}_{\nu'})]$, where ν' is associated with the channels coupled to the Majorana fermions. Considering $T \ll T_K$ and $t \approx 0$, the thermoelectric power satisfies the main prediction of FL theory, where the linear coefficient of the specific heat is independent of the quasiparticle interactions ($\gamma_N = \frac{\pi^2}{3} \sum_{\nu=ls} \tilde{q}_\nu$). Based on this assumption \mathcal{S} is proportional to the two-body correlation function (Eq. (42)).

For decoupled CNTQD to TSCs, the linear coefficient of thermoelectric power reaches a value of $\pm\pi/(3\sqrt{2})$ for the quantum states $|p_{ls}\rangle_4$ and $|t_{ls}\rangle_4$ (yellow and blue areas in Fig. 15a and red line in Fig. 15c), as we predicted earlier [45]. \mathcal{S} probes the Kondo resonance close to the Fermi level E_F , and due to the position of the quasiparticle resonance, the linear coefficient of the thermoelectric power in terms of the SU(4) Kondo effect approaches to the finite value $\gamma_{(S)} = -(k_B/|e|)(\pi/3)(\tilde{E}_\nu/T_K) = -(k_B/|e|)(\pi/3)\cos[\delta_\nu]$. In the range of the fractional charges $Q = (5/2)e$ and $Q = (3/2)e$ for the strong Majorana-coupled channel, the thermal transport is determined by low and high energy sextuplets $|q_g\rangle_6$ and $|q_y\rangle_6$. For the SU*(3) Kondo effect, $\gamma_{(S)}$ has reached the quantized value $\pm 3\pi/22$ and the system is still the FL state (light blue and light yellow regions in Fig. 15a, and blue line in Fig. 15c).

The density plot of γ_S shows the transition around t_1 to the two doublet quantum states $|q_x\rangle_2$ and $|q_z\rangle_2$. The transition line is gate independent and appears as the inverse sign of γ_S . The sign of γ_S changes a second time around t_2 , where the Majorana-coupled channels dominate over the normal thermoelectric transport. In the weak coupling regime for $Q = 1(3)e$, we observe the sharp sign reversal for the octuplets $|q_{(b)}\rangle_8$. The transition line is gate-dependent and the inhomogeneous sharp transition line is associated with the compensation of two processes in the Majorana-coupled channel $-\pi T_K(\cot[\delta_\nu][\tilde{\Gamma}_\nu \delta^2 + \tilde{t}^2 \delta]) \approx -\pi T_K(-\cot[\delta_\nu][\tilde{\Gamma}_\nu \tilde{t}^2])$. For $Q = 2e$, the linear thermoelectric coefficient approaches zero in a statement of charge neutrality. This

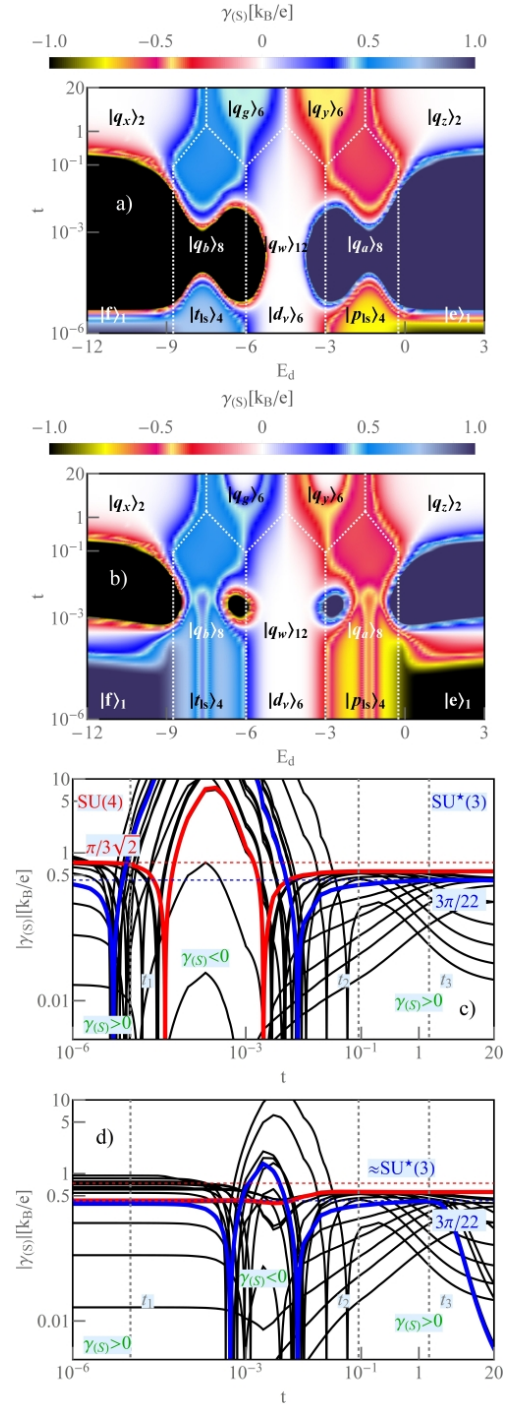


FIG. 15. (Color online) Thermoelectric power in the CNTQD-1TSC device: a, b) The density plot of the linear thermoelectric power coefficient $\gamma_{(S)} = (\mathcal{S})/2\pi T|_{\star}$ as a function of E_d and t for $T = 10^{-8}$ and $T = 10^{-3}$. c, d) The landscape plots of $\gamma_{(S)}$ as a function of t ($\delta E_d = 0.15$).

is the consequence of the Friedel sum rule and the phase shift $\delta_\nu = \pi/2$ at the energy of the Fermi level. The gate-dependent behavior in the NFL phase is also indicated by the slight indentation for $Q = 2e$. In the re-

gion of strong coupling strength, when the system goes to the $SU^*(3)$ Kondo state, for $E_d = -3$ and $E_d = -6$, we observe two flat areas: light yellow and light blue for $Q = 3/2$ and $Q = 5/2$. The γ_S reaches a value of $\gamma_{(S)} = \mp \frac{\pi \sin[\delta_\nu] \sin[2\delta_\nu]}{-4+3 \cos[2\delta_\nu]} = \mp 3\pi/22$, which is significantly different from the value for $SU(3)$ Kondo state, as shown in Figure 15a. This difference is shown by the dark violet line in Fig. 16a ($\gamma_S = \pm\pi/6$), where we have subtracted the contribution to \mathcal{S} from the Majorana fermion channel ν' . This result is confirmed in the literature [45]. $\gamma_S = \pm 3\pi/22$ is observed for the sextuplets, and due to the Onsager relations is associated with the finite topological value of the quantum conductance quantized at $\mathcal{G} = (11/4)(e^2/h)$. A finite temperature gradient $T = 10^{-3}$ changes the picture in γ_S (Fig.15b and Fig. 15d). The finite temperature violates the quantum conductance in the crossover region, where the energy ground state is defined by high-degenerate quantum states $|q_{a(b)}\rangle_8$ (Fig. 9c). The effect of reversal sign for $Q = 1(3)e$ in TEP disappears (red line on Fig. 15d) and reduced to the spots under these temperature conditions (Fig. 15b). For $|p_{l_s}\rangle_4$ and $|t_{l_s}\rangle_4$ we observe decrease of the TEP to $\gamma_S \approx \pm 1/2$. Increasing the temperature gradient (red line in Fig. 15d), the $SU(4)$ Kondo effect is suppressed for $Q = 1(3)e$, therefore $\pm 1/2 < \pm \pi/(3\sqrt{2})$. The transition between $|e\rangle_1$ ($|f\rangle_1$) and the doublets $|q_{x(z)}\rangle_2$ is shifted (Fig. 15b). The same effect was observed for $Q = (3/2)e$ and $Q = (5/2)e$, where t_1 changes its position on the axis of the coupling strength t (blue curve in Fig. 15d). The second point is stable for $T = 10^{-3}$ and is associated with the second compensation processes, where $-\pi T_K(3\tilde{q}_\nu(0))/[(3\tilde{q}_\nu(0) + \tilde{q}_{\nu'}(0))] = -\pi T_K(\cot[\delta_\nu][\tilde{\Gamma}_{\nu'}\delta^2 + \tilde{t}^2(\delta - \tilde{\Gamma}_{\nu'})])/[(3\tilde{q}_\nu(0) + \tilde{q}_{\nu'}(0))(\pi\tilde{\Gamma}_{\nu'}(2\tilde{t}^2 + \tilde{\Gamma}_{\nu'}\delta \csc^2[\delta_\nu])^2)]$. In the intermediate coupling strength between $t = 10^{-2}$ and t_3 the linear coefficient exceeds the value of $\gamma_S \approx \pm 3\pi/22$ (blue line in Fig. 15d). For $T_K^{SU^*(3)} < T$ and $t > t_3$ we observe the suppression of γ_S to zero in the sextuplet regions (blue line in Fig. 15d). The envelope of the NFL-like region, where we observe the strong enhancement of γ_S (black, and dark violet area in Fig. 15a,b), depends strongly on the compensation conditions and the energy level of the quantum dot. An increase in temperature contributes to a gradual narrowing of the NFL crossover region.

Fig. 16 shows the cross sections of $|\gamma_S|$ on a logarithmic plot as a function of E_d for different values of t . In Figure 16a-c, the black lines present $|\gamma_S|$ for $SU(4)$ Kondo state in CNTQD. For $Q = 1(3)e$ we observed the quantized values $|\gamma_S| = \pi/(3\sqrt{2})$. The ground state of the system $|d_\nu\rangle_6$ has on average two electrons ($Q = 2e$) and the thermoelectric power in this region is strongly flattened and suppressed. $|\gamma_S|$ with $t = 5 \times 10^{-3}$ leads to $3\pi/22$ for $1e$ and $3e$ charge sectors (magenta line in Fig.16a). Around the enhancement, we observed two compensation points, where γ_S changed the sign. For this cross section, we have observed the third point of compensation in $Q = 2e$. Orange line shows the saturation of γ_S

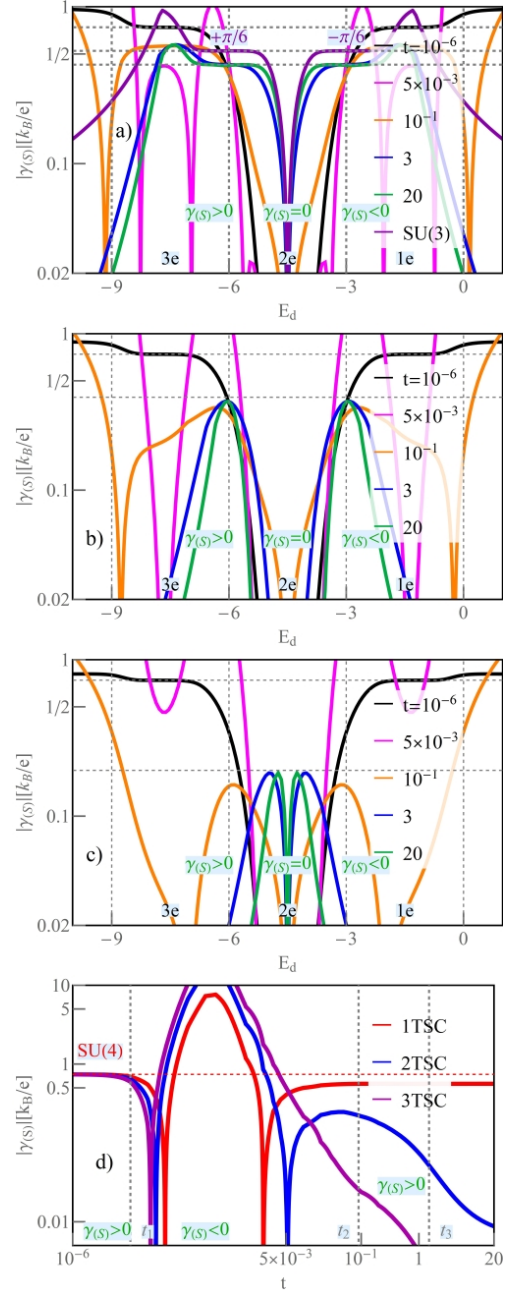


FIG. 16. (Color online) a-c) $|\gamma_S|$ as a function of E_d for CNTQD coupled to 1MF, 2MFs and 3MFs. The dark violet line in figure a shows $\gamma_{(S)} = \pm\pi/6$, the result for the $SU(3)$ Kondo effect (where the $+\uparrow$ channel in \mathcal{S} is neglected) [45]. $\gamma_{(S)}$ changes the sign at a half-filling point $Q = 2e$ d) $|\gamma_S|$ as a function t for $Q = 3e$.

to $\pm\pi/6$ for $Q = 1(3)e$. For the strong coupling strength ($t = 3$ and $t = 20$), $|\gamma_S|$ quantized to $3\pi/22$, where formed $SU^*(3)$ Kondo state for the fractional charge on the quantum dot. The theory for this phase predicts the linear coefficient TEP in the form $\gamma_{(S)} = \mp \frac{\pi \sin[\delta_\nu] \sin[2\delta_\nu]}{-4+3 \cos[2\delta_\nu]}$. At the e-h symmetry point we observed a narrowing line of blocked thermoelectric transport $\gamma_S = 0$ (blue and

green lines in Fig. 16a). Fig. 16b shows $|\gamma_S|$ as a function of E_d for CNTQD-2TSC device. For $t = 3$ and $t = 20$, we observed the area of the $SU^*(2)$ Kondo state, when the quantum dot is in the octuplet state $|q_y\rangle_8$. The thermoelectric power remains strongly suppressed ($|\gamma_S| = 0$), in contrast to the charge degeneracy point, for the Kondo state the region is strictly flattened, as indicated by the scaling energy $T_{[\star]}$. Around the boundary between $|q_y\rangle_8$ and $|q_x(z)\rangle_4$, $|\gamma_S|$ reaches $\pi/8$ and this is associated with the $U^*(1)$ charge symmetry, where the quantum conductance leads to $2(e^2/h)$ (Fig. 6c). For the weak coupling strength to TSC ($t = 5 \times 10^{-3}$), γ_S vanishes and changes sign around $E_d = -(U/2)$ and $E_d = -(5U/2)$ (magenta curve in Fig. 16b). In Fig. 16d for the red and blue line we observe $\gamma_S = 0$. At this point γ_S shows a sharp sign reversal. Red curved on Fig. 16d shows the saturation of γ_S to $\pi/6$ for the strong coupling strength of CNTQD to TSC. The value appears at the charge degeneracy point between the entangled quantum states $|q_x\rangle_2$ and $|q_g\rangle_6$. At this point, the quantum conductance leads to $\mathcal{G} = (3/2)(e^2/h)$. In the case of the CNTQD-3TSC system, TEP is suppressed for $Q = 2e$ and $\gamma_S = 0$ for two degenerate octuplets $|q_x(z)\rangle_8$ at the e-h symmetry point. The switching around the charge degeneracy point reaches $|\gamma_S| = \pi/16$ (blue and green lines in Fig. 16c). Decreasing of the coupling strength t , shift the solution into the NFL-like behavior region, where γ_S reverses the sign and is strongly increases (magenta curve in Fig.16c). The dark magenta line in Fig. 16d shows the evolution of $|\gamma_S|$ as the function of the coupling strength t to the TSCs. Comparing the lines in Fig. 16d, we conclude that increasing the number of TSCs coupled to the quantum dot shifts the second compensation point into the region of strong coupling strength. Even if, the evolution of γ_S explains the Mott's formula, the behavior in the region for the weak Majorana coupling strength has not been scaled by the Kondo temperature, and in this sense we mean about NFL-like phase. The strong enhancement in the weak coupling regime is reflected in the temperature dependence of the entropies S_{QD} and S_{TS} , where the channels ν associated with the Kondo state are much more temperature resistant than the channels ν' interfering with the spin-orbital states in the quantum dots (Fig. 13a).

Before investigating the nonlinear current and shot noise, let's first discuss the influence of the coupling strength to Majorana fermions on the quantities of the two- and three-body correlation functions. Based on the thermodynamics of the Kondo state described in Sec. IIIB, we showed that the general static susceptibilities in Eqs. (21-24) can be expressed as the second and third derivatives of the thermodynamic potential and are related to the density of the quasiparticle states. Using the results of [56, 58], we have postulated the weak-coupling approach to find the off-diagonal two- and three-particle correlations, based on the Wilson ratio $W_{\nu\nu'} = 1 - \tilde{\chi}_{\nu\nu'} / \sqrt{\tilde{\chi}_{\nu\nu}\tilde{\chi}_{\nu'\nu'}} = 1 + \tilde{U}_{\nu\nu'} \sqrt{\tilde{\chi}_{\nu\nu}\tilde{\chi}_{\nu'\nu'}} = 1 + \frac{\delta Q_{\nu\nu'}}{\Delta Q_{\nu\nu'}}$. At this point, we include the (residual) in-

teraction between the quasiparticles $\tilde{U}_{\nu\nu'}$, and we can express as an invariant, the two-particle static susceptibility $\chi_{(z)} = (1/4)(\sum_{\nu} \tilde{\chi}_{\nu\nu} - \sum_{\nu' \neq \nu} \tilde{\chi}_{\nu\nu'})$, which is proportional to the Z-component of the partial fluctuations in the pseudospin space. The same quantum metric can be defined for an odd three-body correlation function in the following way: $\chi_{(z)}^{[3]} = (1/4)(\sum_{\nu} \tilde{\chi}_{\nu\nu\nu} - \sum_{\nu' \neq \nu} \tilde{\chi}_{\nu\nu'\nu'})$. $T\chi_{(z)}(T)$ is screened, when $T\chi_{(z)}(T) = 0$ and the Kondo state is formed. At low temperatures in $\chi_{(z)}(T)$ we observe the saturated constant value, proportional to $1/T_K$ in the limit $T \mapsto 0$. Therefore, the quantities $T_{[\star]}\chi_{(z)}(0)$ and $T_{[\star]}^2\chi_{(z)}^{[3]}(0)$ are the information about the frozen pseudospin and three-particle correlation. In the context of experimental results for single Kondo dot [138], we suggest that more significant information about the symmetry of the Kondo state and all modifications of the $SU(N)$ -Anderson model (i.e. by the coupling term with Majorana fermions) is hidden in the extremely low-temperature measurements of $\chi_{(z)}$ by the charge-sensing technique.

The magnitude of $\lim_{T \rightarrow 0} T\chi_{(z)}(T)$ is screened for the $SU(4)$ Kondo state and is close to zero. For the high temperature limit $T\chi_{(z)}(T)$ reaches the value corresponding to the expectation value of the Z-component of the quadratic Casimir operator (TC_Z^2). Although $T\chi_{(z)}^{[3]}(T)$ in the high temperature limit is not equivalent to the Z-component of the cubic of the Casimir operator (TC_Z^3), for further analysis it is a good approach to investigate the contributions to the nonlinear current and the shot noise, where inelastic processes, beyond the e-h symmetry point play an important role. $\chi_{(z)}^{[3]}$ includes all three-body correlation functions, except $\tilde{\chi}_{\sigma_1\sigma_2\sigma_3}^{[3]}$, which are non-zero only for the tunneling asymmetry between the left and right electrodes ($\tilde{\Gamma}_L \neq \tilde{\Gamma}_R$) [56] (last term in Eq.(18)). Gate-dependent three-particle correlators in quantum dot are the odd parity functions and change the sign when passing through the e-h symmetry point.

Fig. 17a, b shows the density plots of $T_{[\star]}\chi_{(z)}$ and $T_{[\star]}^2\chi_{(z)}^{[3]}$ as a function of E_d and the coupling strength t . The magnitudes are multiplied by the characteristic temperature $T_{[\star]}$, to scale the two-body and three-body correlators proportional to $\sim 1/T_{K,\nu}^2$ and $\sim 1/T_{K,\nu}^4$ (Eqs. (21-24)). $T_{[\star]}\chi_{(z)}(0)$ and $-T_{[\star]}^2\chi_{(z)}^{[3]}(0)$ correspond to the fluctuations of the frozen second and third moments of the pseudospin in CNTQD. In the strongly correlated phase, we observed the Kondo cloud and $T_{[\star]}$ is equal to the Kondo temperature T_K . As we have shown in Fig. 9a, $T_{[\star]}$ varies with the increase of the coupling strength t and reaches characteristic values for a given phase. Fig. 17a presents $T_{[\star]}\chi_{(z)}$ for the $SU(4)$ Kondo state, via the intermediate phase to the $SU^*(3)$ Kondo effect. In the weak coupling regime, $T_{[\star]}\chi_{(z)}$ leads to 0.44 (green line in Fig. 17c), and remains constant for the quantum states $|q_{a(b)}\rangle_8$ (purple area in Fig. 17a). With increasing t , $T_{[\star]}\chi_{(z)}$ reaches to the quantized value $1/4$.

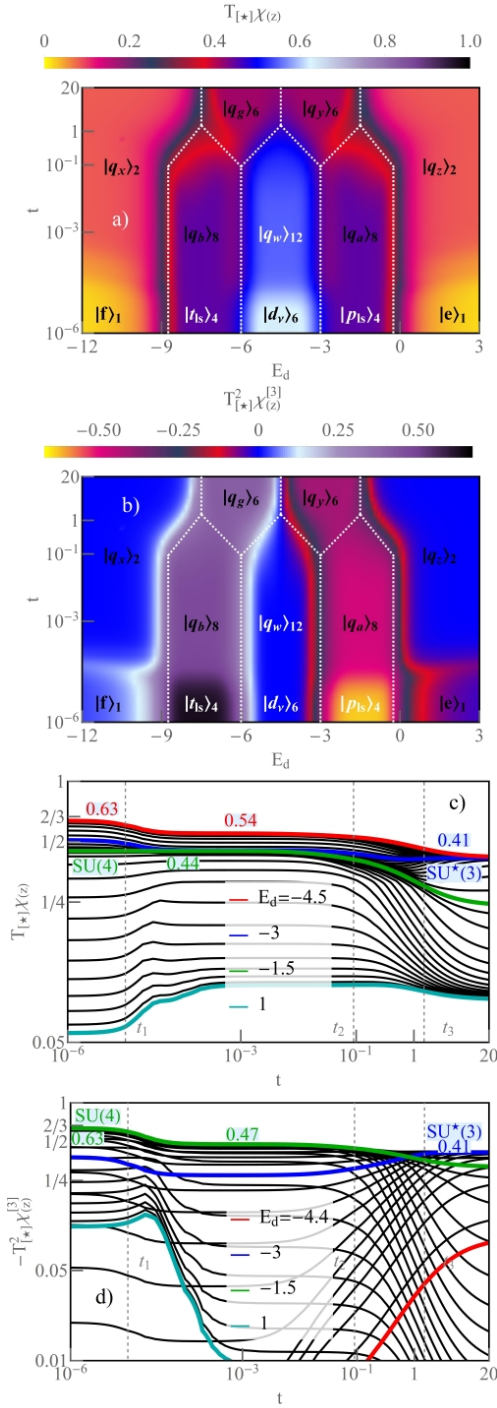


FIG. 17. (Color online) a, b) The density plots of the two-body ($T_{[*]}\chi(z)$) and three-body ($T_{[*]}^2\chi(z)^{[3]}$) frozen correlation functions versus E_d and t for the CNTQD-1TSC device. c, d) The landscape plots of $T_{[*]}\chi(z)$ and $-T_{[*]}^2\chi(z)^{[3]}$ as function of t . The black lines are plotted with an increment of $\delta E_d = 0.15$ from $E_d = -4.5$ to 1. The numbers indicate the values of the correlations in the Kondo phases.

$T_{[*]}\chi(z) = 1/4$ is related to the charge degeneracy line between two quantum states $|q_y\rangle_6$ and $|q_z\rangle_2$. The tran-

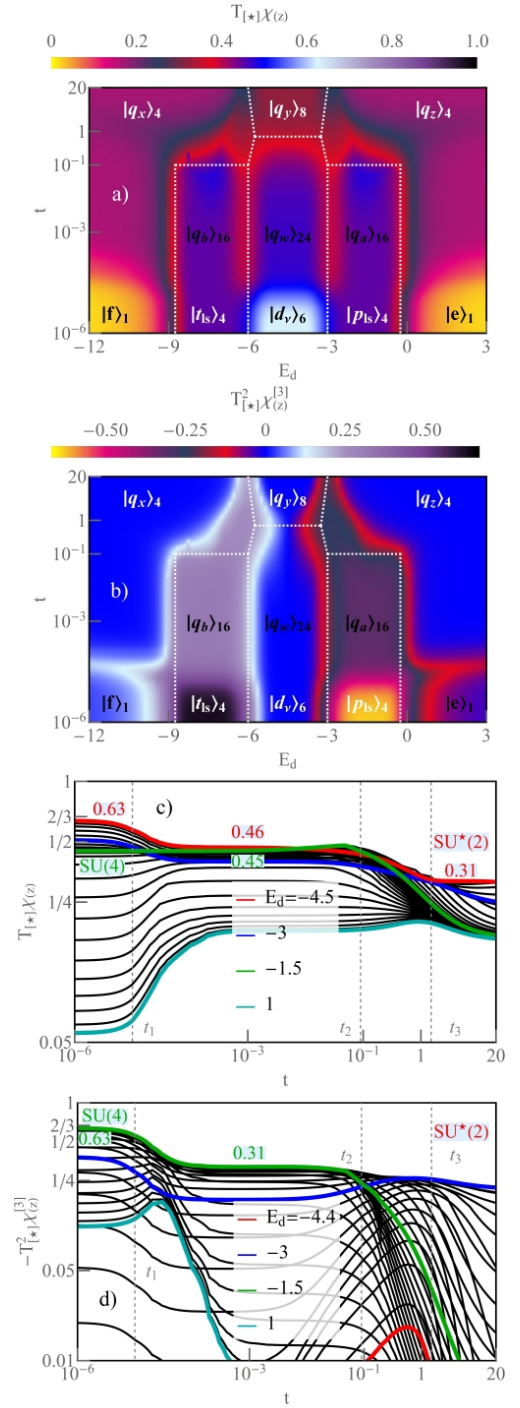


FIG. 18. (Color online) Two- and three-body correlations for the CNTQD-2TSC system: a, b) $T_{[*]}\chi(z)$ and $T_{[*]}^2\chi(z)^{[3]}$ versus E_d and t . c, d) the landscape plots of $T_{[*]}\chi(z)$ and $-T_{[*]}^2\chi(z)^{[3]}$ as function of t .

sition between $|p_{ls}\rangle_4$ and the octuplet $|q_a\rangle_8$ is visible in the three-body correlators (Fig. 17b, d). The value of $-T_{[*]}^2\chi(z)^{[3]}$ changes from 0.63 via 0.47 for the weak coupling strength to 1/3 for the strong coupling limit. In

Figure 17b, we observe the color change in this region from orange to purple for $Q = 1e$, and from black to violet for $Q = 3e$, respectively. The response in the three-particle correlator $-T_{[\star]}\chi_{(z)}^{[3]}$ is much more sensitive for odd charges than in the two-body susceptibilities when the ground state configuration changes, because the high-order correlator, is the derivative of the two-particle correlators (Eq. (22) and Eq. (24)).

For $Q = 2e$ ($E_d = -4.5$) we observe in the two-body correlation a transition between $|d_\nu\rangle_6$ and $|q_w\rangle_{12}$ (light and dark blue regions in Fig. 17a). $T_{[\star]}\chi_{(z)}$ changes from 0.63 to 0.54 at the transition line around t_1 (red line in Figure 17c). The three-particle correlation function for the e-h symmetry point is equal to zero (red line in Figure 17d), due to the oddity and mirror symmetry of $-T_{[\star]}\chi_{(z)}^{[3]}$. The three-body correlator changes the sign at this point. Even if, the transition is observed in $T_{[\star]}\chi_{(z)}$ (red line in Fig. 17c), the argument of the enhancement in the derivative is weaker than vanishing by reciprocal zeroing of the partial three-body correlators in $-T_{[\star]}\chi_{(z)}^{[3]}$. The dependence of $\tilde{E}_{\nu(\nu')}$ is responsible for reducing the three-body correlators in Eqs. (22) and (24). The early experiment confirmed and showed, that the three-body correlators are capable of being measured using the nonlinear current and the shot noise detection [60]. The important issue about the zeroing of higher-order susceptibilities suggests that they will be helpful in the experimental measurements, where the e-h symmetry point is shifted e.g. by the Zeeman compensating field in CNTQD Kondo dot attached to ferromagnetic electrodes [142]. In this device, the exchange field disappears at the e-h symmetry point, the spin Kondo state is restored, and this point is shifted by applying the compensating magnetic field. In terms of the transition between $|f\rangle_1(|e\rangle_1)$, and $|q_x\rangle_2(|q_z\rangle_2)$, we observe around t_1 a slight boost in two-body correlation function and suppression in $-T_{[\star]}\chi_{(z)}^{[3]}$ (dark cyan line in Figures 17c, d). For the fractional charges $Q = (3/2)e$ and $Q = (5/2)e$, the $SU^*(3)$ Kondo state is formed in the strong coupling region, and both correlators, which are significant, are quantized to $T_{[\star]}\chi_{(z)} = |T_{[\star]}\chi_{(z)}^{[3]}| = 0.41$. The system is determined by the two sextuplets $|q_y\rangle_6$ and $|q_g\rangle_6$. The equality of these quantities is due to the expectation values of the boson fields operators, where $|p_{+\downarrow(-s)}|^2 = |d_{20,\uparrow\uparrow,\uparrow\downarrow}|^2 = 1/6$ ($|t_{+\uparrow(-s)}|^2 = |d_{02,\downarrow\downarrow,\downarrow\uparrow}|^2 = 1/6$).

The figures 18 show the higher-order correlation functions for the CNTQD-2TSC device. For $Q = 1e$, we observe a transition from $|p_{1s}\rangle_4$ to $|q_a\rangle_{16}$, and in the strong coupling region to the quantum quartet $|q_z\rangle_4$. In the same way as before, it is difficult to separate the transition in the weak coupling regime, because $a' \ll a$ in the quantum state, and finally for $|q_a\rangle_{16}$ the $SU(4)$ -like Kondo state is realized (even if $\mathcal{G}_\nu = \mathcal{G}_{\nu'} = (1/2)(e^2/h)$, the transmissions are different). Although, in the same weak coupling region, $-T_{[\star]}\chi_{(z)}^{[3]}$ demonstrates two values 0.63 and 0.31 at the transition line between the two

states $|p_{1s}\rangle_4$ and $|q_a\rangle_{16}$ (green line around t_1 in Fig. 18d). The frozen effective Kondo spin features a constant value $T_{[\star]}\chi_{(z)} = 0.45$. In the strong coupling to two Majorana fermions $\gamma_{l\uparrow}$, $T_{[\star]}\chi_{(z)}$ sloped down to $1/8$. The similar result is observed for $E_d = 1$, where in both cases the quantum quartets $|q_z\rangle_4$ dominate (purple region in Fig.18a and dark cyan line in Fig. 18c). For $Q = 2e$ in the two-particle correlation function, we observe three characteristic values: $T_{[\star]}\chi_{(z)} = 0.63$ for the sextuplet $|d_\nu\rangle_6$, 0.46 for $|q_w\rangle_{24}$ and finally constant quantized value 0.31 for the octuplet $|q_y\rangle_8$ (red line in Fig. 18c). $T_{[\star]}\chi_{(z)} = 0.31$ is associated with the restoration of the $SU^*(2)$ Kondo state in the system. In the density plot of $T_{[\star]}\chi_{(z)}^{[3]}$ we observe an enhancement at the transitions between the states $|q_z\rangle_4$ and $|q_a\rangle_{16}$, similarly for $|q_x\rangle_4$ and $|q_b\rangle_{16}$. In the weak coupling strength region, the three-body correlation is quantized to $-T_{[\star]}\chi_{(z)}^{[3]} = \pm 0.31$. $T_{[\star]}\chi_{(z)}^{[3]}$ approaches to $1/3$ around $|f\rangle_1$, where empty $|e\rangle_1$ and fully occupied state $|f\rangle_1$ evolve to quartets, and strongly decreases with increasing of the number of the topological segments (dark cyan line in Fig. 18d). The opposite tendency is observed for two-body correlators, where $T_{[\star]}\chi_{(z)}$ saturates to a constant value (dark cyan lines in Figs. 17-19c).

Fig. 19 shows the evolution of the frozen effective pseudospin moment $T_{[\star]}\chi_{(z)}$ and three-body correlation $T_{[\star]}\chi_{(z)}^{[3]}$ versus E_d with increasing the coupling strength t for the CNTQD-3TSC hybrid device. One of the most significant results is the shogun helmet-like gate dependence of $T_{[\star]}\chi_{(z)}$ and $T_{[\star]}\chi_{(z)}^{[3]}$ in the strong coupling region. Formally, for CNTQD-3TSC, the quantum conductance is suppressed by increasing the tunneling term between the Kondo dot and three Majorana fermions (Fig. 7d). The \mathcal{G} in all three Kondo-like channels, is determined by the interference effect with Majorana fermions. The single normal channel preserves the quantized value $\mathcal{G} = (e^2/h)$ for $Q = 2e$ at the e-h symmetry point, where the ground state is defined by two octuplets $|q_x\rangle_8$ and $|q_z\rangle_8$. Beyond this line, the total quantum conductance reaches $(3/2)(e^2/h)$ and the transport through the normal channel is blocked. In contrast to the static high-order correlations, where we observed the enhancement of $T_{[\star]}\chi_{(z)}$ and the sign reversal in $T_{[\star]}\chi_{(z)}^{[3]}$ around $E_d = -U$ and $E_d = -2U$. There is an amplification associated with a leakage of the quantum states $|q_w\rangle_{48}$, into the forbidden charge region $Q = (5/2)e$ and $Q = (3/2)e$, where $|q_x\rangle_8$ and $|q_z\rangle_8$ are the new energy ground states. The effect requires further analysis, but we can tentatively conclude that the mechanism is due to the presence in two octuplets $|q_x\rangle_8$ and $|q_z\rangle_8$ the states (the basis vectors) from the forbidden charge region in the normal phase. We have marked in red two significant quantum states $|2 \uparrow n_1 n_2 n_3\rangle$ and $|0 \downarrow n_1 n_2 n_3\rangle$ in Eqs. (13-14), which are responsible for the quantum leakage. The physics behind this effect can be explained by the entanglement mechanism with opposite charge-leaking states.

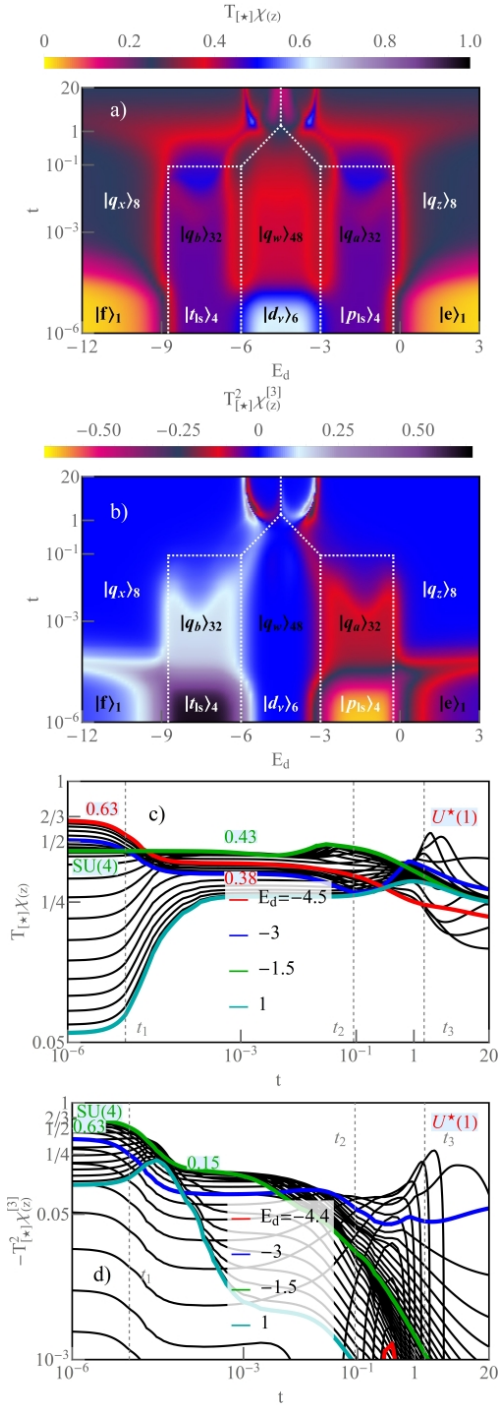


FIG. 19. (Color online) Two- and three-body correlations for the CNTQD-3TSC device: a, b) $T_{[*]}\chi(z)$ and $T_{[*]}^2\chi(z)^{[3]}$ as a function of E_d and t . c, d) The landscape plots of $T_{[*]}\chi(z)$ and $-T_{[*]}^2\chi(z)^{[3]}$ as function of t .

The density plots in Fig. 19a, b show the transition with increasing of t between the empty(fully) occupied states $|e\rangle_1(|f\rangle_1)$ and the low energy octuplets $|q_{x(z)}\rangle_8$. In the weak coupling regime for the high degenerate quantum states $|q_{a(b)}\rangle_{32}$, the frozen two-body susceptibilities

lead to 0.43 (green line in Fig. 19c). For the strong coupling strength, $T_{[*]}\chi(z)$ approaches to 1/4 for both energies $E_d = -1.5$ and $E_d = 1$, where one of the octuplet states dominates (green and dark cyan curves in Fig. 19c). The red curve in Fig. 19c shows three characteristic values: $T_{[*]}\chi(z) = 0.63, 0.38$ and 0.15 . We observed the enhancement of $T_{[*]}\chi(z)$ to 1/2 above $t_3 = U/2$. The charge-leaking states form the shogun helmet-like shape in the density plot of the susceptibilities. Fig. 19d shows $-T_{[*]}^2\chi(z)^{[3]}$. For $E_d = -1.5$, the three-body correlation function changes from 0.63 to 0.15 at the transition line between $|p_{ls}\rangle_4$ and $|q_a\rangle_{32}$ (green curve in Fig. 19d). For the strong coupling region, where two octuplets $|q_z\rangle_8$ dominate, $-T_{[*]}^2\chi(z)^{[3]}$ is reduced, except for the charge-leaking lines (Fig. 19d). In Fig. 19d, the sign of $\chi(z)$ changes between $\pm 1/4$ along the shogun helmet-like shape. For $E_d = 1$, with increasing the coupling strength between quantum dot and Majoranas, the device demonstrates a decrease in $-T_{[*]}^2\chi(z)^{[3]}$ to zero and a saturation in $T_{[*]}\chi(z)$ to 1/4.

Figures 20 show the frozen higher-order quantities: the effective pseudospin $T_{[*]}\chi(z)$, frozen charge susceptibility $T_{[*]}\chi(c)$ and its three-particle correlations $T_{[*]}^3\chi(z)$ and $T_{[*]}^3\chi(c)$ for CNTQD coupled to multi-Majorana device. The charge susceptibility can be expressed as follows $\chi(c) = \sum_{\nu\nu'} \tilde{\chi}_{\nu\nu'}$, and in the analogous way the charge three-body correlator $T_{[*]}^3\chi(z) = \sum_{\nu\nu'} \tilde{\chi}_{\nu\nu'\nu'}^{[3]}$. Fig. 20a compares two-body correlators in three types of nanodevices as a function of t for different gate voltages applied to CNTQD (E_d). The dark, light and lighter lines are the results for CNTQD device coupled to 1TSC, 2TSC and three Majoranas (3TSC). For $E_d = -4.5$ and $E_d = -3$, the frozen effective pseudospin decreases with increase of the coupling strength to the topological segments. The quantum steps observed in $T_{[*]}\chi(z)$ correspond to ground states that determine the specific phase in the strongly correlated hybrid device. In the strong coupling limit, $SU^*(3)$ Kondo state is formed for the fractional charge $Q = (3/2)e$ (dark blue line). For the fractional Kondo phase, the two-body correlator leads to $T_{[*]}\chi(z) = 0.41$ and converges to the same value at the e-h symmetry point, for $Q = 2e$ as mentioned before. At high degeneracy point of two sextuplets $|q_g\rangle_6$ and $|q_y\rangle_6$, the phase is determined by the $U^*(1)$ charge symmetry. The difference between two states, $SU^*(3)$ Kondo and charge $U^*(1)$ phase, is visible in the quantized value of $T_{[*]}\chi(c) = 0$ and $T_{[*]}\chi(c) = 1/3$. Formally, the frozen charge susceptibility is related to the sum of the charge fluctuations $\sum_{l_s} \delta n_{l_s}^2$, and for the screened Kondo cloud $T_{[*]}\chi(c) \approx 0$ (dark blue and light red curves in Fig. 20b). For $E_d = +1$ we observe a gradual increase of $T_{[*]}\chi(z)$ with the growth of the number of Majorana fermions N_{TS} coupled to the CNTQD device (cyan lines in Fig. 20a). $T_{[*]}\chi(z)$ is the magnitude proportional to quadratic of the spin-orbital fluctuations (where $\chi(z) = \sum_{\nu} \int_0^{1/k_B T} d\tau \langle \delta n_{\nu}(\tau) \delta n_{\nu}(0) \rangle < -$

$\sum_{\nu' \neq \nu} \int_0^{1/k_B T} d\tau \langle \delta n_{\nu'}(\tau) \delta n_{\nu'}(0) \rangle$, which increases with N_{TS} for $E_d = 1$, in contrast to the local isospin Z-components shown in Fig. 12. In the strong coupling region, for $E_d = -1.5$, $T_{[\star]}\chi(z)$ converges to $1/4$ in CNTQD coupled to: 1TSC and 3TSC devices. For the strongly coupled CNTQD-3TSC system, the frozen two-body correlator is reduced to $T_{[\star]}\chi(z) = 1/6$. $T_{[\star]}\chi(c)$ vanishes for the SU(4), SU*(3) and SU*(2) Kondo states (Fig. 20b). For $E_d = +1$, the two-body charge susceptibilities start from $1/8$ for uncoupled QD to TSCs. In the intermediate and strong coupling region, $T_{[\star]}\chi(c)$ is enhanced by the number of topological wires N_{TS} (cyan lines in Fig. 20b). $T_{[\star]}\chi(c)$ leads to 0.34 for $|q_z\rangle_2$, 0.62 for $|q_z\rangle_4$ and $T_{[\star]}\chi(c) = 0.87$ for $|q_z\rangle_8$. In particular the partial susceptibilities indexed by ν' channels coupled to Majorana fermions for $E_d = +1$ raise the value of $T_{[\star]}\chi(c)$. In the charge susceptibility we observe a dip around t_3 due to the opposite contributions of diagonal and off-diagonal parts in the sum of $\chi(c) = \sum_{\nu\nu'} \tilde{\chi}_{\nu\nu'}$. Between t_1 and t_2 for $E_d = -4.5$ and -1.5 , when CNTQD is determined by the high degenerate states, we observe low fluctuations of $T_{[\star]}\chi(c)$, characterized for the Kondo states. Above t_2 , for strong coupling strength, the two-body charge correlator increases and saturates at finite values, when the quantum states are in the U*(1) charge phases (all lines except the dark blue and light red curves in Fig. 20b). The three-body correlation function $T_{[\star]}^{[3]}\chi(z)$ versus t is shown in Fig. 20c. $T_{[\star]}^{[3]}\chi(z)$ shows three quantized values, related to the change of the quantum ground states (blue and green lines in Fig. 20c). In the strong coupling region, $T_{[\star]}^{[3]}\chi(z)$ vanishes for the CNTQD-2TSC and CNTQD-3TSC devices, where the quartets $|q_z\rangle_4$ and the octuplets $|q_z\rangle_8$ determine the lowest energy solution in the system. The transition between the empty occupied state and the entangled doublet, quartet and octuplet for $E_d = 1$ is manifested by raising the value around $t_1 = \delta$. For the fractional SU*(3) Kondo state, $T_{[\star]}^{[3]}\chi(z)$ is quantized to 0.41 (dark blue line in Fig. 20c). We observed a similar evolution in the frozen three-body charge correlation $T_{\star}^{[3]}\chi(c)$ (Fig. 20d). For CNTQD coupled to 2TSC and 3TSC, in particular for the weak coupling region, $T_{\star}^{[3]}\chi(c)$ changes sign due to the dominant role of the off-diagonal three-body correlations (light and lighter green curves in Fig. 20d). At the e-h symmetry point, both correlations $T_{[\star]}\chi(z)$ and $T_{\star}^{[3]}\chi(c)$ are suppressed and obtains to zero.

Figures 21 and 22 show the fluctuations of the local effective pseudospin $TC_Z^2 = TC_{Z(K)}^2 + TC_{Z(M)}^2$, expressed by the expected value of the Z-component of the quadratic Casimir operator [137]. The quadratic Casimir operator is written as a sum of two parts $C_{Z(K)}^2$ and $C_{Z(M)}^2$ (dark and light lines in Figs. 21-22). The first contribution describes the local fluctuations in the ν channel associated with the normal states and the second $C_{Z(M)}^2$, represents the two-particle correlations in

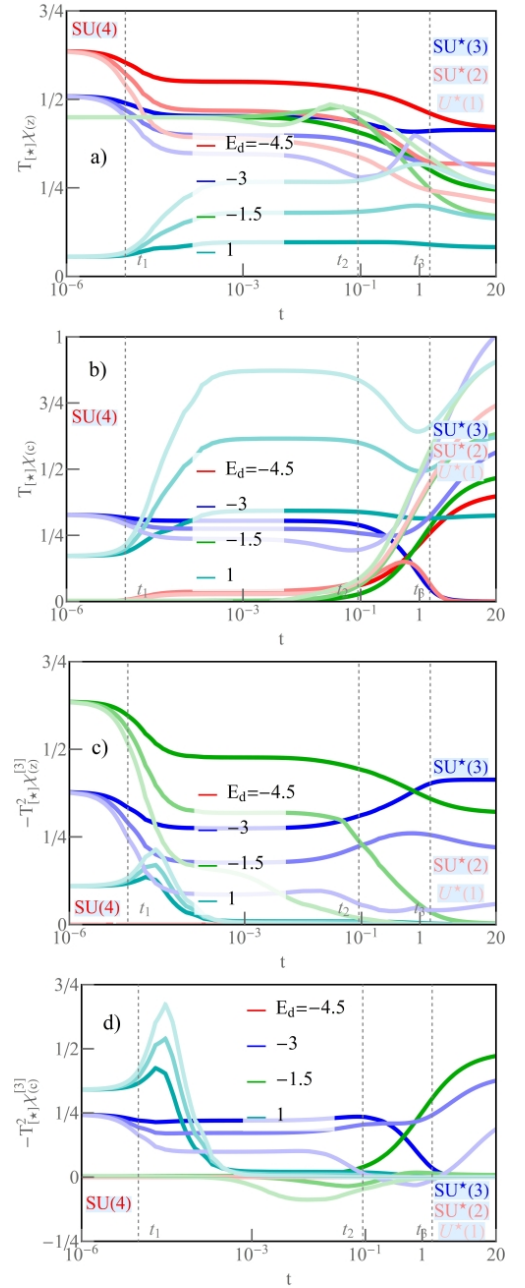


FIG. 20. (Color online) a, b) $T_{[\star]}\chi(z)$ and the frozen charge susceptibilities $T_{[\star]}\chi(c)$ against t . c, d) $-T_{[\star]}^2\chi^{[3]}$ and $-T_{\star}^2\chi^{[3]}$ as a function of the coupling strength t . Dark, light and brightest color of the lines show the results for CNTQD coupled to MF, 2MFs and 3MFs.

the ν' Majorana-coupled channel. We have expressed the Casimir operator by the boson fields operators in Eqs. (29-34). For the CNTQD-TSC device the fluctuations in the normal channels are higher than the contribution in the ν' channel: $TC_K^2 > TC_M^2$. For $E_d = -4.5$, $TC_{Z(K)}^2 = 1/3$ and is constant with increasing the tunneling strength, in contrast to $TC_{Z(M)}^2$, which changes from 0.16 to 0.1 in the strong coupling limit (dark red and light

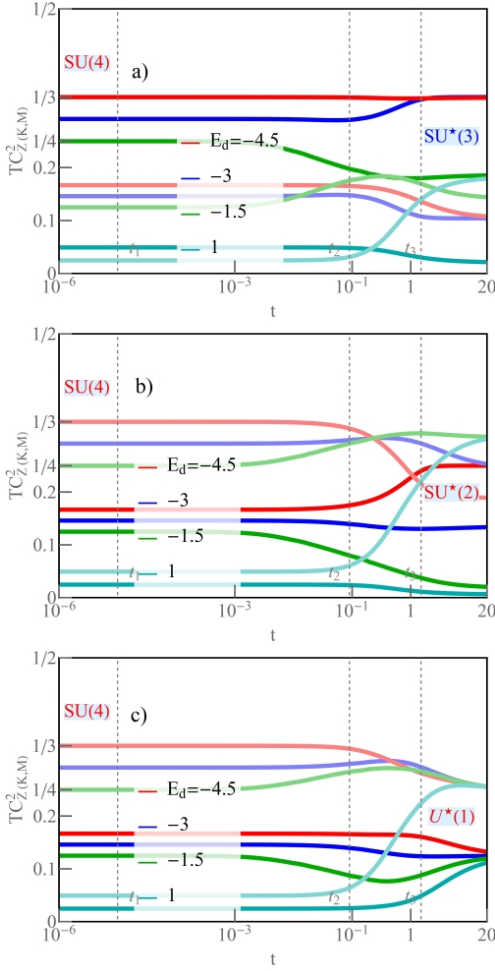


FIG. 21. (Color online) a-c) The expected value of the quadratic of the Casimir operator C_Z^2 as a local spin fluctuations versus t for CNTQD-TSC, CNTQD-2TSC and CNTQD-3TSC devices. Dark and light lines present $TC_{Z(K)}^2$ and $TC_{Z(M)}^2$ in Kondo and Majorana-coupled channels.

red curves in Fig. 21a). For this behavior is responsible the transition from $|q_w\rangle_{12}$ in the Kondo state to the $U^*(1)$ charge symmetry (dark and light cyan lines in Fig. 22a). For both quantum states $|q_g\rangle_6$ for $Q = (5/2)e$ and $|q_y\rangle_6$ for $Q = (3/2)e$, $TC_{Z(K)}^2$ reaches $1/3$, and $TC_{Z(M)}^2 = 0.1$, which is the fingerprint of the $SU^*(3)$ Kondo state [46]. In practice, the states in the ν channel are screened by the nonlocal fluctuation $TC_{s-d}^2 = \lim_{T \rightarrow 0} T\chi_{(z)}(T) - TC_{Z(K)}^2(T) = -1/3$ consisting of the quantum dot and electrode states (TC_{s-d}^2 is called the nonlocal quadratic Casimir operator). In $T\chi_{(z)}(T)$, in the strong coupling limit, with increasing temperature we should observe two quantum steps, first for the Majorana-coupled channel ν , where $T\chi_{(z)}(T) = 0.1$ and second for the high temperature limit $T\chi_{(z)}(T) = 0.1 + 1/3$, in contrast to the entropy, where the tunneling entropy is compensated by the topological part (Fig. 13c). For $E_d = +1$, the transport is determined by the Majorana-coupled channel, and

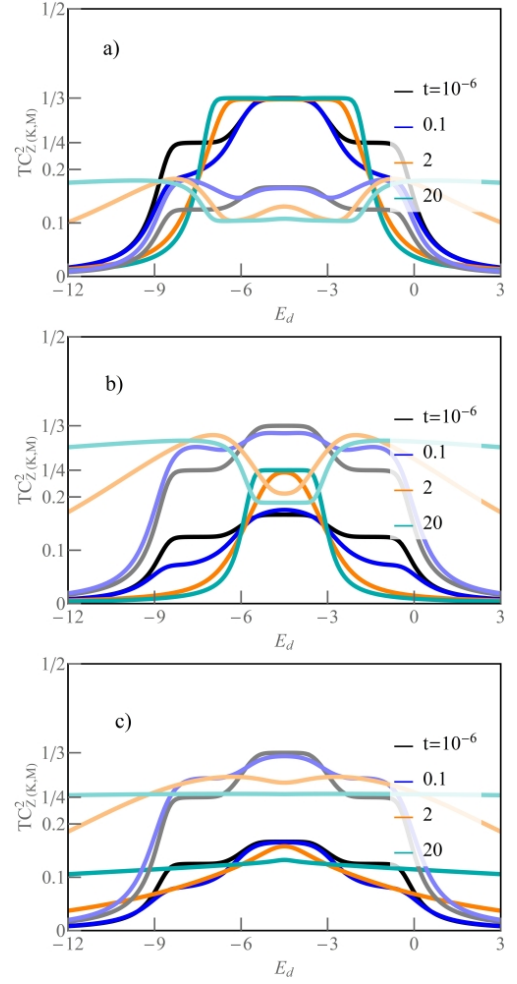


FIG. 22. (Color online) a-c) The expected value of the quadratic of the Casimir operator C_Z^2 as a function of E_d with increasing of t for the CNTQD-TSC, CNTQD-2TSC and CNTQD-3TSC devices. Dark and light lines present $TC_{Z(K)}^2$ and $TC_{Z(M)}^2$ in Kondo and Majorana-coupled channels.

$TC_{Z(M)}^2 > TC_{Z(K)}^2$. In the strong coupling limit, the $TC_{Z(M)}^2$ saturates and reaches to 0.18 (light cyan lines in Fig. 21a and 22a). In this region, $|q_z\rangle_2$ is the ground state and the spin and isospin components achieve $|S_Z| = 1/4$ and $|I_Z| = 3/4$ (Fig. 12a).

In CNTQD-2TSC, the tendencies of the fluctuations are opposite $TC_{Z(M)}^2 > TC_{Z(K)}^2$, except for $E_d = -4.5$, in the strong coupling limit, where the $SU^*(2)$ Kondo state is realized. With increasing the coupling strength t , for $Q = 2e$, we observed the transition between the Kondo state for $|q_w\rangle_{12}$ and $SU^*(2)$ Kondo effect. This occurs, when $TC_{Z(M)}^2 < TC_{Z(K)}^2$ and the fluctuation in the Majorana-coupled channel achieves $TC_{Z(M)}^2 = 0.2$ and in the channel associated with the Kondo state $TC_{Z(K)}^2 = 1/4$ (dark and light cyan lines in Fig. 22b and both red curves in Fig. 21b). For these quantities are responsible the expected values of the boson fields op-

erators Eqs. (31-32). As we see, in the topological qubit states $|q_y\rangle_8$ in Eq. (12), only two bosons of d_ν , single p_{l_s} and one t_{l_s} contribute to the increase of the fluctuations. The spin and the isospin are zero for the $SU^*(2)$ Kondo effect, due to the symmetry of the strongly correlated state and are determined by the values of the boson fields operators in Eq. (44-45). Topological states in the octuplets $|q_y\rangle_8$ contribute to the increase of the total entropy for the intermediate temperature (black line in Fig. 13d). For $|q_z\rangle_4$ states, in the strong coupling region for $E_d = -1.5$ and $E_d = +1$, the transport is determined by the channels coupled to Majorana fermions (light green and cyan lines in Fig. 21b), and only $TC_{Z(M)}^2 = 0.29$ contributes to the pseudospin fluctuations (light cyan line in Fig. 22b). In this region we observe a sharp switch in the Z-component of the spin and isospin, $|S_Z| = |I_Z| = 1/2$ (Fig. 12b). The topological qubits $|q_{-z_n(\bar{n})}\rangle$ are determined by the entanglement of the empty, two single occupied states and one double occupied state in the auxiliary slave boson representation (Eq. (11)).

For the CNTQD-3TSC device, the contributions from the ν' channels coupled to the three Majorana fermions exceed the fluctuation from the normal channel: $TC_{Z(M)}^2 > TC_{Z(K)}^2$ (Fig. 21c). In the strong coupling limit, the octuplet states $|q_x\rangle_8$ and $|q_z\rangle_8$ dominate on the both sides of the e-h symmetry point. With increasing t we observe the completely flat and constant gate-dependent behavior for both fluctuations $TC_{Z(M)}^2 = 1/4$ and $TC_{Z(K)}^2 = 0.1$ (light and dark cyan curves in Fig. 22c). This is caused by the fact that topological superconductors use $N - 1$ degrees of freedom of the QD.

Let's turn to the problem of the shot noise in the CNTQD-TSC devices. According to the results in the paper [56], the current and the shot noise (in terms of linear voltages) can be expressed by the transmission in the Landauer-Büttiker form Eqs. (37-38). The shot noise formula is derived using the Hartree-Fock approximation (HFA) for a two-particle Green's function [139, 147]. Finally, in the context of the shot noise (the fluctuations of the current), we can introduce the linear Fano factor $F_0 = \lim_{V \rightarrow 0} S_0/2|e|I_0$ in the low bias region. The quantum magnitude for certain quantum systems yields to the quantized values less than or greater than 1. For the non-interacting particles, F_0 is equal to 1. F_0 manifests two types of statistical behavior: sub-Poissonian noise ($F_0 < 1$) and super-Poissonian noise ($F_0 > 1$). The particles in the nanodevice (mostly electrons) are bunched or anti-bunched, by the repulsive and attractive Coulomb interaction. The type of interaction between the quasiparticles determines the value of the Fano factor, e.g. Cooper pairs in BCS superconductors demonstrate 2, the Fano factor of the Dirac fermions is equal to 1/3, and for the Kondo singlet quasiparticle, the experiments show 5/3. In the CNTQD-TSCs device, we couple the Kondo quasiparticle to Majorana fermions (real half-fermion state), and by increasing of the tunneling terms, the Kondo cloud is modified by the interference effects.

We observe the coexistence of two states, the Majorana-Kondo state. In the first part of the discussion, we analyze the ballistic transport (for low bias voltage), where the current fluctuation S_0 is described by the transmission. In this picture, the quasiparticle in the Kondo state, behaves like non-interacting particles (in particular for the $SU(2)$ Kondo effect, where $\delta_\nu = \pi/2$). This quantity is observed in the linear coefficient of the specific heat, where in the frame of FL theory $\gamma_N = \frac{\pi^2}{3} \sum_{\nu=l_s} \tilde{\rho}_\nu$ [58]. In general, the non-interacting particles are modified by the renormalization, in this sense the symmetry of the $SU(4)$ Kondo effect and the interaction reveal in low-bias measurements. Finally, the Fano factor consists of the linear and nonlinear parts in the following form:

$$F = \frac{S}{2|e|I} = \frac{S_0V + S_KV^3 + 0[V^5]}{2|e|(I_0V + I_KV^3 + 0[V^5])} \quad (49)$$

where the nonlinear part is measured by subtracting the linear parts S_0 and I_0 from the noise and the currents:

$$F_K = \frac{|S_K|}{2|e||I_K|} = \frac{\delta S_K}{\delta I_K} \approx \frac{d^2S/dV^2}{d^2I/dV^2} \quad (50)$$

F_K is the nonlinear contribution to the shot noise and includes the elastic and inelastic scattering processes, which develops from the high-order correlations and the interaction between dressed Kondo quasiparticles ($eV, T < T_K$). In the further calculations, we have adopted the Eqs. (39-40) from [56].

Fig. 23a shows the density plot of F_0 as a function of E_d and the coupling strength t . In Fig. 23a, for the CNTQD-1TSC device, with respect to the transition from the empty (full) occupied states $|e\rangle_1(|f\rangle_1)$ to the doublets $|q_z\rangle_2$ ($|q_x\rangle_2$), we observe a reduction of the shot noise from $F_0 = 1$ (red area in Fig.23a) to a value of 1/2 (dark orange region in Fig.23a). Comparing the figures in section 23, the reduction is quantized to $F_0 = 1/2$, regardless of the number of TSC segments in the hybrid devices. This is a consequence of the geometry of the measurements (T-shaped like device). The N_{TS} dependence in F_0 is detectable, only in the direct coupling geometry, where the TSC is one of the transport electrodes, where we measure the Andreev reflection contributions to the shot noise [86]. Formally, in the systems with direct coupling, where the quartet $|q_{x(z)}\rangle_4$ and the octuplet $|q_{x(z)}\rangle_8$ are the ground states, we should observe $F_0 \gg 1$ in the strong coupling limit.

$F_0 = 1/2$ has been confirmed for the QD-TSC circuit [86, 146], and is related to the fact that the sum of transmissions in the Majorana-coupled channel reaches $(1/2)(e^2/h)$. One comment is necessary here, F_0 leads to 1/2, only beyond the e-h symmetry point, at the charge degeneracy line the device is in the $U^*(1)$ charge symmetry phase, the quantum conductance is equal to $\mathcal{G} = (3/2)(e^2/h)$ and the linear Fano factor converges to 1/6 (the increase of the quantum conductance is also confirmed by NRG calculations [141]).

The difference between F_0 in CNTQD-TSCs devices is significant in the measurements of S_0 and I_0 . $F_0 = 1/2$

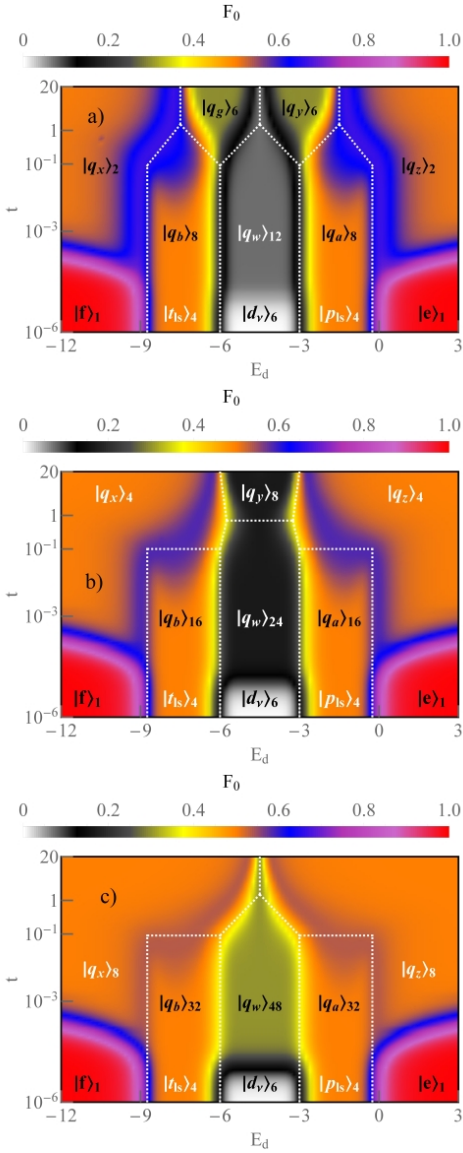


FIG. 23. (Color online) a-c) The density plot of the linear Fano factor $F_0 = S_0/(2eI_0)$ versus E_d and t for the CNTQD-MF, CNTQD-2MFs and CNTQD-3MFs systems.

has a different source for the CNTQD-1TSC circuit. For $|q_{x(z)}\rangle_2$ we observe the noise $S_0 = (1/4)(e/h)$ and the current quantized to $2|e|I_0 = (1/2)(e/h)$. For CNTQD-2TSC, $F_0 = 1/2$ is related to two quartets $|q_{x(z)}\rangle_4$, where $S_0 = (1/2)(e/h)$ and $2|e|I_0 = 1(e/h)$. For a system coupled to three Majorana fermions $F_0 = 1/2$, but $S_0 = (3/4)(e/h)$ and $2|e|I_0 = (3/2)(e/h)$, and the transport is determined by two octuplets $|q_{x(z)}\rangle_8$. The value $F_0 = 1/2$ is observed for $t > t_1$ and is symbolized by the orange area in Fig. 23 and by the dark cyan lines in Figures 24a-c. The black lines in Fig. 24 are plotted in the range from $E_d = -4.5$ to 1 with the increment $\delta E_d = +0.15$.

Let us discuss F_0 for the e-h symmetry point ($E_d = -4.5$). Increasing t we observe the transition in F_0 be-

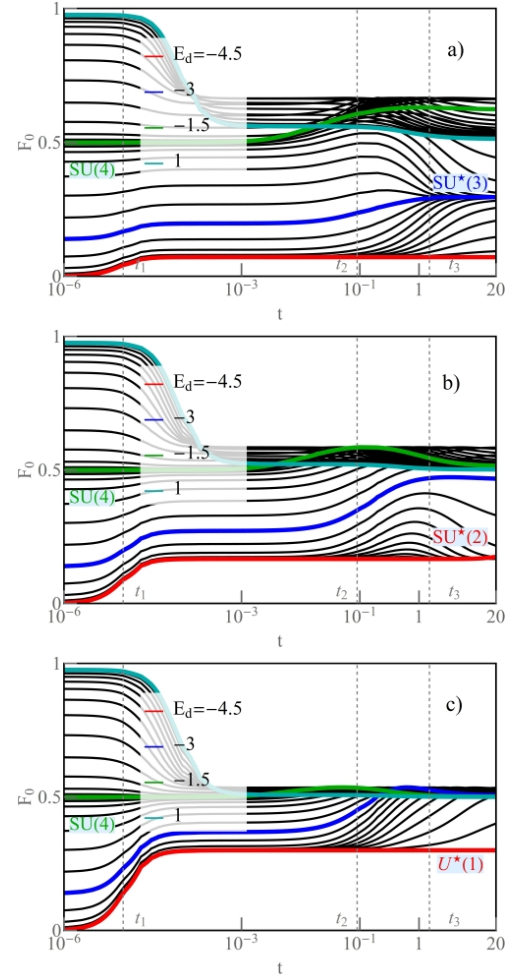


FIG. 24. (Color online) a-c) The landscape plots of F_0 as a function t with increment $\delta E_d = 0.15$ for CNTQD-TSC, CNTQD-2TSC and CNTQD-3TSC devices.

tween the quantum state $|d_s\rangle_6$, where $F_0 = 0$, to the finite quantized values, i.e. $F_0 = \frac{S_0}{2|e|I_0} = \frac{1/4}{7/2} = 1/14$ for $|q_w\rangle_{12}$, $F_0 = \frac{1/2}{3} = 1/6$ for $|q_w\rangle_{24}$ and $F_0 = \frac{3/4}{5/2} = 3/10$ for $|q_w\rangle_{48}$ (Fig. 23 and red curves in Fig. 24). $F_0 = 1/6$ is related to the $SU^*(2)$ Kondo state, $F_0 = 1/14$ and $F_0 = 3/10$ are determined by the $U^*(1)$ charge symmetries with twelfold and sixteenfold degeneracy point. For the fractional $SU^*(3)$ Kondo state, $F_0 = 13/44$, where the noise is quantized to $S_0 = (13/16)(e/h)$ and the current leads to $2|e|I_0 = (11/4)(e/h)$ (dark yellow region in Fig. 23a and blue line in Fig. 24a). For the quantum states with $Q = 1(3)e$ on the dot, in the range of weak coupling strength $F_0 \approx 1/2$ (orange region in Fig. 23 and green lines in Fig. 24). The transition between the states $|p_{l_s}\rangle_4(|t_{l_s}\rangle_4)$ and $|q_a\rangle_{8(16,32)}(|q_b\rangle_{8(16,32)})$ appears in the shot noise, exactly like in the quantum conductances (Figs. 5-7a). Finally, we can conclude that increasing the number of N_{TS} topological superconducting wires coupled to the CNTQD squeezes the Fano factor in the landscape plots to $1/2$ in the limit $N_{TS} = N$.

In the V^3 bias range, the nonlinear Fano factor dominates, which consider the information of the interaction between Kondo quasiparticles. The effective sbMFA Hamiltonian, includes the Coulomb interaction, but formally to calculate the inelastic scattering processes, we take into account the fluctuations in the free energy $\Delta\tilde{F}$. On this basis we can introduce into the system the quantity called the Wilson coefficient, which for the interacting quasiparticles leads to $W_{\nu\nu'} - 1 > 0$, and exactly in the backscattering processes with the Kondo singlet, takes the value of $1/(N-1)$ for the N-orbital Anderson model [53, 56]. CNTQD-TSC devices with N-1 channels coupled to the Majorana fermion behave like the Fermi liquid systems, where $n_\nu = \delta_\nu/\pi$. Based on this assumption, and on the fact that the shot noise and the current have similar linear and the third power bias contributions, we can formally adopt in the first approach the result of the paper [56]. Previous papers, using the Fermi liquid approach, showed that the nonlinear current and shot noise can be expressed by the sum of the elastic and inelastic contributions [51, 52, 55]. In [56] the authors showed for the first time that the FL coefficient can be expressed by the two- and three-body correlation functions ($\chi_{\nu\nu'}$ and $\chi_{\nu\nu'\nu'}^{[3]}$), and the factors $c_{V,\nu}$ and $c_{S,\nu}$ at V^3 in the current and shot noise series are given by the sum of the high-order correlation functions consisting of the backscattering processes found by using the Ward identities [135] and including the vertex functions [56].

Figure 25 shows the shot noise and current in the nonlinear regime for $V < T_K$, which includes the information about the quasiparticle interaction in the Kondo state. The quantities are expressed in terms of two- and three-particle correlation functions. The $\delta I_K = T_{[*]}^2 |I_K|$ is the excess current multiplied by the square of the characteristic temperature $T_{[*]}$. The two-body correlation functions determine the δI_K . The static susceptibilities are expressed by Eqs. (21-24), and are thus inversely proportional to the square of T_K , so that the characteristic temperature scales the quantities to quantum values in the range between 0 and 1 for δI_K , and from 0 to 3/2 for $\delta S_K = T_{[*]}^2 |S_K|$. The δI_K is directly expressed by the sum of the factors $c_{V,\nu}$ and $c_{V,\nu'}$ for the uncoupled and coupled channels to the topological superconductor. The two-particle and three-particle scattering in $c_{V,\nu}$ have opposite signs, and in certain ranges of parameters t and E_d the processes can be equivalent. Figure 25a shows the density plot of δI_K and Fig. 25b presents the landscape plot of the nonlinear current as a function of t . The δI_K in Figure 25b is plotted with an increment of $\delta E_d = 0.15$. The colored lines represent δI_K in the different ground state regions. For $E_d = 1$ (dark cyan line in Fig. 25b), with increasing t we evolve from the empty state $|e\rangle_1$ to the doublet $|q_z\rangle_2$. The δI_K in terms of the weak and strong coupling regime to the Majorana fermion takes the value $\delta I_K \approx 0.08$ and for $t = 0$ the value $\delta I_K = 0.018$. Between intermediate and strong coupling strength we observe a clear point where the current is extinguished $\delta I_K = 0$ (yellow line in Figure 25a and dark cyan curve

in Figure 25b). Above this point, the contribution of the two-particle correlation dominates over the three-particle correlation, and δI_K reverses the sign. For $E_d = -1.5$ (green line in Fig. 25b), we observe three characteristic values of $\delta I_K = 0.33$ for the quartet $|p_{ls}\rangle_4$, $\delta I_K = 0.25$ for the octuplet $|q_a\rangle_8$ and $\delta I_K \mapsto 0$ at the boundary of the charge areas $Q = (3/2)e$ and $Q = (1/2)e$. For $Q = 2e$ ($E_d = E_{e-h}$, red line in Fig. 25b), the current takes on the values: $\delta I_K = 0.89$ for the $|d_\nu\rangle_6$ states, $\delta I_K = 0.69$ for the duodecuplet states $|q_w\rangle_{12}$ and $\delta I_K = 0.525$ in the strong coupling regime at the degeneracy point between the sextuplets $|q_g\rangle_6$ and $|q_y\rangle_6$. For $SU^*(3)$ (the blue line in Fig. 25b), the nonlinear current reaches a value of $\delta I_K = 0.515$ for the ground state $|q_y\rangle_6$. Fig. 25a shows that the zeroing of the current occurs at the boundary between the doublets $|q_x\rangle_2$ and $|q_z\rangle_2$.

Figures 25c and 25d illustrate the nonlinear shot noise $\delta S_K = T_{[*]}^2 |S_K|$ as a function of E_d and t . In contrast to the current factor Eqs. (39-40), the number of scattering processes in δS_K leads to a double line of the reduction of the shot noise (light yellow lines in Fig. 25c). The δS_K is a fluctuation of the current, called second cumulant [148], which zeroes predominantly at other points than the current. For $E_d = +1$, δS_K has double zero points and the nonlinear shot noise between the compensation points is negative $\delta S_K < 0$ (dark cyan line in Fig. 25d). This follows from a simple fact, the coefficient $c_{S,\nu}$ is expressed by doubling the phase shift $2\delta_\nu$ and quadrupling $4\delta_\nu$ in the trigonometric functions. The zeroing effect, as before, occurs on the boundary with the doublet states $|q_{x(z)}\rangle_2$. The δS_K for $E_d = +1$, with increasing the coupling strength takes values of $\delta S_K = 0.016$ for the empty state $|e\rangle_1$, in the weak and strong coupling range it is $\delta S_K = 0.07$. A pronounced suppression of the noise $\delta S_K = 0$ occurs for the two coupling values $t = 0.25$ and $t = 1.5$ (yellow line in Figure 25c, and dark cyan curve in Figure 25d). At these points, the transport is noiseless. The $\delta S_K < 0$ occurs in the interval between these specific lines. The magnitude of the negative noise, is affected by the static three-particle correlators, which increases the negative value of the shot noise. This is a very interesting result considering that the noise is a variance of the nonlinear current [148]. For $E_d = -1.5$ (the green line in Fig. 25d), we observe a constant value of $\delta S_K = 0.11$ for the quartet $|p_{ls}\rangle_4$ and the octuplet $|q_a\rangle_8$. The $\delta S_K = 0$, at $t = 4.5$, and the noise takes on a negative value of $\delta S_K = -0.013$ in the strong coupling regime, i.e. for the quantum state $|q_z\rangle_2$, with dominant role of the three-body correlators. For $Q = 2e$ ($E_d = E_{e-h}$, red line in Fig. 25d), the shot noise is quantized to $\delta S_K = 1.33$ for $|d_\nu\rangle_6$, $\delta S_K = 1.02$ for the duodecuplet quantum state $|q_w\rangle_{12}$ and reaches 0.74 for the strong coupling regime at the degeneracy point of two sextuplets $|q_g\rangle_6$ and $|q_y\rangle_6$. The δS_K for $E_d = -3$ (blue line in Fig. 25d) at the boundary of the quantum states of $|d_\nu\rangle_6$, $|p_{ls}\rangle_4$ and $|q_w\rangle_{12}$, $|q_a\rangle_8$ takes on values of 0.44 and 0.35. Finally, for the $SU^*(3)$ Kondo state, the shot noise reaches $\delta S_K = 0.35$. The blue line shows a

characteristic minimum around $t \approx 0.25$, most likely due to a quantum state transition from $U^*(1)$ charge symmetry to threefold $SU^*(3)$ symmetry with a reduction of c_S by contributions from the three-body correlation functions. This is the main argument why the three-particle interactions are significant in the current and shot noise for the states with broken symmetry.

Fig. 26 shows the shot noise and current in the nonlinear regime for the CNTQD-2TSC device. For $E_d = +1$ (dark cyan line in Fig. 26b), δI_K reaches 0.16 with increasing t , where the quantum state changes from the $|e\rangle_1$ to the quartet $|q_z\rangle_4$. The δI_K between the weak and strong coupling range to two Majorana fermions shows a pronounced extinction for $t = 1$ ($\delta I_K = 0$ presents yellow line in Figure 26a, and dark cyan curve in 26b). The mechanism for changing the sign is identical to the CNTQD-1TSC system. For $E_d = -1.5$ (green line in Fig. 26b), we observe three characteristic values of δI_K : 0.33 for the quartets $|p_{ls}\rangle_4$ (this corresponds to the $SU(4)$ Kondo symmetry), $\delta I_K = 0.16$ for $|q_a\rangle_{16}$ and $|q_z\rangle_4$. It is interesting to note that for $\delta I_K = 1/3$ and $\delta S_K = 1/10$ the Fano factor is equal to $1/3$, which is similar to the result for Dirac fermions. The analogy of these systems derives from the bispinor of the Dirac fermion state and the spin-orbital $SU(4)$ Kondo state with one electron in the system. In δI_k we observe the boost of the current between the configuration change from $|q_a\rangle_{16}$ to the quartet states $|q_z\rangle_4$ (green line in Fig. 26b). For $E_d = -3$, the current with increasing the coupling strength t is quantized to: $\delta I_K = 0.5, 0.3$ and 0.07 at the boundaries of areas with different charge numbers on the dot. For $Q = 2e$ (i.e. $E_d = E_{e-h}$, red line in Fig. 26b), the current takes on values: $\delta I_K = 0.89$ for the sextuplets $|d_w\rangle_6$ ($SU(4)$ Kondo symmetry), $\delta I_K = 0.51$ for $|q_w\rangle_{24}$ and $\delta I_K = 1$ in the region of strong coupling strength, where the octuplet $|q_y\rangle_8$ determines the $SU^*(2)$ Kondo phase (red line in Fig. 26b, and the black area in Fig. 26a).

Figures 26c, d present the nonlinear shot noise δS_K versus E_d and t . δS_K has double zero points for $E_d = +1$, where we observe the sign reversal of the shot noise ($\delta S_K < 0$). The δS_K for $E_d = +1$ in the weak and strong coupling range reaches a value of $\delta S_K = 0.14$ for the quartet states $|q_z\rangle_4$ (dark cyan curve in Fig. 26d). A pronounced suppression of the shot noise ($\delta S_K = 0$) occurs for the two coupling strength values $t = 0.3$ and $t = 2.7$ (yellow line in Fig. 26c, and dark cyan curve in Fig. 26d). At these points, the transport is noiseless, which can be very attractive for quantum measurements. For $E_d = -1.5$ (green line in Fig. 26d), we observe a constant value of $\delta S_K = 0.11$ for $|p_{ls}\rangle_4$ and $|q_a\rangle_{16}$, in contrast to δI_K where the transition is detectable. With increasing the coupling t , the shot noise saturates to 0.14, which corresponds to the quartet state $|q_z\rangle_4$ in the quantum dot. For $E_d = -3$ (blue line in Fig. 26d), the noise leads to three quantized values 0.44, 0.24 and 0.06, which occur at the boundary of the different charge sectors. We observe the noiseless transport at the point $t = 1$ for $E_d = -3$, and for $t > 1$ the shot noise takes on a nega-

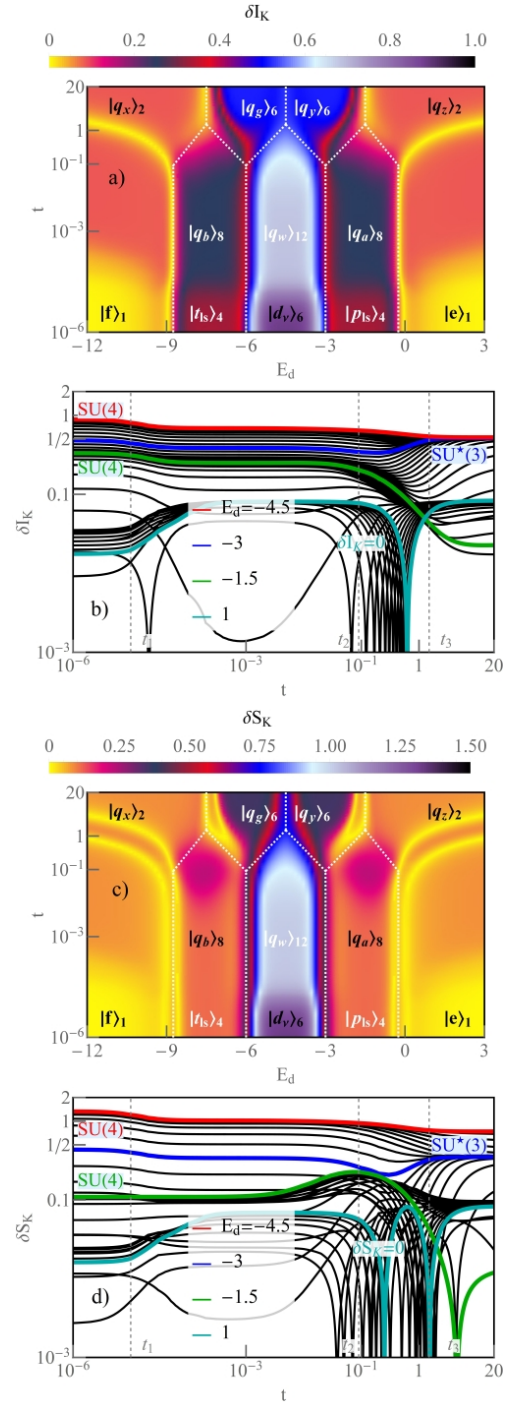


FIG. 25. (Color online) CNTQD-TSC device: a, c) The density plot of the rescaled nonlinear current $\delta I_K = T_{[*]}^2 I_K$ and shot noise $\delta S_K = T_{[*]}^2 S_K$ versus E_d and t . b, d) The landscape log-log plot of δI_K and δS_K as a function of t with increment $\delta E_d = 0.15$. Yellow lines indicate the vanishing of δI_K and δS_K , respectively.

tive value $\delta S_K = -0.06$. For $Q = 2e$ ($E_d = E_{e-h}$, red line in Fig. 26d), the nonlinear noise is quantized to the values: $\delta S_K = 1.33$ for $|d_w\rangle_6$ (the $SU(4)$ Kondo state),

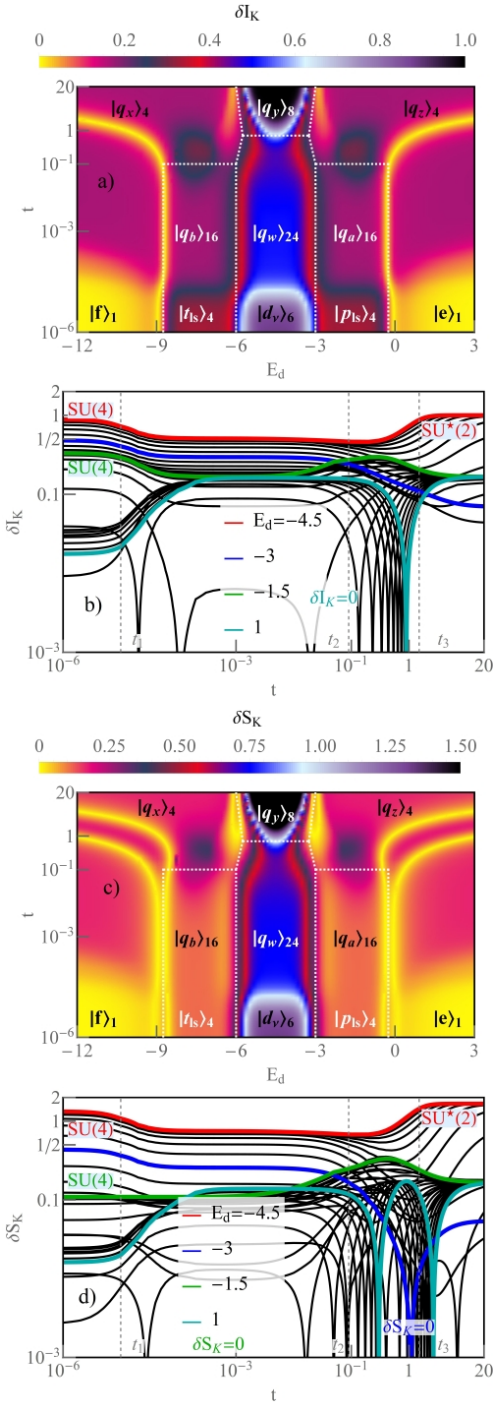


FIG. 26. (Color online) CNTQD-2TSC device: a, c) The density plot of the rescaled nonlinear current δI_K and shot noise δS_K versus E_d and t . b, d) The landscape log-log plot of δI_K and δS_K as a function of t with an increment of $\delta E_d = 0.15$.

$\delta S_K = 0.75$ for $|q_w\rangle_{24}$ and $\delta S_K = 1.65$ in terms of strong coupling strength, where the Kondo $SU^*(2)$ effect is realized by the octuplet $|q_y\rangle_8$ - as the ground state in the system.

Figure 27 shows the δS_K and δI_K for the CNTQD-

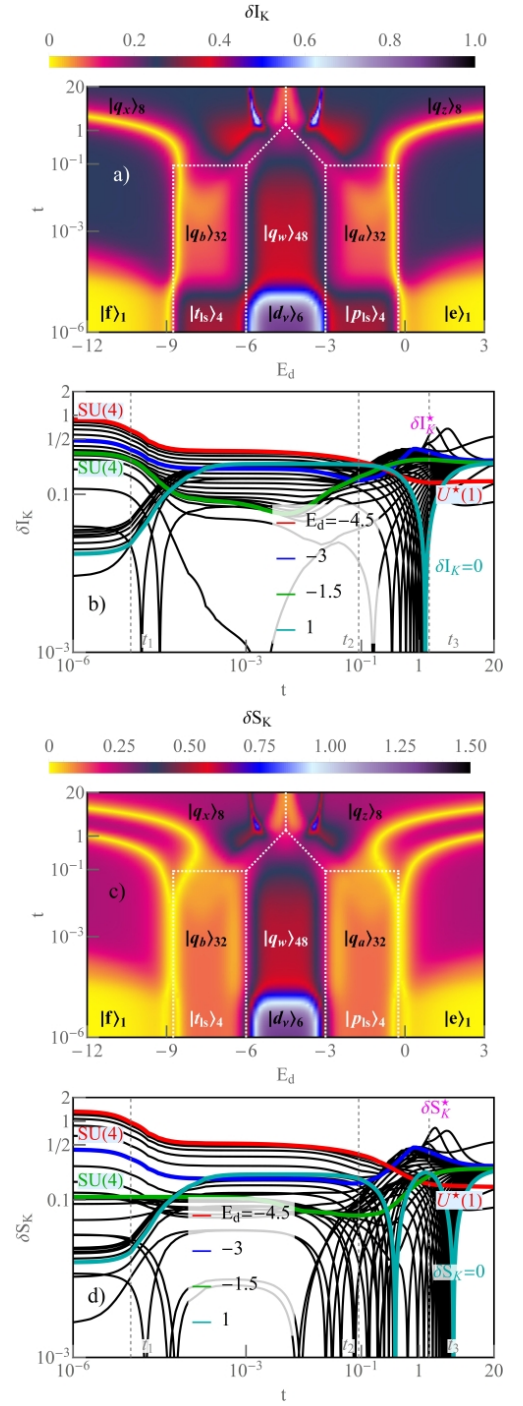


FIG. 27. (Color online) CNTQD-3TSC system: a, c) The density plot of the rescaled nonlinear current δI_K and shot noise δS_K versus E_d and t . b, d) The landscape log-log plot of δI_K and δS_K as a function of t with increment $\delta E_d = 0.15$.

3TSC system. For $t = 0$, the Kondo effect with $SU(4)$ symmetry is realized in the system and δS_K and δI_K are identical to the previously presented numbers. In the weak and strong coupling regime to the TSC for $E_d = +1$ δI_K reaches $1/4$ for the octuplet state $|q_z\rangle_8$

(dark cyan line in Fig. 27b). The sign reversal appears above $t = 1.3$ for $E_d = +1$, but as we can see from Figure 27a, the suppression effect depends on the atomic level of the quantum dot E_d and the coupling strength to the TSC (yellow line shows $\delta I_K = 0$). For $E_d = -1.5$ (green line in Fig. 27b) in the weak coupling regime, we observe a value of $\delta I_K = 0.08$ for $|q_a\rangle_{32}$ with saturation in the strong coupling strength range up to a value of $\delta I_K = 0.25$ for $|q_z\rangle_8$. For $E_d = -3$, we observe three values of the current with increasing the coupling t : $\delta I_K = 0.5, 0.21$ and 0.27 . The $\delta I_K = 0.21$ appears at the boundary of the regions with different charge numbers on the quantum dot (between $|q_w\rangle_{48}$ and $|q_a\rangle_{32}$). In the strong coupling region there is an increase in the nonlinear current, labeled δI_K^* in Figure 27b, where the quantum state $|q_z\rangle_8$ is close enough to the e-h symmetry point to enhance the current by the entanglement mechanism with opposite charge-leaking states. This is closely related to the quantum states marked in red in Eqs. (13-14). The state $|2 \uparrow n_1 n_2 n_3\rangle$ is entangled with states below the e-h symmetry point (from a different charge region). The identical situation occurs on the other side of the e-h symmetry point, for the octuplet $|q_x\rangle_8$. In this case, the state $|0 \downarrow n_1 n_2 n_3\rangle$ in Eq. (14) is responsible for the charge leakage effect. This seems to be the first report in the literature that indicates such a mechanism, and at the same time suggests the possibility of verifying with the lock-in technique in the noise measurement. To emphasize this result, let us call this shogun helmet-like state. For $Q = 2e$ (i.e. $E_d = E_{e-h}$, red line in Fig. 27b), the current takes on the values: $\delta I_K = 0.89$ for the states $|d_w\rangle_6$ (the Kondo state with SU(4) symmetry), $\delta I_K = 0.35$ for $|q_w\rangle_{48}$ and $\delta I_K = 0.5$ in the range of strong coupling t at the e-h symmetry point where the octuplet states degenerate: $|q_x\rangle_8$ and $|q_z\rangle_8$ (red line in Fig. 27b, and the shogun helmet-like state in Fig. 27a). Figures 27c, d show the nonlinear shot noise δS_K , which is rescaled by the characteristic energy $T_{[*]}$ for a CNTQD system coupled to three Majorana fermions. For $E_d = +1$, δS_K (dark cyan curve at 27d) has double zeros. The $\delta S_K = 0$ appears for two coupling values $t = 0.4$ and $t = 4$ (yellow line in Figure 27c, and dark cyan curve in Figure 27d). Between these points δS_K is negative. The δS_K for $E_d = +1$, in the range of the weak and strong coupling strength takes the value around 0.25, when the ground state is determined by the octuplet $|q_z\rangle_8$. For $E_d = -1.5$ (the green line in Fig. 27d) we observe a constant value of $\delta S_K = 0.11$ for $|p_{ls}\rangle_4$ and $|q_a\rangle_{32}$. As the coupling strength increases, the shot noise saturates to $\delta S_K = 0.25$, which corresponds to the octuplet $|q_z\rangle_8$ as the ground state energy. For $E_d = -3$ the noise reaches three quantized values of 0.44, 0.19 and 0.25 (blue line in Fig. 27d), which occur at the boundary of the different charge sectors. At the the shogun helmet-like point there is an increase in shot noise to a maximum value denoted by δS_K^* in Fig. 27d. This is also related to the mechanism of entanglement with opposite charge-leaking states. For $Q = 2e$ ($E_d = E_{e-h}$, red line in Fig. 27d), the noise takes

on the values: $\delta S_K = 1.33$ for the $|d_\nu\rangle_6$, $\delta S_K = 0.52$ for the quantum state $|q_w\rangle_{48}$ and $\delta S_K = 0.15$ in the strong coupling regime for the $U^*(1)$ charge symmetry phase at the e-h symmetry point.

The analyzed quantity in the quantum transport measurements is the nonlinear Fano factor $F_K = \delta S_K / 2e\delta I_K = e^*/e$, whose value different from 1, indicates for the influence of the residual interaction $\tilde{U}_{\nu\nu'}$ between the quasiparticles. The main factors affecting these values are the second and third order fluctuations observed in the current δI_K and in the shot noise δS_K . Figures 28, show the density plots of the nonlinear Fano factor as a function of the quantum dot level energy and the coupling strength to the topological superconductor. Figure 28a, shows F_K for the CNTQD-1TSC model, in the density plot we observe bright areas resulting from the blocked current $\delta I_K = 0$, with a non-zero negative shot noise value $\delta S_K < 0$. On these lines, F_K has an asymptotic behavior. In the density plot, we also see regions where the transport is noiseless $F_K = 0$ (black colored lines). This occurs at the boundary between $|q_a\rangle_8$ and $|q_z\rangle_2$ and between $|q_y\rangle_6$ and $|q_z\rangle_2$, where $\delta S_K = 0$ and $\delta I_K > 0$. Similar behavior was observed in the results of the NRG method [33]. It is definitely not the effect of the absence of the higher order corrections in the coefficients at V^5 , since these contributions are insignificant below the Kondo energy scale, where current and shot noise are described by the Fermi liquid theory assumptions and the vertex corrections for the current-current correlation. Could quaternary and higher-order fluctuations affect the values of the coefficients $c_{V,\nu}$ and $c_{S,\nu}$? This is difficult to answer unambiguously, the authors in [56] have limited themselves to two- and three-particle correlations, pointing to low-energy excitation as the mechanism of the Kondo phase. The zeroing of F_K also occurs for a single quantum dot in the Kondo state (we have only four states there $\{0, \uparrow, \downarrow, 2\}$), where is difficult to imagine fourth-order dot correlators, which says something about the physical implications of this behavior.

Figure 28a illustrates the characteristic values of F_K in the density plot for the CNTQD-1TSC device. For SU(4) Kondo state, (a result known from the literature [33, 51]), as t approaches 0 we observe $F_K = 3/2$ for $Q = 2e$ and ($|d_\nu\rangle_6$) $F_K = 0.33$ for $Q = 1e$ ($|p_{ls}\rangle_4$). For the empty and fully occupied states the Fano factor reaches $F_K = 1$ and is negative $F_K = \frac{S_K}{(2eI_K)} = -1$ for the doublet state $|q_z\rangle_2$. In the weak coupling regime the device demonstrates $F_K = 3/2$ for $|q_w\rangle_{12}$ and $F_K = 0.11/0.25 \approx 0.44$ for the octuplet quantum states $|q_{a(b)}\rangle_8$. For the SU*(3) Kondo state, the Fano factor reaches 0.62. The influence of the Majorana fermion-coupled channel $\nu' = +\uparrow$ is negligible, and the result is consistent with the SU(3) Kondo state. In a sense this is understandable due to the fact that the residual interaction occurs only between the Kondo quasiparticles. Majorana fermions do not interact with each other (they are only represented by two states $\{0, \uparrow\}$). The interaction between the Majorana fermions

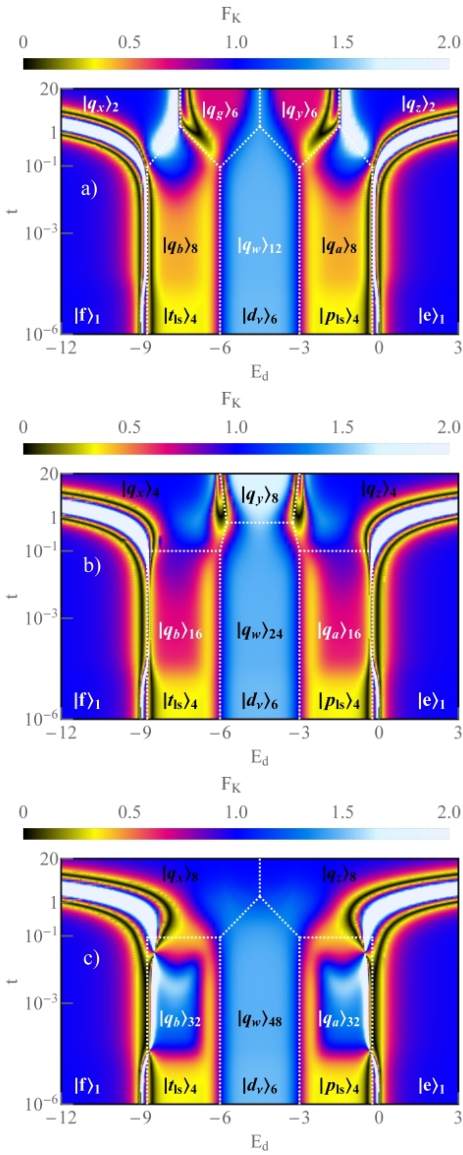


FIG. 28. (Color online) a-c) The density plot of the fractional nonlinear Fano factor $F_K = |c_S|/|c_V|$ versus E_d and t for the CNTQD-TSC, CNTQD-2TSC and CNTQD-3TSC devices. Black and white lines correspond to $S_K = 0$ and $I_K = 0$ respectively.

analyzes the authors in this papers [108, 109] and based on the concept of Wilson ratio, the type of interaction can be relevant for F_K . At the level of the linear regime of the current and the shot noise F_0 is equal to $1/2$ in the channel coupled to the Majorana fermion state, in the nonlinear regime of bias voltage, it is probably insignificant [119]. However, there is a paper [146] where the author suggests for QD-TSC device with the infinite U on quantum dot, $F_K = 3/2$ in the high voltage regime for $t > V > E_d \ll 0$ [146], beyond the Kondo regime ($V \gg T_K$).

Figure 28b shows the density plot of F_K as a function of E_d and the coupling strength t for the CNTQD-2TSC

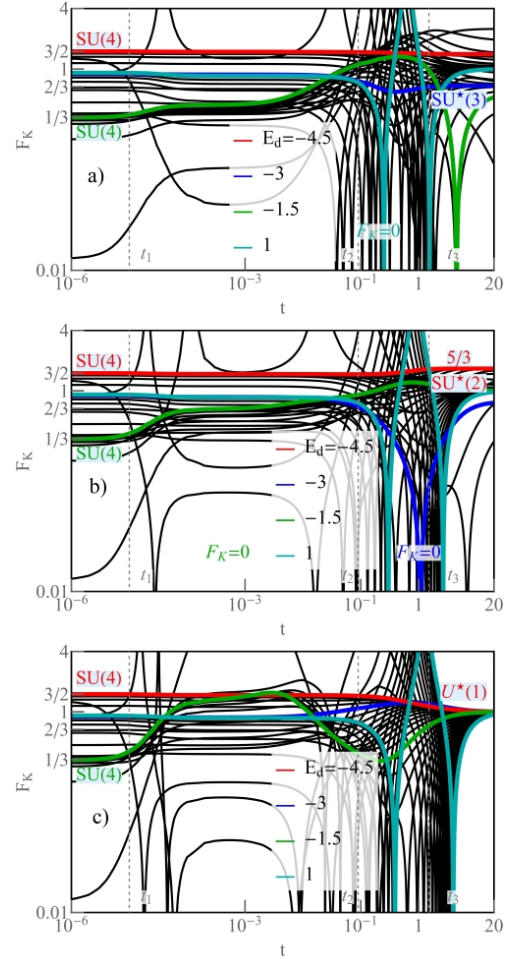


FIG. 29. (Color online) a-c) The landscape log-log plots of F_K as a function of t with increment $\delta E_d = 0.15$ for the CNTQD coupled with MF, 2MFs, and 3MFs.

system. The $SU^*(2)$ Kondo effect arises in the strong coupling region for $Q = 2e$. In this region $F_K = 5/3$ and the channels associated with $SU^*(2)$ Kondo effect play a significant role in the nonlinear shot noise and current (Fig. 26). The fractional super-Poissonian Fano factor is identical to the prediction for the $SU(2)$ Kondo state[59] and the experimental results [149]. Majorana channels in the strong coupling limit remain inactive in the nonlinear voltage regime. In the strong coupling limit, the channels coupled to the TSC contribute only to the linear Fano factor (see Fig. 23b). In the weak coupling limit, the ground state is represented by $|q_w\rangle_{24}$ and $|q_{a(b)}\rangle_{16}$. For this quantum state, Majorana fermions modify the value of the Fano coefficient for $Q = 1(3)e$ from $1/3$ to $F_K \approx 2/3$ (green line in Fig. 29b). Super-Poissonian values of F_K occur at the boundary of the states $|q_{x(z)}\rangle_4$ and $|q_{a(b)}\rangle_{16}$. Noiseless transport ($\delta S_K = 0$) is represented by the black lines in the density plot of the nonlinear Fano factor. $F_K = 0$ is realized at the boundary of the octuplet $|q_y\rangle_8$ and the two quartets $|q_{x(z)}\rangle_4$, and around the transition between $|q_{x(z)}\rangle_4$ and $|q_{a(b)}\rangle_{16}$.

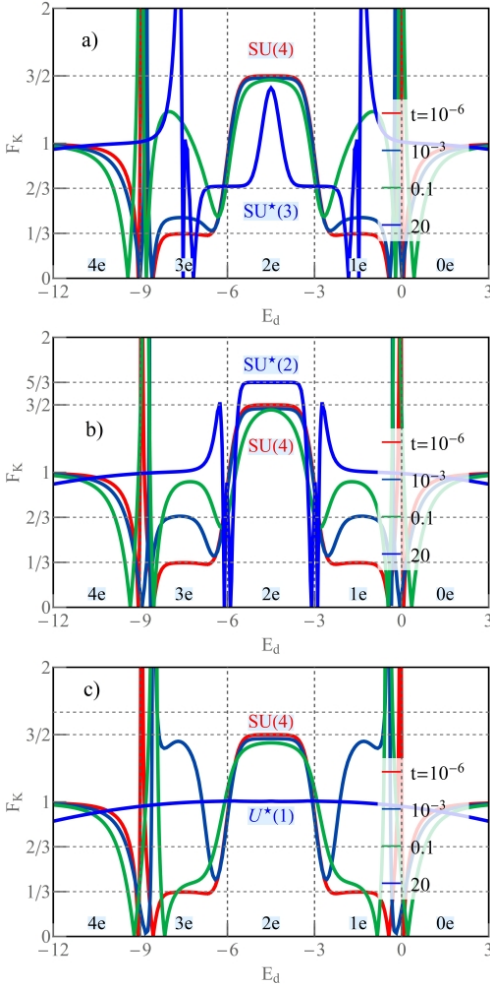


FIG. 30. (Color online) a-c) E_d dependence of F_K with increasing t for CNTQD-TSC, CNTQD-2TSC and CNTQD-3TSC devices. Dashed vertical and horizontal lines divide the charge regions $Q = 0e, 1e, 2e, 3e, 4e$ and show characteristic limits of F_K .

Fig. 28c illustrates F_K as a function of E_d and the coupling strength t for the CNTQD-3TSC hybrid device. In terms of the weak coupling to three Majorana fermion states, we observe an SU(4) Kondo-like effect, with a ground state $|q_{a(b)}\rangle_{32}$ in the charge regions $Q = 1(3)e$. The F_K in this area reaches $F_K \approx 1.33$ (the light blue region in Fig. 28c). The F_K shows the difference between the fully SU(4) Kondo phase and the SU(4) Kondo-like state. For $Q = 2e$, the area is determined by the quantum state $|q_w\rangle_{48}$, and F_K approaches the quantized value $F_K = 3/2$, which corresponds to the result for the SU(4) Kondo effect. The variability of δS_K and δI_K is intersected as a red curves in Fig. 26b,d. The role of the Majorana fermion is significant in the current and the shot-noise, even if $F_K = |S_K|/2e|I_K| = 3/2$ with increasing t , is constant and does not depend on the coupling strength t in terms of weak coupling to the TSC. In both magnitudes S_K and I_K , the mechanism of entanglement

with opposite charge-leaking states is evident, but in F_K the mechanism is practically invisible, due to the comparable values of I_K with S_K . In Fig. 28c, black lines present noiseless transport, where $\delta S_K = 0$ and the white areas represent the blocked transport for $\delta I_K = 0$.

Figure 29 shows the cross sections of F_K as a function of t with the increment $\delta E_d = 0.15$ in the range E_d from -12 to 3 . Figure 29 a-c presents $F_K = 1$ for $E_d = +1$ in the weak coupling regime to TSC (dark cyan lines). In the intermediate region, between t_2 and t_3 , we observe a sign reversal in δS_K , leading to an extinction of F_K at two characteristic points. Significantly, for $t > t_3$, S_K becomes positive again, however I_K has a negative value in the strong coupling regime. We can say that the quasiparticles reverse the flow of the current. This is due to the two-body correlations in δI_K . The red line shows $F_K = 3/2$ for $Q = 2e$ and the green line reaches a value of $F_K = 1/3$ in the weak coupling regime [55, 59]. For the octuplet $|q_a\rangle_8$, we observe $F_K \approx 0.44$ with a small increase of the Fano factor around t_2 to the quantized value $F_K = 3/2$. Above t_3 , there is point of the noiseless transport and F_K saturates with increasing t to the value $F_K = -1/2$ (green line Fig. 29a). For the sextuplet $|q_y\rangle_6$, a fractional effect is realized in the strong coupling regime to the TSC. The SU*(3) Kondo state is formed and F_K reaches 0.62 (blue line Fig. 29a). In Fig. 29b and Fig. 29c for $E_d = -4.5$ we observe the Kondo effect with the SU*(2) symmetry and a charge-degenerate state with U*(1) symmetry (between two octuplets $|q_x\rangle_8$ and $|q_z\rangle_8$). In terms of strong coupling strength, F_K leads to values of $5/3$ and 1 , respectively. Of note is the fact that, for the CNTQD-3TSC system, for the states of $|q_a\rangle_{32}$, we observe a boost of the Fano factor to the value of $F_K \approx 3/2$, which formally occurred for the case of full SU(4) symmetry at the half-filling (green line in Fig. 29c).

Figures 30 include the cross sections of F_K as a function of E_d for the uncoupled, intermediate and strong coupling regimes to the TSC. Fig. 30a shows the gate-dependent F_K for a CNTQD system coupled to a single Majorana fermion $\gamma_{+\uparrow}$. The plot shows the absolute value of the Fano factor, there are regions where $F_K < 0$, preceded by the noiseless points ($F_K = 0$), as we have written, this is due to the dominance of two-body processes over three-particle correlators. For $t = 10^{-6}$, the system is in the SU(4) Kondo state, and F_K assumes two characteristic numbers: $F_K = 3/2$ for $Q = 2e$ and $F_K = 1/3$ for $Q = 1(3)e$. At the transition between the charges $Q = 0(4)e$ and $Q = 1(3)e$, we observe the suppression of the shot noise in two points with super-Poissonian behavior in the middle, when $\delta I_K = 0$. In terms of weak coupling, there is a modification of F_K (green line for $t = 0.1$ in Fig. 30a), F_K is close to $3/2$ for $Q = 2e$ ($|q_w\rangle_{12}$) and increases to $\approx 5/4$ for $Q = 1(3)e$. In $Q = 1(3)e$, the value varies from sub- to super-Poissonian noise with increasing the coupling strength ($\delta I_K > \delta S_K \mapsto \delta I_K \ll \delta S_K$). For the strong coupling limit, we observe two contrasting behaviors around the U*(1) charge symmetry line, where $F_K = 0$ and

$F_K \mapsto +\infty$ (black and white lines in Fig. 28a).

Figure 30b shows the cross sections of F_K corresponding to the density plot of Fig. 28b for $t = 10^{-6}$, 0.1, 10^{-3} and 20. In the figure, we observe a gradual change of F_K from the full SU(4) Kondo effect through the intermediate crossover region ($|q_a\rangle_{16}$) to the strong coupling solution for the quartet $|q_z\rangle_4$. For $t = 0.1$, the value of the δI_K and δS_K at the transition between the states $|q_{a(b)}\rangle_{16}$ and $|q_{z(x)}\rangle_4$ shows an asymptotic maximum and between $|q_{a(b)}\rangle_{16}$ and $|q_w\rangle_{24}$ leads to minimum $F_K = 1/3$ (green line Fig. 29 b). In the strong coupling regime F_K changes its sign to -1 . For the quantum state $|q_{a(b)}\rangle_{16}$, the value of F_K approaches to $2/3$ (dark blue line Fig. 29b). For two electrons on the quantum dot F_K evolves from $2/3$ to a quantized value of $5/3$ for the SU*(2) Kondo state. Although $F_K = 5/3$, as for the full SU(2) Kondo effect [59], we denote the state by \star because the strongly correlated state appears for an even number of electrons $Q = 2e$. The full SU(2) Kondo state is observed for $Q = 1e$. Below $E_d = -6$ and above $E_d = -3$, where $Q = 3e$ and $Q = 1e$, the ground state is defined by two quadruplets $|q_{x(z)}\rangle_4$, $F_K = -1$ and the reverse current $\delta I_K < 0$ dominates in the nonlinear transport (blue line in Fig. 29b).

Fig. 30c shows the cross sections of F_K from Fig. 28c for $t = 10^{-6}$, 0.1, 10^{-3} and 20. The F_K evolve from the full SU(4) Kondo state and reconstructs via the crossover region ($|q_a\rangle_{32}$) to the stable U*(1) charge phase in the range of the strong coupling strength ($|q_z\rangle_8$). Two transition points are observed for $t = 10^{-3}$: the first one at the boundary between $|q_{a(b)}\rangle_{32}$ and $|q_{z(x)}\rangle_8$ shows a maximum and the second one between $|q_{a(b)}\rangle_{32}$ and $|q_w\rangle_{48}$ reaches a minimum close to $1/3$ (dark blue line in Fig. 29c). For half filling and $Q = 1(3)e$ F_K approaches to $3/2$ for $|q_w\rangle_{48}$ and $|q_{a(b)}\rangle_{32}$ (dark blue line Fig. 29c). With increasing the coupling strength, F_K reaches $1/3$ at t_2 and approaches to -1 in the broad region of E_d , in particular for U*(1) charge symmetry point. A line of degeneracy appears for $Q = 2e$ between the fractional charges $Q = 5/2e$ and $Q = 3/2e$, therefore we denote this state by \star (blue line in Fig. 29c). The quantum conductance at this point leads to $\mathcal{G} = (5/2)(e^2/h)$ and is negatively spin (orbital) polarized $\Delta\mathcal{G}_{s(o)} = -1/5$ (Fig. 7a and Fig. 8c). This corresponds to the result for the QD-TSC device [141], where the quantum conductance in the strong coupling regime is narrowed to the e-h symmetry line and reaches the value $\mathcal{G} = (3/2)(e^2/h)$.

E. SOI and transport properties in CNTQD-1TSC device

In the last subsection we will discuss the effect of the spin-orbit interaction (Δ) on the transport quantities in the CNTQD-TSC hybrid system. The SOI in the CNTQD originates from the curvature of the nanotube and reaches the values ranging from thousands to a few meV [2, 8, 36, 44]. The Δ removes the fourfold degeneracy of

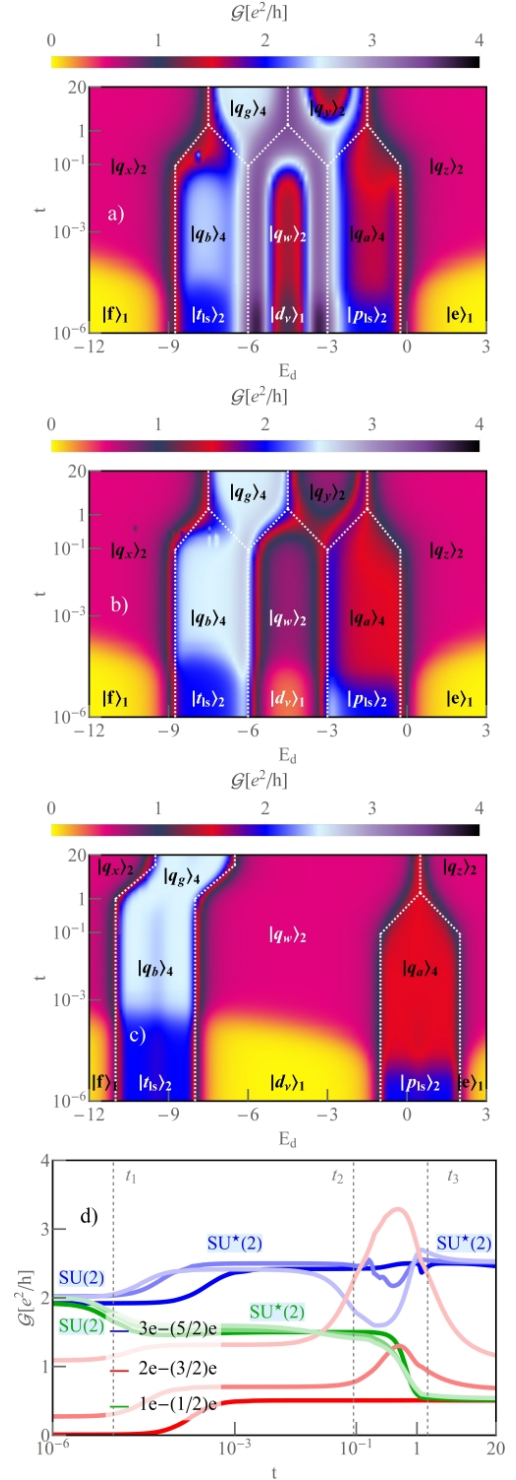


FIG. 31. (Color online) CNTQD-MF device with spin-orbit interaction Δ : a-c) The density plot of \mathcal{G} versus E_d and t for $\Delta = 10^{-2}$, 10^{-1} and 2. d) \mathcal{G} as a function of t . Brightest, light and dark color of the lines show the results for weak, intermediate and strong SOI.

the states on the quantum dot, and forms two Kramers doublets: a low energy doublet $E_{+\downarrow} = E_{-\uparrow}$ and a high

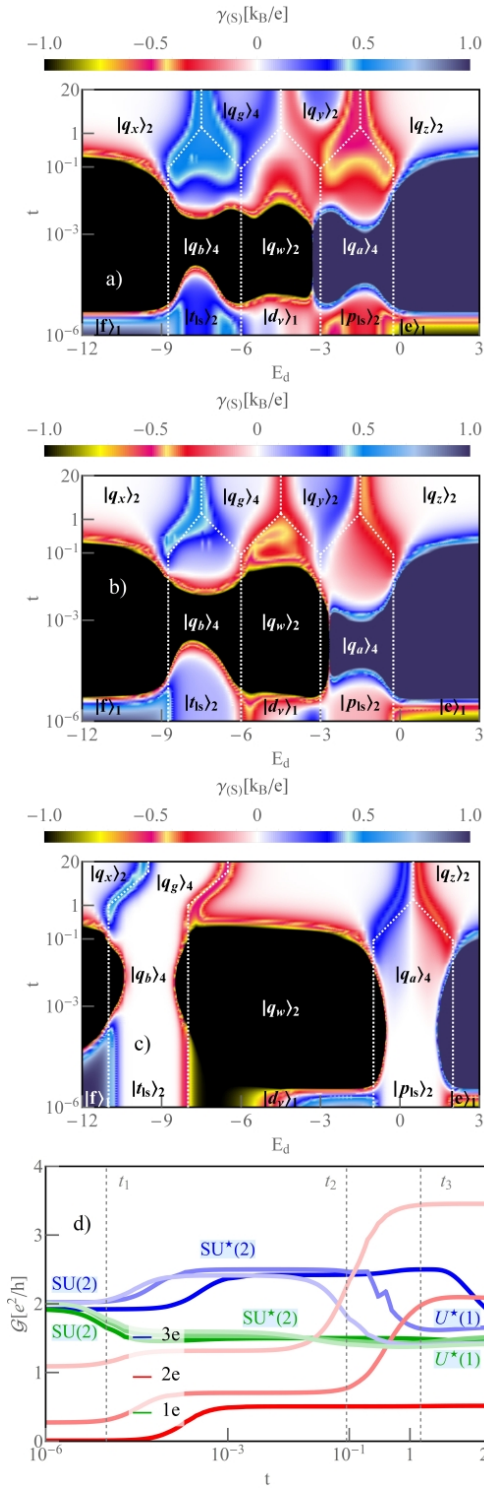


FIG. 32. (Color online) a-c) The density plot of $\gamma_{(S)}$ versus E_d and t for $\Delta = 10^{-2}, 10^{-1}$ and 2. d) \mathcal{G} as a function of t . Brightest, light and dark color of the lines show the results for weak, intermediate and strong SOI.

energy doublet $E_{+\uparrow} = E_{-\downarrow}$. The $SU(4)$ Kondo state is broken by SOI and we observe the Kondo effect with $SU(2)$ symmetry [40, 42, 43]. When we connect the quan-

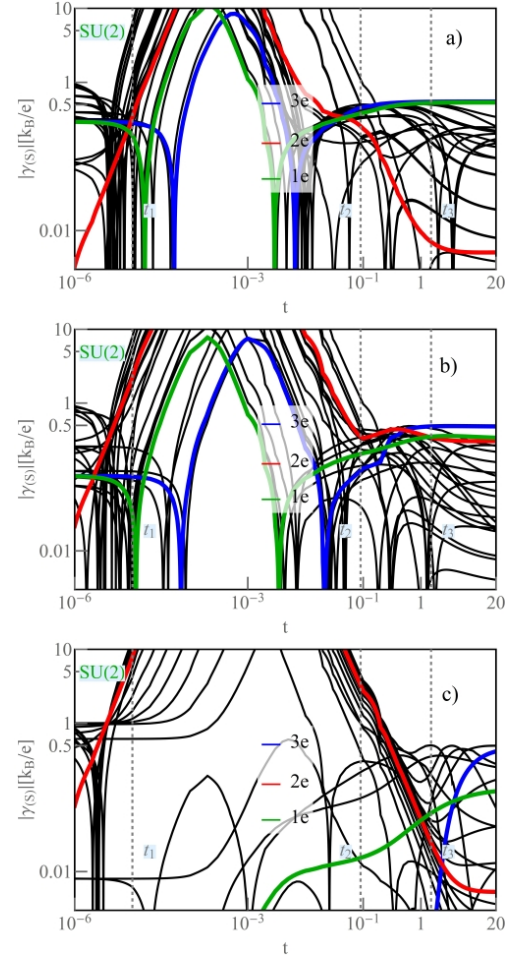


FIG. 33. (Color online) a-c) The landscape log-log plots of $|\gamma_{(S)}|$ as a function of t for weak, intermediate, and strong SOI. The lines are plotted with an increment of $\delta E_d = 0.5$ from -10 to 0.5 .

tum dot to a Majorana fermion of type $\gamma_{+\uparrow}$, one of the channels from the high-energy doublet, is operated by a topological superconductor. The other low-energy doublet is not directly connected to the topological state, but is indirectly capacitively coupled to the $\nu' = +\uparrow$ state through the Coulomb interactions. Figure 31 shows the quantum conductance maps of \mathcal{G} for the weak SOI $\Delta = 10^{-2}$ (a), intermediate $\Delta = 10^{-1}$ (b) and for the strong spin-orbital interaction $\Delta = 2$ ($\Delta \approx U$) (c) [2, 44]. Coupling with 1TSC changes the ground state configuration in the system. For $Q = 1e$, with increasing Δ there is a transition from the quartet $|p_{ls}\rangle_4$ to the doublet $|p_{ls}\rangle_2$, in the weak coupling regime from the octuplet $|q_a\rangle_8$ to the quadruplet $|q_a\rangle_4$ and in the strong coupling range the $U^*(1)$ charge symmetry phase is realized for two doublet states $|q_y\rangle_2$ and $|q_z\rangle_2$. It is noteworthy that for large SOI the $|q_y\rangle_2$ state is replaced by a lower energy state $|q_w\rangle_2$ for the $Q = 2e$ sector (Fig. 31c). The degenerate line between the two doublets disappears under the influence of Δ (Fig. 31a). This is particularly evident in

Fig. 31d, where the sharp maximum between $|q_w\rangle_2$ and $|q_y\rangle_2$ is gradually suppressed (red curves for $Q = 2e$). For $Q = 1e$ we observe the transitions between three quantum states. The first transition is observed between the doublet $|p_{ls}\rangle_2$ and the quadruplet state $|q_a\rangle_4$ and the conductance changes from $\mathcal{G} = 2(e^2/h)$ to $\mathcal{G} = (3/2)(e^2/h)$. Finally, for the strong coupling strength, the quantum conductance $\mathcal{G} = (1/2)(e^2/h)$ determines the doublet state $|q_z\rangle_2$. However, in $|q_z\rangle_2$, the charge is reduced to $Q = (1/2)e$. At the charge degeneracy between the two doublets: $|q_{y(w)}\rangle_2$ and $|q_z\rangle_2$, the system is in the $U^*(1)$ charge state and the conductance reaches the value $\mathcal{G} = (3/2)(e^2/h)$ (green lines in Fig. 32d, and red narrow line in Fig. 31c). This is important, because for $U(1)$ charge symmetry, the quantum conductance always approaches the value of the single quanta (e^2/h).

The most significant result is the asymmetry relation in the quantum conductance, with respect to the e-h symmetry point, between $Q = 1e$ and $Q = 3e$. The reason for the asymmetry is that the high energy is tunnel-coupled to the Majorana fermion state $\gamma_{+\uparrow}$, in contrast to the excited doublet, which is only capacitively coupled to $n_{+\uparrow}$ via the Coulomb interaction. In the weak and strong coupling regime for $Q = 3e-(5/2)e$, the $SU^*(2)$ Kondo states are realized in the presence of Majorana state. The Kondo phases are determined by two quadruplets $|q_b\rangle_4$ and $|q_g\rangle_4$ (blue lines in Fig. 31d). In Fig. 31d, the tunneling term t depends on E_d , using this dependence, we show the quantum conductance for the integer and fractional charges and we pass through the most important ground states of the system (in the contrast to Fig. 32d).

Figures 32-33 show the linear thermoelectric coefficient $\gamma_{(S)}$, defined by Eq. (43) for the CNTQD-1TSC device. In the density plots, we see that for the weak coupling regime, depending on the value of Δ , the thermoelectric power gradually reduces to the full $SU(2)$ Kondo state, where the quasiparticle resonance is centered at the Fermi level, hence $\gamma_{(S)} = 0$ (bright white areas in Fig. 32c for $|t_{ls}\rangle_2$ and $|p_{ls}\rangle_2$ and green and blue lines in Fig. 33c). For $\Delta = 10^{-2}$ and $\Delta = 10^{-1}$, the ground state energy is determined by two doublets $|t_{ls}\rangle_2$ and $|p_{ls}\rangle_2$, however, we observe finite values of $|\gamma_S| \ll \pi/(3\sqrt{2})$, indicating that we are not exactly in the full $SU(2)$ or $SU(4)$ Kondo state. The value of $\gamma_{(S)}$ determines the symmetry and the quality of the Kondo effect.

In the range of intermediate coupling t and $\Delta = 10^{-2}, 10^{-1}$, we observe an enhancement of the thermoelectric power for $|q_{a(b)}\rangle_4$. The system behaves like a non-Fermi liquid in this region, because $T_{[*]}$, does not scale the $\gamma_{(S)}$ to a constant FL number [45]. In Figures 33a, b, we observe the first and second compensation points in γ_S (for $Q = 1e$ and $Q = 3e$). The first zero in Eq. (43) occurs when $-\pi T_K (\cot[\delta_{\nu'}][\tilde{\Gamma}_{\nu'}\delta^2 + \tilde{t}^2\delta])/[(3\tilde{q}_{\nu}(0) + \tilde{q}_{\nu'}(0))(\pi\tilde{\Gamma}_{\nu'}(2\tilde{t}^2 + \tilde{\Gamma}_{\nu'}\delta \csc^2[\delta_{\nu'}])^2)] = -\pi T_K (-\cot[\delta_{\nu'}]\tilde{\Gamma}_{\nu'}\tilde{t}^2)/[(3\tilde{q}_{\nu}(0) + \tilde{q}_{\nu'}(0))(\pi\tilde{\Gamma}_{\nu'}(2\tilde{t}^2 + \tilde{\Gamma}_{\nu'}\delta \csc^2[\delta_{\nu'}])^2)]$. The first compensation point appears near the value of $t_1 = \delta$ (where δ is the lifetime of the Majorana fermion) and is related

to the contribution of the ν' channel. With increasing the coupling strength we then observe a maximum in the channel coupled to the Majorana fermion. The sign of $\gamma_{(S)}$ changes in the intermediate coupling regime. The similar effect of the sign reversal is presented in the paper [114]. The second compensation point is already a result of balancing of the normal contribution, coming from the ν channel, with the contribution from the ν' quantum channel for the condition $-\pi T_K(3\tilde{q}_{\nu}(0))/[(3\tilde{q}_{\nu}(0) + \tilde{q}_{\nu'}(0))] = -\pi T_K(\cot[\delta_{\nu'}][\tilde{\Gamma}_{\nu'}\delta^2 + \tilde{t}^2(\delta - \tilde{\Gamma}_{\nu'})])/[(3\tilde{q}_{\nu}(0) + \tilde{q}_{\nu'}(0))(\pi\tilde{\Gamma}_{\nu'}(2\tilde{t}^2 + \tilde{\Gamma}_{\nu'}\delta \csc^2[\delta_{\nu'}])^2)]$. In the strong coupling regime, we observe in the linear thermoelectric power coefficient a constant value of $\gamma_s \approx \pm(1/2)$ at the boundary between $|q_x\rangle_2$ and $|q_g\rangle_4$ and between $|q_y\rangle_2$ and $|q_z\rangle_2$ (blue, green lines in Fig. 32a-b). The results correspond to the quantum conductances $\mathcal{G} = (3/2)(e^2/h)$ for $Q = 1e$ and $Q = 3e$ (brightest and light green curves in Fig. 32d). In contrast to Fig. 15a, where we have shown the symmetric evolution of the density plot of $\gamma_{(S)}$ in the NFL phase for $\Delta = 10^{-3}$, we observe a significant asymmetry in the NFL state. In terms of weak and intermediate SOI, $\gamma_{(S)}$ is negative for the doublet and quartet states: $|q_w\rangle_2$ and $|q_a\rangle_4$. The sharp switch is observed at the charge degeneracy line between $|q_w\rangle_2$ and $|q_a\rangle_4$. The position of the e-h symmetry line in the NFL phase is perturbed due to the dominant role of the hole states in Eqs. (8-9). For $\Delta = 2$ in the intermediate coupling regime, the regions for $|q_{a(b)}\rangle_4$ are well defined, and we already observe the full $SU^*(2)$ Kondo states, where $\gamma_S = 0$ (flat white areas in Fig. 32c). Interesting was the intersection by the NFL state of the region for the doublet $|q_w\rangle_2$ (the enhancement for $t \approx 10^{-6}$ in Fig. 32c). This suggests that we need a much weaker coupling to remove the NFL phase from the dependence of $\gamma_{(S)}$. The quantum measurements of the thermoelectric power \mathcal{S} give us the information about the quality of the Kondo effect, much more precisely than the linear quantum conductance \mathcal{G} . If we look on the lines in Fig. 31d and Fig. 32d for $Q = 1(3)e$, we observe a small fluctuation of the conductance around $\mathcal{G} = (5/2)(e^2/h)$ and $\mathcal{G} = (3/2)(e^2/h)$, but in γ_S this is a drastic change in character from NFL (green and blue lines in Fig. 33a, b) to FL behavior (green and blue lines in Fig. 33c).

Fig. 34 shows the δI_K as a function of E_d and t for weak (a), intermediate (b) and strong SOI on the quantum dot (c). The yellow lines and the yellow areas in Fig. 34a show the blocked nonlinear transport. The $\delta I_K \approx 0$ occurs for $\Delta = 10^{-2}$ in the region of the charge stability for two doublet quantum states $|q_w\rangle_2$ and $|q_y\rangle_2$. For $\Delta = 0.1$, the zero lines merge into two lines at the charge degeneracy point between even and odd charges (Fig. 34b). For $t = 10^{-6}$, when the system determines two doublets $|t_{ls}\rangle_2$ and $|p_{ls}\rangle_2$, δI_K varies from $1/2$ for $\Delta = 10^{-2}$, via $\delta I_K \approx 0.75$ for $\Delta = 0.1$, to $\delta I_K \approx 1$ for $\Delta = 2$. For the strong SOI, the $SU(2)$ Kondo states on the two quantum doublets are well defined and well separated (black regions in Fig. 34c). In the region of $Q = 1(3)e$ and $\Delta = 0.1, 2$, for the weak tunneling rate, where $t = 10^{-3}$

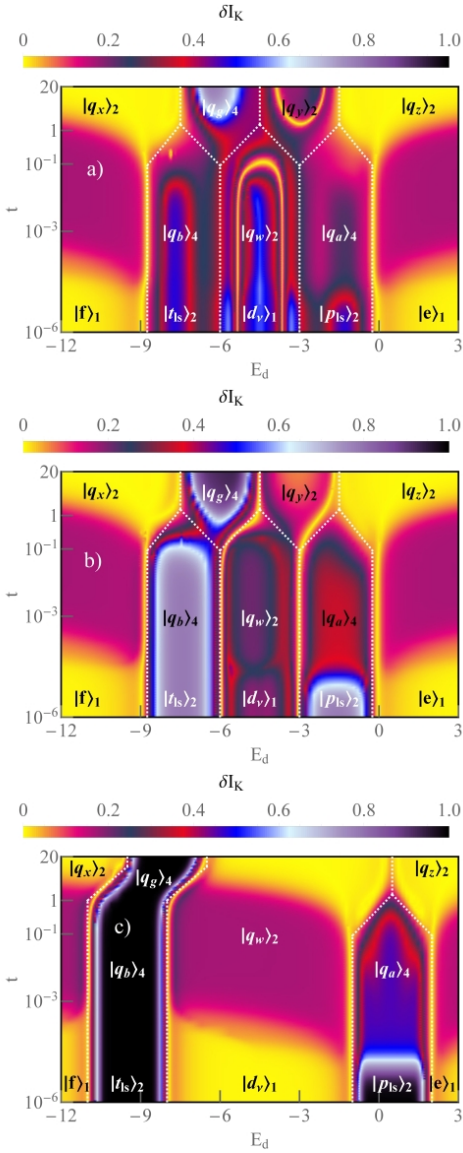


FIG. 34. (Color online) CNTQD-MF device with SOI: a-c) The density plot of the rescaled nonlinear current δI_K versus E_d and t for $\Delta = 10^{-2}$, 10^{-1} and 2.

we observe an asymmetry between the $SU^*(2)$ Kondo effects in two quartet states $|q_b\rangle_4$ and $|q_a\rangle_4$ (Fig. 34b and Fig. 34c). In these domains, the $\delta I_K = T_{[s]}^2 |I_K|$ is quantized to $\delta I_K \approx 1$ for $|q_b\rangle_4$ and $\delta I_K \approx 1/2$ for $|q_a\rangle_4$. For $\Delta = 0.1$, the states are also separated, but the nonlinear currents approach $\delta I_K \approx 0.75$ and 0.35 . The transition between weak and strong coupling strength t is clearly visible in δI_K for the two doublets $|q_{x(z)}\rangle_2$. In these regions, with increasing tunneling strength we observe a change in the value from $\delta I_K = 0.15$ (purple color in Fig. 34a-c) to $\delta I_K = 10^{-3} \approx 0$ (yellow area). In Fig. 25a, for CNTQD without spin-orbit interaction, the quantum states $|q_{x(z)}\rangle_2$ are shared by the yellow line representing $\delta I_K = 0$, where two- and three-body correlators are compared. For the hybrid device with finite

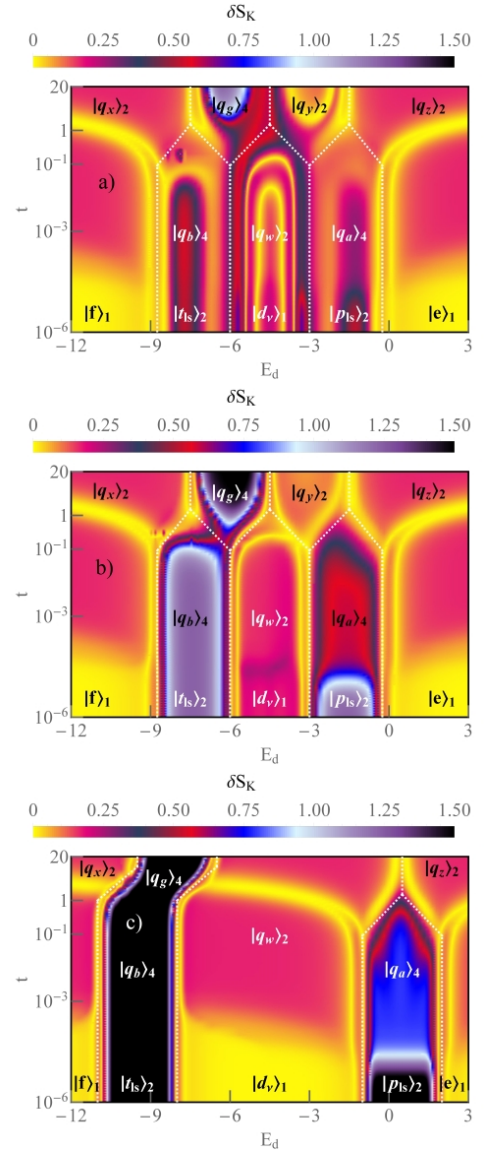


FIG. 35. (Color online) a-c) The density plot of the rescaled nonlinear shot noise δS_K versus E_d and t for weak, intermediate and strong SOI. Yellow lines denote noiseless transport $\delta S_K \approx 0$.

SOI, the line extends into the region with blocked non-linear transport $\delta I_K \approx 0$. The consequence of this effect is the super-Poissonian value of F_K . The transition between the Kondo effect with $SU(2)$ symmetry and the $SU^*(2)$ Kondo state is visible in the current, especially for $Q = 1e$, where $\delta I_K \approx 1$ for $|p_s\rangle_2$ changes to $\delta I_K \approx (1/2)$ for $|q_a\rangle_4$. This is particularly evident, in the high energy doublet, due to the fact that the CNTQD is coupled to $\gamma_{\uparrow\downarrow}$. The interference effects between the topological and quantum dot states, significantly modify the value of the δI_K . The low energy doublet is insensitive to increasing the coupling strength t , in contrast to the quantum conductance (black region in Fig. 34c), which changes from $2(e^2/h)$ to $(5/2)(e^2/h)$ (Fig. 31b, c).

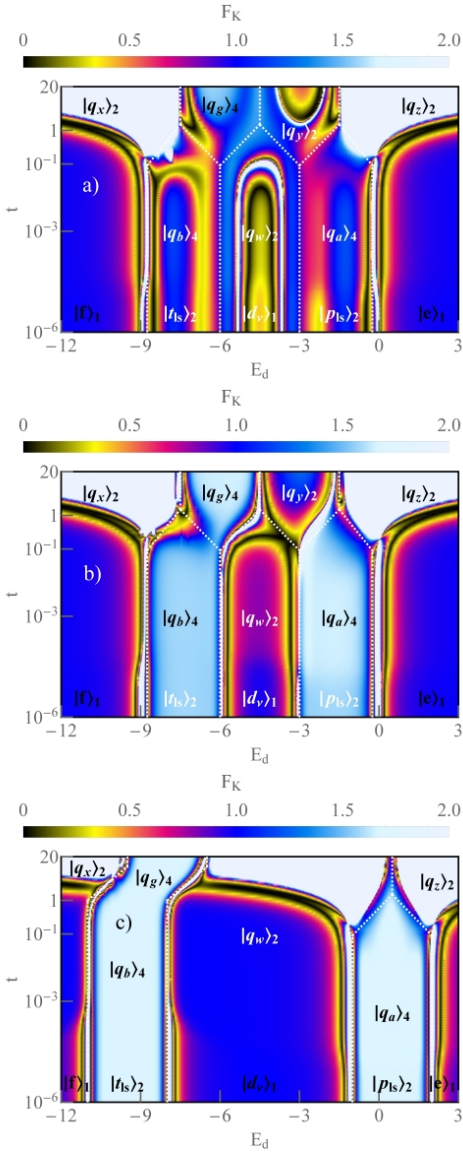


FIG. 36. (Color online) a-c) The density plot of F_K as a function of E_d and t for $\Delta = 10^{-2}, 10^{-1}$ and 2. Black and white lines correspond to $S_K = 0$ and $I_K = 0$.

Figures 35 show the density plots of the nonlinear shot noise $\delta S_K = T_{[x]}^2 |S_K|$ as a function of E_d and t . The yellow lines represent the noiseless transport $\delta S_K \approx 0$. The lines are doubled and between them the noise due to three-particle processes changes the sign $\delta S_K < 0$ (yellow lines in Fig. 35a-c). In Fig. 35b we observe two noiseless lines separating the quantum states $|q_w\rangle_2$ from $|q_y\rangle_2$ and $|q_{a(b)}\rangle_4$ from $|q_{z(x)}\rangle_2$. In the intermediate and strong coupling regime for $|q_{z(x)}\rangle_2$, δS_K reaches a finite value $\delta S_K \approx 0.15$, leading to super-Poissonian behavior of F_K (the bright white area in Fig. 36a-c). The double black lines where $F_K \approx 0$ result from two types of phase shifts in Eq. (39): $2\delta_\nu$ and $4\delta_\nu$. For $\Delta = 10^{-2}$ the noiseless transport occurs in the charge stability regions for two quantum states $|q_w\rangle_2$ and $|q_y\rangle_2$ (Fig. 35a).

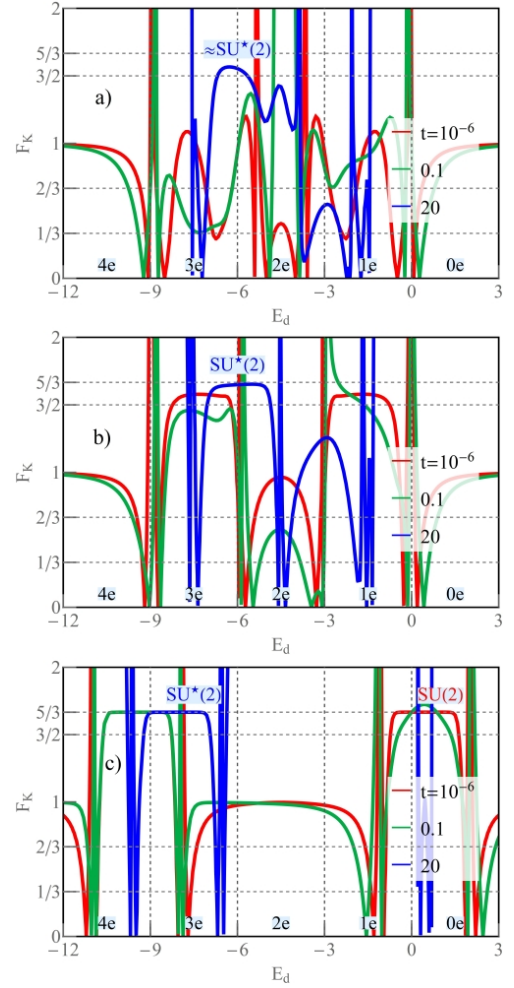


FIG. 37. (Color online) a-c) E_d dependence of F_K with increasing t for weak, intermediate and strong SOI.

With increasing SOI there is a significant asymmetry in δS_K between $Q = 1e$ and $Q = 3e$. In the high energy doublet, due to the coupling strength of the CNTQD to $\gamma_{+\uparrow}$, interference effects of the topological state significantly modify the value of the nonlinear shot noise. For $Q = 1e$, we observe a change of the δS_K for $|p_{l_s}\rangle_2$ and $|q_a\rangle_2$ from 1.25 to 0.55 for $\Delta = 10^{-1}$ and from 1.5 to 0.75 for $\Delta = 2$.

Figure 36 shows the density plots of the evolution of $F_K = \delta S_K / \delta I_K$ in functions E_d and t with increasing SOI in the quantum dot. Fig. 36a shows F_K for $\Delta = 0.01$. In the sector of the doublet states $|q_w\rangle_2$ and $|q_y\rangle_2$ and between $|q_{a(b)}\rangle_4$ and $|q_{z(x)}\rangle_2$, we observe the black lines symbolizing the noiseless transport $\delta S_K \approx 0$, with strong enhancement when $\delta I_K \approx 0$ and the nonlinear transport is blocked (bright white line and regions Fig. 36). For $Q = 1e$ and $Q = 3e$, we observe the partially filled blue region where $F_K \approx 1$ ($\Delta = 0.01$), which is a precursor of the $SU(2)$ and $SU^*(2)$ Kondo states. Figure 36a shows a narrow region for $Q = 1e$ and $Q = 3e$ with $F_K \approx 1/3$, which reveals as a residual of the Kondo state with $SU(4)$

symmetry (Fig. 28a). The asymmetry of F_K manifests itself for the broken $SU^*(3)$ Kondo state, where finite $\Delta = 0.01$ for $Q \approx (5/2)e$ leads to an increase of the shot noise $F_K \approx (5/3)$ ($|q_g\rangle_4$) and for the $Q \approx (3/2)e$ we observe a decrease of the noise $F_K \approx 0.5$ ($|q_y\rangle_2$). The transition from $|q_y\rangle_2$ to $|q_w\rangle_2$ is seen by changing the sign and reducing the nonlinear current δI_K , then F_K reaches $1/2$, via -1 and to the super-Poissonian value $F_K \gg 1$ (Fig. 36).

The cross sections of F_K are shown in Fig. 37a. The blue line in Fig. 37a, for $Q = (5/3)e$ approaches to the value of $F_K = e^*/e \approx (5/3)$ for the $SU^*(2)$ Kondo effect. For $Q = (3/2)e$ and $t = 20$, we observe the reduction of the Fano factor to $F_K = e^*/e \approx 1/2$ (Fig. 37a). In the region, where two doublets $|q_{x(z)}\rangle_2$ dominate, the Fano factor F_K reaches the super-Poissonian values $F_K \gg 1$, which is due to the finite value of the nonlinear shot noise $\delta S_K \approx 0.15$, relative to the value of the current $\delta I_K \approx 10^{-3}$. This behavior persists for the three values of the SOI $\Delta = 0.01, 0.1$ and 2 (the white areas in Fig. 36, and the blue lines in Fig. 37). For $\Delta = 0.1$ and $t = 10^{-6}$, F_K in the region of one and three electrons on the quantum dot is quantized close to $5/3$ for $|p_{l_s}\rangle_2$ and $|t_{l_s}\rangle_2$ states, which is the characteristic fingerprint of the $SU(2)$ Kondo state (red line in Fig. 37b). With increasing the coupling strength t , the e-h symmetry is broken and for $\Delta = 0.1, 2$, the $SU^*(2)$ Kondo state is realized for the quadruplet $|q_g\rangle_4$ (blue curves in Fig. 37c). The high energy doublet evolves to the $U^*(1)$ charge symmetry, where between $|q_w\rangle_2$ and $|q_z\rangle_2$ we observe $F_K = 1$ splitting two super-Poissonian regions.

Figure 38 shows the landscape plots of F_K as a function of t . The black curves are plotted from $E_d = -10$ to $E_d = 1$ with increment $\delta E_d = 0.25$. In Fig. 38a, b for $E_d = -6$ (blue line) and in Fig. 38c for $E_d = -7.5$ (red line), in the strong coupling regime, F_K approaches to $5/3$ for $Q = (5/2)e$, in contrast to $Q = (3/2)e$ ($E_d = -3$, Fig. 38a, c), where $F_K \approx (1/2)$ for $\Delta = 0.01$ and $F_K \approx 1$ for $\Delta = 0.1$. The changes in nonlinear current and shot noise are determined by the doublet quantum state $|q_y\rangle_2$. The coupling term to $\gamma_{+\uparrow}$ and Δ contributes to the asymmetry in F_K between low and high energy doublets. The curve for $E_d = -4.5$ ($Q = 2e$) shows two points of compensation in the Fano factor $F_K = 0$. We observe the noiseless transport for $|q_w\rangle_2$. Between the point of the blocked nonlinear transport, we observe a negative shot noise $\delta S_K < 0$ (red line in Fig. 38a). For $\Delta = 0.1$, two compensation points are reduced to one noiseless point at the boundary of the doublet state (red curve in Fig. 38b). For the quantum state $|q_y\rangle_2$, we observe the asymptotic enhancement of the Fano factor $F_K \gg 1$ (green lines in Fig. 38a). With increasing the SOI, for the intermediate spin-orbit coupling $\Delta = 0.1$, the enhancement of F_K shifts from t_3 to t_1 . At this point we observe the super-Poissonian value of F_K , and the nonlinear current is blocked. For $\Delta = 0.1$, $\delta I_K \approx 0$ appears on the charge degeneracy line between two states $|q_w\rangle_2$ and the quadruplet $|q_a\rangle_4$. With increasing SOI, the super-Poissonian

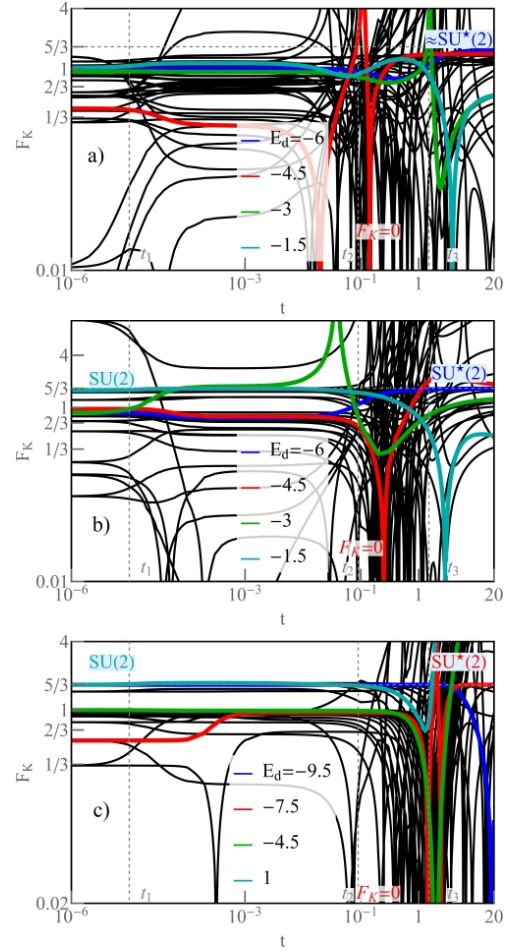


FIG. 38. (Color online) a-c) The landscape log-log plot of F_K as a function of t for $\Delta = 10^{-2}, 10^{-1}$ and 2 . $F_K = 0$ corresponds the noiseless nonlinear transport ($S_K = 0$).

F_K evolves to noiseless transport for $E_d = -4.5$ (green line in Fig. 38c). For $t = 10^{-6}$ and intermediate and strong SOI, the $SU(2)$ Kondo effect is realized by two doublets $|p_{l_s}\rangle_2$ and the Fano factor reaches to the quantized value $F_K = (5/3)$ (dark cyan lines in Fig. 38b, c). With increasing the coupling strength F_K is constant and reaches $5/3$, but the effective charge e^* determines the quartet state $|q_a\rangle_4$. The dynamical changes to super-Poissonian values are observed in the strong coupling regime for $|q_{x(z)}\rangle_2$ and $Q = 2e$, when $|q_w\rangle_2$ is the ground state (green line in Fig. 38c). The enhancement of F_K is preceded by noiseless point around t_3 (black lines in Fig. 36 and green line in Fig. 38c).

Figure 39 shows the nonlinear current, shot noise and Fano factor as a function of the coupling strength t for $\Delta = 2$. The cross sections are drawn from $E_d = 1/2$ to 1.75 and intersect the quartet $|q_a\rangle_4$ for the weak coupling strength to TSC and the doublet $|q_z\rangle_2$ in the strong coupling regime. The curve for $E_d = 2$ is plotted at the boundary of the $|q_a\rangle_4$ and $|q_z\rangle_2$ states. At the charge boundary, $\delta I_K = 0$ and $\delta S_K = 0$ appear for two differ-

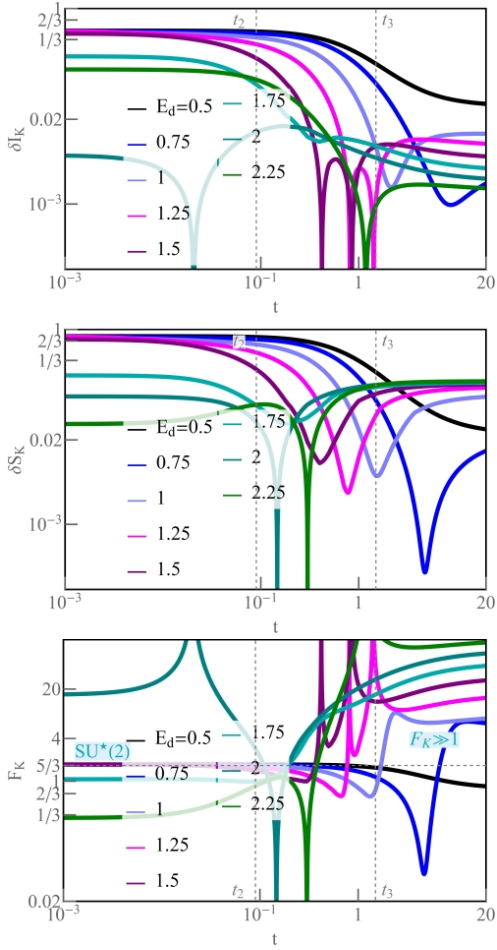


FIG. 39. (Color online) Super-Poissonian F_K : a-c) Gate-dependent δI_K , δS_K and F_K as a function of t ($\Delta = 2$). $F_K \gg 1$ appears for t , where the nonlinear transport is determined by Majorana fermion-coupled channel.

ent values of t , hence we observe the logarithmic divergence of F_K for $t = 10^{-2}$, and noiseless transport near t_2 (darker cyan curve Fig. 39c). For $E_d = 2.25$ the transport is determined by double $|q_z\rangle_2$ and in F_K we observe the opposite tendency, the transport is blocked around t_2 and F_K is logarithmically divergent at t_3 . For weak coupling and in the range between $E_d = 0.5$ and 1.5 , the $SU^*(2)$ Kondo effect is realized (Fig. 38c) and F_K reaches $5/3$. The super-Poissonian F_K results from the blocking effect of the nonlinear current, and the presence of the spin-orbit interaction in the system. The F_K for the doublet states show two types of the behavior: $F_K \approx 1$ for weak coupling strength to the TSC and $F_K \gg 1$ in the strong coupling regime (Fig. 36c). The current and shot noise are modified by the SOI, in particular the contributions of the two- and three-body correlators in the current are compared to each other (Fig. 39a), hence $\delta I_K \approx 0$ we observe the logarithmic divergence of F_K (Fig. 39c). For $E_d = 1.25$ and $E_d = 1.5$ we observe two compensation points, where $\delta I_K = 0$. Between these points the cur-

rent is negative and in the nonlinear regime, the current flows in the opposite direction to the applied voltage (the backward current of the quasiparticles), whereas before this behavior was reserved only for nonlinear noise. The super-Poissonian value of the nonlinear Fano is always accompanied by a sign reversal of the nonlinear current. The calculations require a more detailed analysis in the future. However, it is worth mentioning that the result of the experiment [149], where the authors obtained $F_K = 3$ for the quantum dot system, is also surprising, perhaps the system is not in the full $SU(2)$ Kondo state, and the symmetry is broken by an additional disorder. At the moment it is difficult to explain this with the existing theory.

IV. CONCLUSIONS

In summary, we have studied the transport properties of the novel type of the fractional Kondo effect with $SU^*(3)$ symmetry in the strong coupling regime with 1TSC. For the CNTQD system coupled with two Majorana fermions, we discovered the $SU^*(2)$ Kondo state with an even number of electrons on the quantum dot. The CNTQD-3TSC device showed that a state with charge symmetry $U^*(1)$ determines the quantum conductance $\mathcal{G} = (5/2)(e^2/h)$ in the strong coupling regime. For the octuplets $|q_{x(z)}\rangle_8$ we observed the charge leakage quantum effect. The effect was seen in the high order susceptibilities, nonlinear current and shot noise measurements. For $SU^*(3)$ Kondo phase, the charge fluctuations were finite and led to $\Delta N^2 = 1/4$, which is due to the coexistence of a coupled channel with a Majorana fermion.

In the linear thermoelectric power coefficient, in the range of weak coupling to TSCs, we observed NFL behavior with strong enhancement of the TEP with two compensation points, where $\gamma_{(S)} = 0$. In the range of weak and strong coupling, $\gamma_{(S)}$ led to FL-type behavior and the numbers characterized the Kondo state with full symmetry. The extended KR sbMFA method showed the complementary results to the NRG calculations [54], in particular with respect to the $SU(4)$ Kondo effect. The new type of strongly correlated phases $SU^*(3)$ and $SU^*(2)$ showed $F_K = 2/3$ and $F_K = 5/3$. In this paper, a so-called the weak coupling ansatz is proposed to calculate the Wilson coefficients, and consequently the off-diagonal two- and three-body correlators. Measurements of the linear coefficient of the TEP and the nonlinear Fano factor, in the case of the broken $SU(2)$ Kondo state, by SOI and most likely in the case of arbitrary other perturbations contain the information about the quality of the Kondo effect and its symmetry. The Kondo temperature with increasing coupling to TSCs, at the transition limit between the $SU(2)$ and $SU^*(2)$ showed an enhancement controlled by the Coulomb interaction in CNTQD and by the tunneling rate to the normal electrodes. The total entropy as a function of temperature is

quenched for the Kondo state. For a single electron in the CNTQD-1TSC device, the entropy has reached $\ln[4]/4$, which is closely related to the symmetry of the Kondo effect. By increasing the number of Majorana fermions coupled to the CNTQD, the entropy is raised in the intermediate temperature range to the following numbers $(N_{TS} \ln[4])/4$.

In the tunneling entropy we observed a sign reversal and a negative value, which is characteristic for TSC-coupled systems - indicating strong order. For the $SU^*(3)$ Kondo state, the fluctuations of the pseudospin moment increased with the temperature, and the high temperature limit of the entropy reached to the value of $\ln[3]$, suggesting the threefold degeneracy of the quantum states. The linear Fano effect led to the quantized fractional values. By measuring the linear coefficient of the TEP, we presented the detection of the lifetime of the Majorana fermion state and the moment of the transition from the NFL-like behavior to the FL phase. Hybrid devices with TSC showed the negative spin (orbital) polarization of the quantum conductance. For 1TSC and 3TSC, the spin and orbital polarization are identical in sign and value. Shot noise and current measurements allowed indirect the determination of the pseudospin and charge suscep-

tibilities. The SOI in the CNTQD-1TSC system, due to the formation of two quadruplets, led to an asymmetric behavior in the nonlinear current, shot noise and effective charge. The number of N_{TS} topological sectors was introduced for the entanglement of the quantum states from even and odd charge regions, and the Hilbert space was extended to $2^{n+N_{TS}}$. In the strong coupling regime, for the doublet states as the ground state, we observed super-Poissonian values of the Fano factor, which is related to the damping of the nonlinear current by the SOI in CNTQD. In this paper, we have investigated the transport and correlation properties of the CNTQD system in the Kondo state coupled to a TSC. We have studied the quantum transport quantities such as quantum conductance, thermoelectric power, linear and nonlinear current, and shot noise in a wide range of the coupling term to the topological superconductor. We have shown that CNTQD in the $SU(4)$ Kondo state, can provide a very precise detector of the Majorana bound states, and the residual interaction between the quasiparticles.

Acknowledgements. This work received support from National Science Center in Poland through the research Project No. 2018/31/D/ST3/03965.

-
- [1] S. Sapmaz, P. Jarillo-Herrero, L. P. Kouwenhoven, and H. S. J. van der Zant, Quantum dots in carbon nanotubes, *Semicond. Sci. and Tech.* **21**, S52 (2006).
 - [2] E. A. Laird, F. Kuemmeth, G. A. Steele, K. Grove-Rasmussen, J. Nygård, K. Flensberg, and L. P. Kouwenhoven, Quantum transport in carbon nanotubes, *Rev. Mod. Phys.* **87**, 703 (2015).
 - [3] J. Nygård, D. H. Cobden, and P. E. Lindelof, Kondo physics in carbon nanotubes, *Nature* **408**, 342 (2000).
 - [4] J. D. Schmid, *The Kondo Effect in quantum dots*, Phd thesis, Max-Planck-Institut für Festkörperforschung Stuttgart, Stuttgart, Germany (2000).
 - [5] J. P. Cleuziou, N. V. N'Guyen, S. Florens, and W. Wernsdorfer, Interplay of the Kondo Effect and Strong Spin-Orbit Coupling in Multihole Ultraclean Carbon Nanotubes, *Phys. Rev. Lett.* **111**, 136803 (2013).
 - [6] A. J. Keller, S. Amasha, I. Weymann, C. P. Moca, I. G. Rau, J. A. Katine, H. Shtrikman, G. Zaránd, and D. Goldhaber-Gordon, Emergent $SU(4)$ Kondo physics in a spin-charge-entangled double quantum dot, *Nat. Phys.* **10**, 145 (2014).
 - [7] S. Sasaki, S. De Franceschi, J. M. Elzerman, W. G. van der Wiel, M. Eto, S. Tarucha, and L. P. Kouwenhoven, Kondo effect in an integer-spin quantum dot, *Nature* **405**, 764 (2000).
 - [8] T. S. Jespersen, K. Grove-Rasmussen, J. Paaske, K. Muraki, T. Fujisawa, J. Nygård, and K. Flensberg, Gate-dependent spin-orbit coupling in multielectron carbon nanotubes, *Nat. Phys.* **7**, 348 (2011).
 - [9] J. Kondo, Resistance Minimum in Dilute Magnetic Alloys, *Prog. of Theo. Phys.* **32**, 37 (1964).
 - [10] K. G. Wilson, The renormalization group: Critical phenomena and the Kondo problem, *Rev. Mod. Phys.* **47**, 773 (1975).
 - [11] P. Nozières, A Fermi-liquid description of the Kondo problem at low temperatures, *J. of Low Temp. Phys.* **17**, 31 (1974).
 - [12] F. D. M. Haldane, Scaling Theory of the Asymmetric Anderson Model, *Phys. Rev. Lett.* **40**, 416 (1978).
 - [13] K. Haule, S. Kirchner, J. Kroha, and P. Wölfle, Anderson impurity model at finite Coulomb interaction U : Generalized noncrossing approximation, *Phys. Rev. B* **64**, 155111 (2001).
 - [14] D. R. Hamann, Derivation of Kondo Anomalous Scattering from the Anderson Dilute-Alloy Model, *Phys. Rev.* **154**, 596 (1967).
 - [15] R. Van Roermund, *Theoretical Study of non-equilibrium transport in Kondo quantum dots*, Phd thesis, Université Grenoble Alpes, Grenoble, France (2010).
 - [16] G. Kotliar and A. E. Ruckenstein, New Functional Integral Approach to Strongly Correlated Fermi Systems: The Gutzwiller Approximation as a Saddle Point, *Phys. Rev. Lett.* **57**, 1362 (1986).
 - [17] P. Coleman, *Introduction to Many-Body Physics* (Cambridge University Press, 2015).
 - [18] P. Coleman and N. Andrei, Diagonalisation of the generalised Anderson model, *J. of Phys. C: Sol. Sta. Phys.* **19**, 3211 (1986).
 - [19] P. B. Wiegmann and A. M. Tsel'ick, Exact solution of the Anderson model: I, *J. of Phys. C: Sol. Sta. Phys.* **16**, 2281 (1983).
 - [20] A. Okiji and N. Kawakami, Thermodynamic Properties of the Anderson Model, *Phys. Rev. Lett.* **50**, 1157 (1983).
 - [21] D. Goldhaber-Gordon, H. Shtrikman, D. Mahalu,

- D. Abusch-Magder, U. Meirav, and M. A. Kastner, Kondo effect in a single-electron transistor, *Nature* **391**, 156 (1998).
- [22] W. Liang, M. Bockrath, and H. Park, Shell Filling and Exchange Coupling in Metallic Single-Walled Carbon Nanotubes, *Phys. Rev. Lett.* **88**, 126801 (2002).
- [23] K. Grove-Rasmussen, H. Jørgensen, and P. Lindelof, Fabry-Perot interference, Kondo effect and Coulomb blockade in carbon nanotubes, *Phys. Rev. B* **40**, 92 (2007).
- [24] A. Kurzmann, Y. Kleeorin, C. Tong, R. Garreis, A. Knothe, M. Eich, C. Mittag, C. Gold, F. K. de Vries, K. Watanabe, T. Taniguchi, V. Fal'ko, Y. Meir, T. Ihn, and K. Ensslin, Kondo effect and spin-orbit coupling in graphene quantum dots, *Nat. Commun.* **12**, 6004 (2021).
- [25] W. Liang, M. P. Shores, M. Bockrath, J. R. Long, and H. Park, Kondo resonance in a single-molecule transistor, *Nature* **417**, 725 (2002).
- [26] P. Jarillo-Herrero, J. Kong, H. S. van der Zant, C. Dekker, L. P. Kouwenhoven, and S. De Franceschi, Orbital Kondo effect in carbon nanotubes, *Nature* **434**, 484 (2005).
- [27] A. Makarovski, A. Zhukov, J. Liu, and G. Finkelstein, SU(2) and SU(4) Kondo effects in carbon nanotube quantum dots, *Phys. Rev. B* **75**, 241407 (2007).
- [28] T. Hata, Non-equilibrium Fluctuations Along Symmetry Crossover in a Kondo-Correlated Quantum Dot, in *Non-equilibrium Many-body States in Carbon Nanotube Quantum Dots* (Springer Singapore, Singapore, 2019) pp. 47–59.
- [29] A. C. Hewson, *The Kondo problem to heavy fermions* (Cambridge University Press, Cambridge, 1997).
- [30] B. Dutta, D. Majidi, A. García Corral, P. A. Erdman, S. Florens, T. A. Costi, H. Courtois, and C. B. Winkelmann, Direct Probe of the Seebeck Coefficient in a Kondo-Correlated Single-Quantum-Dot Transistor, *Nano Lett.* **19**, 506 (2019).
- [31] R. Scheibner, H. Buhmann, D. Reuter, M. N. Kiselev, and L. W. Molenkamp, Thermopower of a Kondo Spin-Correlated Quantum Dot, *Phys. Rev. Lett.* **95**, 176602 (2005).
- [32] T. A. Costi, A. C. Hewson, and V. Zlatic, Transport coefficients of the Anderson model via the numerical renormalization group, *J. of Phys.: Cond. Mat.* **6**, 2519 (1994).
- [33] Y. Teratani, R. Sakano, and A. Oguri, Fermi liquid theory for nonlinear transport through a multilevel anderson impurity, *Phys. Rev. Lett.* **125**, 216801 (2020).
- [34] P. Trocha and J. Barnaś, Large enhancement of thermoelectric effects in a double quantum dot system due to interference and Coulomb correlation phenomena, *Phys. Rev. B* **85**, 085408 (2012).
- [35] M. Niklas, S. Smirnov, D. Mantelli, M. Margańska, N.-V. Nguyen, W. Wernsdorfer, J.-P. Cleuziou, and M. Grifoni, Blocking transport resonances via Kondo many-body entanglement in quantum dots, *Nat. Commun.* **7**, 12442 (2016).
- [36] F. Kuemmeth, S. Ilani, D. C. Ralph, and P. L. McEuen, Coupling of spin and orbital motion of electrons in carbon nanotubes, *Nature* **452**, 448 (2008).
- [37] T. Ando, Spin-Orbit Interaction in Carbon Nanotubes, *J. of the Phys. Soc. of Japan* **69**, 1757 (2000).
- [38] D. Huertas-Hernando, F. Guinea, and A. Brataas, Spin-orbit coupling in curved graphene, fullerenes, nanotubes, and nanotube caps, *Phys. Rev. B* **74** (2006).
- [39] J.-S. Jeong and H.-W. Lee, Curvature-enhanced spin-orbit coupling in a carbon nanotube, *Phys. Rev. B* **80**, 075409 (2009).
- [40] D. Krychowski and S. Lipiński, Intra- and inter-shell Kondo effects in carbon nanotube quantum dots, *J. Eur. Phys. B* **91**, 8 (2018).
- [41] D. R. Schmid, S. Smirnov, M. Margańska, A. Dirnacher, P. L. Stiller, M. Grifoni, A. K. Hüttel, , and C. Strunk, Broken SU(4) symmetry in a Kondo-correlated carbon nanotube, *Phys. Rev. B* **91**, 155435 (2015).
- [42] M. R. Galpin, F. W. Jayatilaka, D. E. Logan, and F. B. Anders, Interplay between Kondo physics and spin-orbit coupling in carbon nanotube quantum dots, *Phys. Rev. B* **81**, 075437 (2010).
- [43] D. Mantelli, C. Paşcu Moca, G. Zaránd, and M. Grifoni, Kondo effect in a carbon nanotube with spin-orbit interaction and valley mixing: A DM-NRG study, *Physica E: Low-dim. Sys. and Nano.* **77**, 180 (2016).
- [44] G. A. Steele, F. Pei, E. A. Laird, J. M. Jol, H. B. Meerwaldt, and L. P. Kouwenhoven, Large spin-orbit coupling in carbon nanotubes, *Nat. Commun.* **4**, 1573 (2013).
- [45] P. Florków, D. Krychowski, and S. Lipiński, Kondo effects in small-bandgap carbon nanotube quantum dots, *Beilstein Journal of Nanotechnology* **11**, 1873 (2020).
- [46] R. López, T. c. v. Rejec, J. Martinek, and R. Žitko, SU(3) Kondo effect in spinless triple quantum dots, *Phys. Rev. B* **87**, 035135 (2013).
- [47] M. Ferrier, T. Arakawa, T. Hata, R. Fujiwara, R. Delagrangé, R. Weil, R. Deblock, R. Sakano, A. Oguri, and K. Kobayashi, Universality of non-equilibrium fluctuations in strongly correlated quantum liquids, *Nat. Phys.* **12**, 230 (2016).
- [48] Y. Teratani, R. Sakano, R. Fujiwara, T. Hata, T. Arakawa, M. Ferrier, K. Kobayashi, and A. Oguri, Field-Enhanced Kondo Correlations in a Half-Filling Nanotube Dot: Evolution of an SU(N) Fermi-Liquid Fixed Point, *J. of the Phys. Soc. of Japan* **85**, 094718 (2016).
- [49] M. Ferrier, R. Delagrangé, J. Basset, H. Bouchiat, T. Arakawa, T. Hata, R. Fujiwara, Y. Teratani, R. Sakano, A. Oguri, K. Kobayashi, and R. Deblock, Quantum Noise in Carbon Nanotubes as a Probe of Correlations in the Kondo Regime, *J. of Low Temp. Phys.* **201**, 738 (2020).
- [50] T. Delattre, C. Feuillet-Palma, L. G. Herrmann, P. Morfin, J.-M. Berroir, G. Fève, B. Plaçais, D. C. Glatli, M.-S. Choi, C. Mora, and T. Kontos, Noisy Kondo impurities, *Nat. Phys.* **5**, 208 (2009).
- [51] C. Mora, P. Vitushinsky, X. Leyronas, A. A. Clerk, and K. Le Hur, Theory of nonequilibrium transport in the SU(N) Kondo regime, *Phys. Rev. B* **80**, 155322 (2009).
- [52] C. Mora, Fermi-liquid theory for SU(N) Kondo model, *Phys. Rev. B* **80**, 125304 (2009).
- [53] A. Oguri and A. C. Hewson, Higher-Order Fermi-Liquid Corrections for an Anderson Impurity Away from Half Filling, *Phys. Rev. Lett.* **120**, 126802 (2018).
- [54] Y. Teratani, R. Sakano, T. Hata, T. Arakawa, M. Ferrier, K. Kobayashi, and A. Oguri, Field-induced SU(4) to SU(2) Kondo crossover in a half-filling nanotube dot: Spectral and finite-temperature properties, *Phys. Rev.*

- B **102**, 165106 (2020).
- [55] C. Mora, X. Leyronas, and N. Regnault, Current Noise through a Kondo Quantum Dot in a $SU(N)$ Fermi Liquid State, *Phys. Rev. Lett.* **100**, 036604 (2008).
- [56] A. Oguri, Y. Teratani, K. Tsutsumi, and R. Sakano, Current noise and Keldysh vertex function of an Anderson impurity in the Fermi-liquid regime, *Phys. Rev. B* **105**, 115409 (2022).
- [57] C. Mora, C. P. Moca, J. von Delft, and G. Zaránd, Fermi-liquid theory for the single-impurity Anderson model, *Phys. Rev. B* **92**, 075120 (2015).
- [58] Y. Nishikawa, A. C. Hewson, D. J. G. Crow, and J. Bauer, Analysis of low-energy response and possible emergent $SU(4)$ Kondo state in a double quantum dot, *Phys. Rev. B* **88**, 245130 (2013).
- [59] E. Sela, Y. Oreg, F. von Oppen, and J. Koch, Fractional Shot Noise in the Kondo Regime, *Phys. Rev. Lett.* **97**, 086601 (2006).
- [60] T. Hata, Y. Teratani, T. Arakawa, S. Lee, M. Ferrier, R. Deblock, R. Sakano, A. Oguri, and K. Kobayashi, Three-body correlations in nonlinear response of correlated quantum liquid, *Nat. Commun.* **12**, 3233 (2021).
- [61] E. Majorana, Teoria simmetrica dell'elettrone e del positrone, *Il Nuovo Cimento* (1924-1942) **14**, 171 (1937).
- [62] M. Leijnse and K. Flensberg, Introduction to topological superconductivity and Majorana fermions, *Semicond. Sci. and Tech.* **27**, 124003 (2012).
- [63] K. Flensberg, Non-Abelian Operations on Majorana Fermions via Single-Charge Control, *Phys. Rev. Lett.* **106**, 090503 (2011).
- [64] M. Ezawa, Non-Abelian braiding of Majorana-like edge states and topological quantum computations in electric circuits, *Phys. Rev. B* **102**, 075424 (2020).
- [65] C. W. J. Beenakker, Search for Majorana Fermions in Superconductors, *Ann. Rev. of Cond. Matt. Phys.* **4**, 113 (2013).
- [66] A. Kitaev, Fault-tolerant quantum computation by anyons, *Ann. of Phys.* **303**, 2 (2003).
- [67] C. W. J. Beenakker, Search for non-Abelian Majorana braiding statistics in superconductors, *SciPost Phys. Lect. Notes* , 15 (2020).
- [68] C. Nayak, S. H. Simon, A. Stern, M. Freedman, and S. Das Sarma, Non-Abelian anyons and topological quantum computation, *Rev. Mod. Phys.* **80**, 1083 (2008).
- [69] A. Y. Kitaev, Unpaired Majorana fermions in quantum wires, *Physics-Uspekhi* **44**, 131 (2001).
- [70] H.-L. Lai and W.-M. Zhang, Decoherence dynamics of Majorana qubits under braiding operations, *Phys. Rev. B* **101**, 195428 (2020).
- [71] R. Žitko, Detection of Majorana edge states in topological superconductors through non-Fermi-liquid effects induced in an interacting quantum dot, *Phys. Rev. B* **83**, 195137 (2011).
- [72] G. Castagnoli and M. Rasetti, The notions of symmetry and computational feedback in the paradigm of steady, simultaneous quantum computation, *Int. J. of Theo. Phys.* **32**, 2335 (1993).
- [73] D. P. Arovas, R. Schrieffer, F. Wilczek, and A. Zee, Statistical mechanics of anyons, *Nuc. Phys. B* **251**, 117 (1985).
- [74] F. Wilczek, Quantum Mechanics of Fractional-Spin Particles, *Phys. Rev. Lett.* **49**, 957 (1982).
- [75] D. A. Ivanov, Non-Abelian Statistics of Half-Quantum Vortices in p -Wave Superconductors, *Phys. Rev. Lett.* **86**, 268 (2001).
- [76] M. Greiter, F. D. M. Haldane, and R. Thomale, Non-Abelian statistics in one dimension: Topological momentum spacings and $SU(2)$ level- k fusion rules, *Phys. Rev. B* **100**, 115107 (2019).
- [77] M. Greiter and F. Wilczek, Fractional Statistics, *Ann. Rev. of Cond. Matt. Phys.* **15**, 131 (2024).
- [78] F. D. M. Haldane, Fractional statistics in arbitrary dimensions: A generalization of the Pauli principle, *Phys. Rev. Lett.* **67**, 937 (1991).
- [79] D. Sticlet, C. Bena, and P. Simon, Spin and Majorana Polarization in Topological Superconducting Wires, *Phys. Rev. Lett.* **108**, 096802 (2012).
- [80] J. J. He, T. K. Ng, P. A. Lee, and K. T. Law, Selective Equal-Spin Andreev Reflections Induced by Majorana Fermions, *Phys. Rev. Lett.* **112**, 037001 (2014).
- [81] M. M. Maška and T. Domański, Polarization of the Majorana quasiparticles in the Rashba chain, *Sci. Rep.* **7**, 16193 (2017).
- [82] N. Sedlmayr, M. Guigou, P. Simon, and C. Bena, Majoranas with and without a 'character': hybridization, braiding and chiral Majorana number, *J. of Phys.: Cond. Matt.* **27**, 455601 (2015).
- [83] V. Mourik, K. Zuo, S. M. Frolov, S. R. Plissard, E. P. A. M. Bakkers, and L. P. Kouwenhoven, Signatures of Majorana Fermions in Hybrid Superconductor-Semiconductor Nanowire Devices, *Science* **336**, 1003 (2012).
- [84] E. J. H. Lee, X. Jiang, M. Houzet, R. Aguado, C. M. Lieber, and S. De Franceschi, Spin-resolved Andreev levels and parity crossings in hybrid superconductor-semiconductor nanostructures, *Nat. Nano.* **9**, 79 (2014).
- [85] P. Yu, J. Chen, M. Gomanko, G. Badawy, E. P. A. M. Bakkers, K. Zuo, V. Mourik, and S. M. Frolov, Non-Majorana states yield nearly quantized conductance in proximatized nanowires, *Nature Physics* **17**, 482 (2021).
- [86] M. Cheng, M. Becker, B. Bauer, and R. M. Lutchyn, Interplay between Kondo and Majorana Interactions in Quantum Dots, *Phys. Rev. X* **4**, 031051 (2014).
- [87] Y. Kim, D. E. Liu, E. Gaidamauskas, J. Paaske, K. Flensberg, and R. M. Lutchyn, Signatures of Majorana Kramers pairs in superconductor-Luttinger liquid and superconductor-quantum dot-normal lead junctions, *Phys. Rev. B* **94**, 075439 (2016).
- [88] L. Fu and C. L. Kane, Superconducting Proximity Effect and Majorana Fermions at the Surface of a Topological Insulator, *Phys. Rev. Lett.* **100**, 096407 (2008).
- [89] G. Moore and N. Read, Nonabelions in the Fractional Quantum Hall effect, *Nuc. Phys. B* **360**, 362 (1991).
- [90] N. Read and D. Green, Paired states of fermions in two dimensions with breaking of parity and time-reversal symmetries and the fractional quantum Hall effect, *Phys. Rev. B* **61**, 10267 (2000).
- [91] Z.-Z. Li, F.-C. Zhang, and Q.-H. Wang, Majorana modes in a topological insulator/s-wave superconductor heterostructure, *Sci. Rep.* **4**, 6363 (2014).
- [92] J. D. Sau, R. M. Lutchyn, S. Tewari, and S. Das Sarma, Generic New Platform for Topological Quantum Computation Using Semiconductor Heterostructures, *Phys. Rev. Lett.* **104**, 040502 (2010).
- [93] M. Cheng, M. Becker, B. Bauer, and R. M. Lutchyn, Interplay between Kondo and Majorana Interactions in Quantum Dots, *Phys. Rev. X* **4**, 031051 (2014).

- [94] J. Alicea, Majorana fermions in a tunable semiconductor device, *Phys. Rev. B* **81**, 125318 (2010).
- [95] L. Fu and C. L. Kane, Josephson current and noise at a superconductor/quantum-spin-Hall-insulator/superconductor junction, *Phys. Rev. B* **79**, 161408 (2009).
- [96] Y. Oreg, G. Refael, and F. von Oppen, Helical Liquids and Majorana Bound States in Quantum Wires, *Phys. Rev. Lett.* **105**, 177002 (2010).
- [97] B. Jäck, Y. Xie, J. Li, S. Jeon, B. A. Bernevig, and A. Yazdani, Observation of a Majorana zero mode in a topologically protected edge channel, *Science* **364**, 1255 (2019).
- [98] M. T. Deng, C. L. Yu, G. Y. Huang, M. Larsson, P. Caroff, and H. Q. Xu, Anomalous Zero-Bias Conductance Peak in a Nb-InSb Nanowire-Nb Hybrid Device, *Nano Lett.* **12**, 6414 (2012).
- [99] H. Zhang, D. E. Liu, M. Wimmer, and L. P. Kouwenhoven, Next steps of quantum transport in Majorana nanowire devices, *Nat. Commun.* **10**, 5128 (2019).
- [100] H. Zhang, C.-X. Liu, S. Gazibegovic, D. Xu, J. A. Logan, G. Wang, N. van Loo, J. D. S. Bommer, M. W. A. de Moor, D. Car, R. L. M. Op het Veld, P. J. van Veldhoven, S. Koelling, M. A. Verheijen, M. Pendharkar, D. J. Pennachio, B. Shojaei, J. S. Lee, C. J. Palmström, E. P. A. M. Bakkers, S. D. Sarma, and L. P. Kouwenhoven, RETRACTED ARTICLE: Quantized Majorana conductance, *Nature* **556**, 74 (2018).
- [101] S. Das Sarma, In search of Majorana, *Nat. Phys.* **19**, 165 (2023).
- [102] S. Nadj-Perge, I. K. Drozdov, J. Li, H. Chen, S. Jeon, J. Seo, A. H. MacDonald, B. A. Bernevig, and A. Yazdani, Observation of Majorana fermions in ferromagnetic atomic chains on a superconductor, *Science* **346**, 602 (2014).
- [103] F. Zhang, C. L. Kane, and E. J. Mele, Time-Reversal-Invariant Topological Superconductivity and Majorana Kramers Pairs, *Phys. Rev. Lett.* **111**, 056402 (2013).
- [104] E. Gaidamauskas, J. Paaske, and K. Flensberg, Majorana Bound States in Two-Channel Time-Reversal-Symmetric Nanowire Systems, *Phys. Rev. Lett.* **112**, 126402 (2014).
- [105] Y. Yamazaki, S. Kobayashi, and A. Yamakage, Magnetic Response of Majorana Kramers Pairs Protected by Z₂ Invariants, *J. of the Phys. Soc. of Japan* **89**, 043703 (2020).
- [106] B. Béri, Majorana-Klein Hybridization in Topological Superconductor Junctions, *Phys. Rev. Lett.* **110**, 216803 (2013).
- [107] B. Béri and N. R. Cooper, Topological Kondo Effect with Majorana Fermions, *Phys. Rev. Lett.* **109**, 156803 (2012).
- [108] A. Rahmani and M. Franz, Interacting Majorana fermions, *Rep. Prog. Phys.* **82**, 084501 (2019).
- [109] C.-K. Chiu, D. I. Pikulin, and M. Franz, Strongly interacting Majorana fermions, *Phys. Rev. B* **91**, 165402 (2015).
- [110] M. Lee, J. S. Lim, and R. López, Kondo effect in a quantum dot side-coupled to a topological superconductor, *Phys. Rev. B* **87**, 241402 (2013).
- [111] K. Wrześniewski and I. Weymann, Magnetization dynamics in a Majorana-wire-quantum-dot setup, *Phys. Rev. B* **103**, 125413 (2021).
- [112] I. Weymann, K. P. Wójcik, and P. Majek, Majorana-Kondo interplay in T-shaped double quantum dots, *Phys. Rev. B* **101**, 235404 (2020).
- [113] P. Majek and I. Weymann, Majorana mode leaking into a spin-charge entangled double quantum dot, *Phys. Rev. B* **104**, 085416 (2021).
- [114] R. López, M. Lee, L. Serra, and J. S. Lim, Thermoelectrical detection of Majorana states, *Phys. Rev. B* **89**, 205418 (2014).
- [115] M. Leijnse, Thermoelectric signatures of a Majorana bound state coupled to a quantum dot, *New J. of Phys.* **16**, 015029 (2014).
- [116] F. Chi, Z.-G. Fu, J. Liu, K.-M. Li, Z. Wang, and P. Zhang, Thermoelectric Effect in a Correlated Quantum Dot Side-Coupled to Majorana Bound States, *Nano. Res. Lett.* **15**, 79 (2020).
- [117] P. Majek, K. P. Wójcik, and I. Weymann, Spin-resolved thermal signatures of Majorana-Kondo interplay in double quantum dots, *Phys. Rev. B* **105**, 075418 (2022).
- [118] J. Klinovaja, S. Gangadharaiyah, and D. Loss, Electric-field-induced Majorana Fermions in Armchair Carbon Nanotubes, *Phys. Rev. Lett.* **108**, 196804 (2012).
- [119] D. E. Liu, M. Cheng, and R. M. Lutchny, Probing Majorana physics in quantum-dot shot-noise experiments, *Phys. Rev. B* **91**, 081405 (2015).
- [120] S. Smirnov, Non-equilibrium Majorana fluctuations, *New J. of Phys.* **19**, 063020 (2017).
- [121] S. Smirnov, Revealing universal Majorana fractionalization using differential shot noise and conductance in nonequilibrium states controlled by tunneling phases, *Phys. Rev. B* **105**, 205430 (2022).
- [122] A. Golub and B. Horowitz, Shot noise in a Majorana fermion chain, *Phys. Rev. B* **83**, 153415 (2011).
- [123] K. Elk and W. Gasser, *Die Methode der Greenschen Funktionen in der Festkörperphysik* (Akademie-Verlag Berlin, Berlin, 1979).
- [124] K. Elk and W. Gasser, *Nonequilibrium Green's Functions Approach to Inhomogeneous Systems* (Springer Berlin, Heidelberg, 2012).
- [125] E. Prada, R. Aguado, and P. San-Jose, Measuring Majorana nonlocality and spin structure with a quantum dot, *Phys. Rev. B* **96**, 085418 (2017).
- [126] H.-J. Kwon, K. Sengupta, and V. M. Yakovenko, Fractional ac Josephson effect in p- and d-wave superconductors, *The Eur. Phys. J. B - Cond. Matt. and Compl. Sys.* **37**, 349 (2004).
- [127] L. P. Rokhinson, X. Liu, and J. K. Furdyna, The fractional a.c. Josephson effect in a semiconductor-superconductor nanowire as a signature of Majorana particles, *Nat. Phys.* **8**, 795 (2012).
- [128] D. Krychowski, S. Lipiński, and G. Cuniberti, Spin Dependent Conductance of a Quantum Dot Side attached to Topological Superconductors as a Probe of Majorana Fermion States, *Acta Phys. Pol. A* **133**, 552–554 (2018).
- [129] P. A. Igoshev, M. A. Timirgazin, V. F. Gilmudtinov, A. K. Arzhnikov, and V. Y. Irkhin, Spiral magnetism in the single-band Hubbard model: the Hartree-Fock and slave-boson approaches, *J. of Phys.: Cond. Matt.* **27**, 446002 (2015).
- [130] P. Coleman, Mixed valence as an almost broken symmetry, *Phys. Rev. B* **35**, 5072 (1987).
- [131] M. Lavagna, Functional-integral approach to strongly correlated Fermi systems: Quantum fluctuations beyond the Gutzwiller approximation, *Phys. Rev. B* **41**, 142 (1990).

- [132] W. Zimmermann, R. Frésard, and P. Wölfle, Spin and charge structure factor of the two-dimensional Hubbard model, *Phys. Rev. B* **56**, 10097 (1997).
- [133] K. Yamada, Perturbation Expansion for the Anderson Hamiltonian. II, *Prog. of Theo. Phys.* **53**, 970 (1975).
- [134] H. C. Lee and H.-Y. Choi, Slave-boson approach to the infinite- U Anderson-Holstein impurity model, *Phys. Rev. B* **70**, 085114 (2004).
- [135] L. Mihály and A. Zawadowski, Fermi liquid theory of the degenerate anderson model, *J. de Phys. Lett.* **39**, 483 (1978).
- [136] Y. Y. Lee and C. T. Chen-Tsai, The Fifteenfold way of the SU(4) symmetry scheme of strongly interacting particles, *Chin. J. Phys.* **3**, 45 (1965).
- [137] F. Iachello, *Lie Algebras and Applications* (Springer Berlin, Heidelberg, 2007).
- [138] C. Piquard, P. Glidic, C. Han, A. Aassime, A. Cavanna, U. Gennser, Y. Meir, E. Sela, A. Anthore, and F. Pierre, Observing the universal screening of a Kondo impurity, *Nat. Commun.* **14**, 7263 (2023).
- [139] L. Kadanoff and G. Baym, *Quantum Statistical Mechanics: Green's Function Methods in Equilibrium and Nonequilibrium Problems*, *Frontiers in Physics. A Lecture Note and Reprint Series* (W. A. Benjabin, Inc., New York, 1962).
- [140] H. C. Lee and H.-Y. Choi, Slave-boson approach to the infinite- U Anderson-Holstein impurity model, *Phys. Rev. B* **70**, 085114 (2004).
- [141] I. Weymann and K. P. Wójcik, Transport properties of a hybrid majorana wire-quantum dot system with ferromagnetic contacts, *Phys. Rev. B* **95**, 155427 (2017).
- [142] J. R. Hauptmann, J. Paaske, and P. E. Lindelof, Electric-field-controlled spin reversal in a quantum dot with ferromagnetic contacts, *Nat. Phys.* **4**, 373 (2008).
- [143] D. Krychowski, M. Antkiewicz, and S. Lipiński, Transport through strongly correlated triple quantum dot, *J. of Mag. and Magn. Mat.* **541**, 168564 (2022).
- [144] K. Rao, G. Berghe, and C. Krattenthaler, An entry of Ramanujan on hypergeometric series in his Notebooks, *Journal of Computational and Applied Mathematics* **173**, 239 (2005).
- [145] D. Krychowski, S. Lipiński, and G. Cuniberti, Spin dependent conductance of a quantum dot side attached to topological superconductors as a probe of Majorana fermion states, *Acta Phys. Polon. A* **133**, 552 (2018).
- [146] S. Smirnov, Majorana tunneling entropy, *Phys. Rev. B* **92**, 195312 (2015).
- [147] R. López, R. Aguado, and G. Platero, Shot noise in strongly correlated double quantum dots, *Phys. Rev. B* **69**, 235305 (2004).
- [148] Y. V. Nazarov and Y. M. Blanter, *Quantum Transport: Introduction to Nanoscience* (Cambridge University Press, 2009).
- [149] Y. Yamauchi, K. Sekiguchi, K. Chida, T. Arakawa, S. Nakamura, K. Kobayashi, T. Ono, T. Fujii, and R. Sakano, Evolution of the Kondo Effect in a Quantum Dot Probed by Shot Noise, *Phys. Rev. Lett.* **106**, 176601 (2011).